

## EXTRAGALACTIC SCIENCE AND COSMOLOGY WITH THE SUBARU PRIME FOCUS SPECTROGRAPH (PFS)

RICHARD ELLIS<sup>1</sup>, MASAHIRO TAKADA<sup>2</sup>, HIROAKI AIHARA<sup>2,3</sup>, NOBUO ARIMOTO<sup>4</sup>, KEVIN BUNDY<sup>2</sup>, MASASHI CHIBA<sup>5</sup>, JUDITH COHEN<sup>1</sup>, OLIVIER DORE<sup>6,1</sup>, JENNY E. GREENE<sup>7</sup>, JAMES GUNN<sup>7</sup>, TIMOTHY HECKMAN<sup>8</sup>, CHRIS HIRATA<sup>1</sup>, PAUL HO<sup>9</sup>, JEAN-PAUL KNEIB<sup>10</sup>, OLIVIER LE FEVRE<sup>10</sup>, HITOSHI MURAYAMA<sup>2,11</sup>, TOHRU NAGAO<sup>12</sup>, MASAMI OUCHI<sup>13</sup>, MICHAEL SEIFFERT<sup>4,1</sup>, JOHN SILVERMAN<sup>2</sup>, LAERTE SODRÉ JR<sup>14</sup>, DAVID N. SPERGEL<sup>7</sup>, MICHAEL A. STRAUSS<sup>7</sup>, HAJIME SUGAI<sup>2</sup>, YASUSHI SUTO<sup>3</sup>, HIDEKI TAKAMI<sup>4</sup>, ROSEMARY WYSE<sup>8</sup>, & THE PFS TEAM

*Draft version March 21, 2019*

### ABSTRACT

The Subaru Prime Focus Spectrograph (PFS) is a massively-multiplexed fiber-fed optical and near-infrared spectrograph ( $N_{\text{fiber}}=2400$ ,  $380 \leq \lambda \leq 1300\text{nm}$ ), offering unique opportunities in survey astronomy. Following a successful external design review the instrument is now under construction with first light predicted in late 2017. Here we summarize the science case for this unique instrument in terms of provisional plans for a Subaru Strategic Program of  $\simeq 300$  nights. We describe plans to constrain the nature of dark energy via a survey of emission line galaxies spanning a comoving volume of  $9.3h^{-3}\text{Gpc}^3$  in the redshift range  $0.8 < z < 2.4$ . In each of 6 independent redshift bins, the cosmological distances will be measured to 3% precision via the baryonic acoustic oscillation scale and redshift-space distortion measures will be used to constrain structure growth to 6% precision. As the near-field *cosmology* program, radial velocities and chemical abundances of stars in the Milky Way and M31 will be used to infer the past assembly histories of both spiral galaxies as well as the structure of their dark matter halos. Complementing the goals of the Gaia mission ( $V < 17$ ), radial velocities and metallicities will be secured for  $10^6$  Galactic stars to  $17 < V < 20$ . Data for fainter stars to  $V \simeq 21$  will be secured in areas containing Galactic tidal streams. The M31 campaign will target red giant branch stars with  $21 < V < 22.5$  over an unprecedented area of  $65 \text{ deg}^2$ . For the extragalactic program, our simulations suggest the wide wavelength range of PFS will be particularly powerful in probing the galaxy population and its clustering over a wide redshift range and we propose to conduct a color-selected survey of  $1 < z < 2$  galaxies and AGN over  $16 \text{ deg}^2$  to  $J \simeq 23.4$ , yielding a fair sample of galaxies with stellar masses above  $\sim 10^{10} M_{\odot}$  at  $z \simeq 2$ . A two-tiered survey of higher redshift Lyman break galaxies and Lyman alpha emitters will quantify the properties of early systems close to the reionization epoch. PFS will also provide unique spectroscopic opportunities beyond these currently-envisaged surveys, particularly in the era of Euclid, LSST and TMT.

*Subject headings:* PFS — cosmology — galactic archaeology — galaxy evolution

### 1. INTRODUCTION

There is currently a major expansion in survey imaging capability via the use of CCD and near-infrared detector mo-

saics on a wide range of ground-based telescopes. Such imaging surveys provide accurate photometric and other data to enable the study of gravitational lensing signals which trace the distribution of dark matter and to conduct census studies of Galactic structures and distant star-forming galaxies. For over a decade it has been recognized that a similar revolution would be provided by a massively-multiplexed spectrograph on a large aperture telescope. Spectra provide precise radial velocities, metallicities and emission line properties for faint and distant sources and enable additional probes of cosmology. The main challenge in realizing this second revolution has been access to a wide field telescope, essential for efficient multi-object spectroscopy of panoramic fields, and the cost of implementing the appropriate instrumentation.

The proposal to construct a Subaru Prime Focus Spectrograph (PFS) emerged following the cancellation in May 2009 of the Gemini-sponsored Wide-Field Multi-Object Spectrometer (WFMOS). WFMOS was envisaged as a facility instrument on the Subaru telescope sharing the optics designed for the new prime focus camera, Hyper Suprime-Cam (HSC). Two teams received Gemini funding for a conceptual design study of WFMOS and, prior to cancellation, a team led by Caltech and the Jet Propulsion Laboratory (JPL) secured preliminary approval. Soon after, however, the Gemini Board indicated they did not have sufficient funding to proceed and the WFMOS project was terminated.

The Kavli Institute for the Physics and Mathematics of the

<sup>1</sup> California Institute of Technology, Pasadena, CA 91125, U.S.A

<sup>2</sup> Kavli Institute for the Physics and Mathematics of the Universe (Kavli IPMU), WPI, University of Tokyo, Chiba 277-8583, Japan

<sup>3</sup> Department of Physics, University of Tokyo, Tokyo, 113-0033, Japan

<sup>4</sup> National Astronomical Observatory of Japan, Tokyo, 181-8588, Japan

<sup>5</sup> Astronomical Institute, Tohoku University, Sendai, 980-8578, Japan

<sup>6</sup> Jet Propulsion Laboratory, California Institute of Technology, Pasadena, CA, U.S.A.

<sup>7</sup> Department of Astrophysical Sciences, Princeton University, Princeton, NJ 08544, U.S.A

<sup>8</sup> Department of Physics & Astronomy, Johns Hopkins University, Baltimore, MD 21218, U.S.A.

<sup>9</sup> Institute of Astronomy and Astrophysics, Academia Sinica, Taipei 10617, Taiwan

<sup>10</sup> Laboratoire d'Astrophysique de Marseille, F-13388 Marseille Cedex 13, France

<sup>11</sup> Physics Department, University of California, Berkeley and Lawrence Berkeley National Laboratory, Berkeley, California 94720, U.S.A

<sup>12</sup> The Hakubi Center for Advanced Research, Kyoto University, Kyoto 606-8302, Japan

<sup>13</sup> The Hakubi Center for Advanced Research, Kyoto University, Kyoto 606-8302, Japan

<sup>14</sup> Institute for Cosmic Ray Research, The University of Tokyo, Chiba 277-8582, Japan

<sup>15</sup> Departamento de Astronomia, Geofísica e Ciências Atmosféricas São Paulo, 05508-090, Brazil

Universe (Kavli IPMU) at the University of Tokyo submitted a proposal for stimulus funding to the Japanese government in September 2009 using design concepts pioneered in the WFMOS study led by Caltech and JPL. The successful outcome of this proposal in early 2010 initiated the present PFS partnership which now includes Caltech/JPL, Princeton and Johns Hopkins Universities, the Laboratoire d’Astrophysique de Marseille, Academia Sinica Institute of Astronomy & Astrophysics (ASIAA) Taiwan, the University of São Paulo and the Laboratório Nacional de Astrofísica in Brazil. Our collaboration structure is summarized in Appendix A.

In addition to the leadership funding provided by Kavli IPMU, three important milestones have enabled progress and led to the decision to commence construction. Firstly, in January 2011 the Subaru Users Meeting endorsed the PFS project as a next-generation instrument for the Subaru Prime Focus, recognizing the international PFS team and its responsibilities. This decision led to the establishment of a PFS project office at Kavli IPMU in early 2011 and an allocation of funds and manpower by the National Astronomical Observatory of Japan (NAOJ) towards integration, commissioning and survey operations. A second milestone followed the MOU in December 2011 between the Director-General of NAOJ and the Director of Kavli IPMU, that anticipates a Subaru Strategic Program for PFS providing up to 300 nights of observing time for the PFS team in collaboration with the Japanese astronomical community. These developments provided the essential impetus for the science plans and technical requirements defined in this article. The third milestone was a successful Conceptual Design Review (CoDR) held in March 2012 which triggered the decision to commence construction with first light predicted in 2017. The CoDR documentation included a detailed science case for PFS and a list of technical requirements and this article reproduces these for general interest.

This article is not intended to provide a technical description of PFS but a brief overview is helpful (see Fig. 1). Further technical details of the instrument and its current design can be found in <http://sumire.ipmu.jp/en/2652>. PFS is designed to allow simultaneous low and intermediate-resolution spectroscopy of 2400 astronomical targets over a 1.3 degree hexagonal field. It shares the *Wide Field Corrector* and associated *Field Rotator* and *Hexapod* already constructed for the HSC. An array of 2400 optical fibers is in the *Prime Focus Instrument* and each fiber tip position is controlled in-plane by a two-stage piezo-electric *Fiber Positioner* Cobra system. Each fiber can be positioned within a particular patrol region such that these patrol regions fully sample the 1.3 deg field. A *Fiber Connector* relays light to four identical fixed-format 3-arm twin-dichroic all-Schmidt *Spectrographs* providing continuous wavelength coverage from 380nm to 1.3 $\mu$ m. The blue and red channels will use two Hamamatsu 2K $\times$ 4K edge-buttable fully-depleted CCDs (as in HSC). The near-infrared channel will use a new Teledyne 4RG 4K $\times$ 4K HgCdTe 1.7 $\mu$ m cut-off array.

The present article describes the detailed scientific case for PFS in the context of a Subaru Strategic Program (SSP) of  $\simeq$ 300 nights of observing time. Since such a program would not be implemented until 2017 at the earliest, the main motivation in formulating the team’s plans at this stage is in providing a list of key science requirements for the technical design. In Sections 2 – 4 we describe 3 key components of the science case for PFS that will likely form the basis of the Subaru Strategic Program. For each of these 3 cases we provide a summary, a detailed science justification and survey strat-

egy as well as the flow-down from these to the technical requirements for the instrument. We summarize these science requirements for PFS in more detail in Section 5 and discuss some outstanding issues in Section 6 which we will address prior to our Preliminary Design Review.

## 2. COSMOLOGY

*Summary: PFS will be remarkably powerful in spectroscopic surveys of faint galaxies because of its large multiplex gain and the 8.2 meter aperture of the Subaru telescope. The extended wavelength coverage provided by the red and near-infrared spectrograph arms (650 – 1300nm) will permit a unique survey of [O II] emission-line galaxies extending over the redshift range  $0.8 \leq z \leq 2.4$ . As large-scale structures remain in the linear regime at high redshift, such a survey will give detailed new information on the cosmological parameters as well as the growth rate of structure formation. This combination will provide a valuable test of alternative models of gravity on large scale which may provide a possible explanation for dark energy. Multi-color data planned to arrive from the HSC imager will be used to select target galaxies for spectroscopy and the expected high throughput should yield a  $\simeq$ 75% success rate of detecting [O II] emission at  $S/N > 8.5$ . Herein, we propose to conduct a 100 night cosmological survey over 1400 deg<sup>2</sup>, sampling galaxies within a comoving volume of 9 (Gpc/h)<sup>3</sup> over  $0.8 \leq z \leq 2.4$ . This will complement the lower redshift survey being undertaken by the SDSS BOSS collaboration.*

*The primary goals of the PFS cosmology survey are to: (1) measure the Hubble expansion rate and the angular diameter distance to 3% fractional accuracies in each of 6 redshift bins over  $0.8 < z < 2.4$  via the baryonic acoustic oscillation (BAO) method, (2) use the distance measurements for determining the dark energy density parameter  $\Omega_{de}(z)$  to about 7% accuracy in each redshift bin, when combined with lower redshift BAO measurements, (3) use the geometrical constraints to determine the curvature parameter  $\Omega_K$  to 0.3% accuracy, and (4) measure the redshift-space distortion (RSD) in order to reconstruct the growth rate of large-scale structure to 6% accuracy since a redshift  $z = 2.4$ . These PFS measurements of the large scale galaxy distribution can be combined with complementary weak lensing information from the HSC survey in order to significantly improve the cosmological and structure growth constraints and reduce uncertainties arising from galaxy bias and nonlinear effects that are otherwise major sources of systematic error in spectroscopic surveys.*

### 2.1. Cosmology Objectives

The accelerated expansion of the Universe is the most intriguing problem in cosmology. It either requires the introduction of a mysterious form of energy, “dark energy”, or it could signal a breakdown of Einstein theory of General Relativity on cosmological scales. To distinguish between these and other possibilities requires precise observational constraints on both the expansion history of the universe and the growth rate of large-scale structure.

Measurements of galaxy clustering statistics are one of the most powerful means of addressing the nature of dark energy. The tight coupling between baryons and photons prior to the decoupling epoch of  $z \simeq 1100$  leaves a characteristic imprint on the pattern of galaxy clustering on large scales – the so-called baryonic acoustic oscillation (BAO) scale. As the BAO length scale is precisely constrained as  $\simeq 150$  Mpc from cosmic microwave background (CMB) experiments (Komatsu

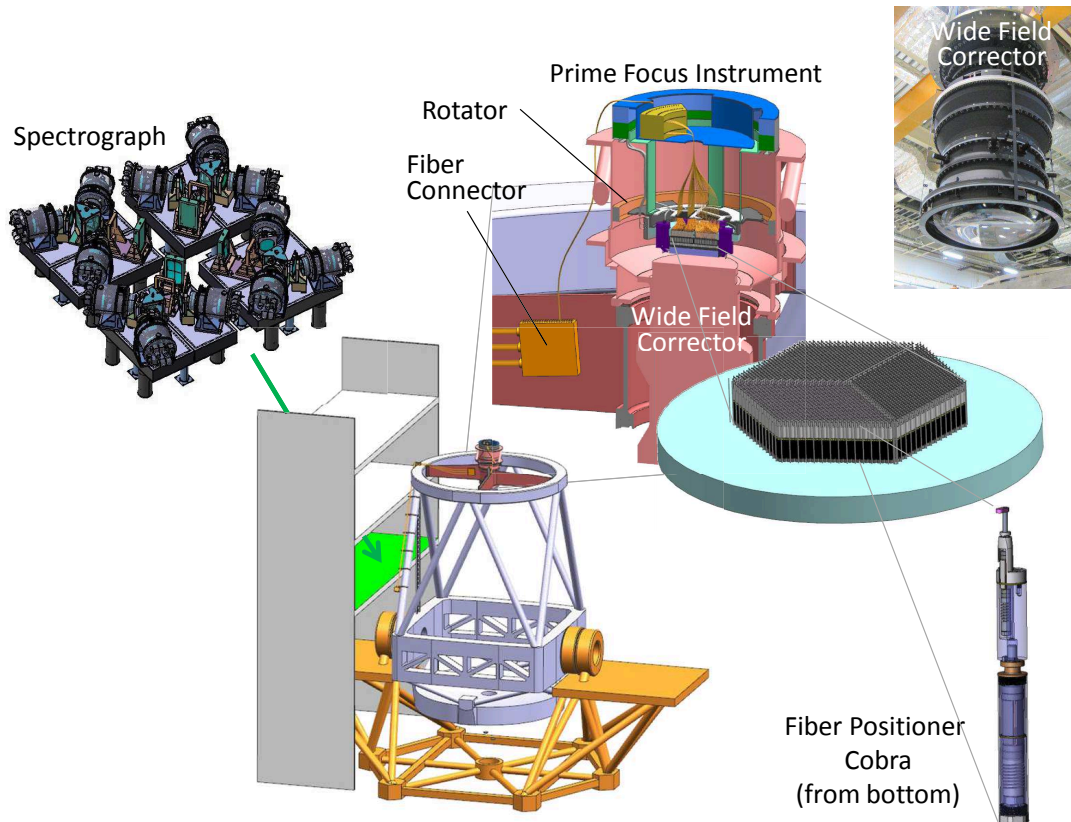


FIG. 1.— A brief overview of PFS instruments, which consist of components **Wide Field Corrector**, **Field Rotator**, **Prime Focus Unit**, and **Fiber Positioner**. A **Fiber Connector** relays light to four identical fixed-format 3-arm twin-dichroic all-Schmidt **Spectrographs** providing continuous wavelength coverage from 380nm to  $1.3\mu\text{m}$ .

et al. 2011), it offers a standard ruler by which we can infer the angular diameter distance and the Hubble expansion rate from the observed correlation function of the galaxy distribution. The BAO scale is in the linear or weakly-nonlinear density regime and thus provides a robust geometrical test. Furthermore, if uncertainties arising from galaxy bias can be removed or accurately modeled, we can use the amplitude and shape information of the galaxy correlation function in order to constrain cosmological parameters as well as the growth rate of structure formation.

Recognizing this, the main scientific questions we seek to address with the PFS cosmology survey are:

1. *Is the cosmic acceleration caused by dark energy or does it represent a failure of Einstein's theory of gravity on cosmological length scales?*
2. *What is the physics of the early universe that generates the primordial fluctuations as the seed of large-scale structures?*

To address these fundamental questions, the main goals for the PFS cosmology survey are to:

- Constrain the angular diameter distance and the Hubble expansion rate via the BAO experiment to the precision comparable with, or better than, existing, ongoing or planned BAO surveys.
- Derive the BAO constraints in a redshift range that is complementary to those probed by the existing or

planned BAO surveys on the time scale of the PFS survey.

- Utilize the unique capabilities of the 8.2m Subaru Telescope and the PFS spectrograph for maximizing cosmological science.
- Use the shape and amplitude of galaxy correlation function in order to constrain cosmological parameters as well as the growth rate of structure formation.
- Combine the weak lensing information, delivered from the HSC survey, with the PFS cosmology survey in order to improve the cosmological constraints by calibrating systematic uncertainties that cannot be resolved by either of the PFS and HSC surveys alone.

## 2.2. PFS Cosmology Survey

Here we describe the parameters of the PFS cosmology survey that are required to meet the above scientific goals.

Firstly, we will consider which type of galaxy to target with PFS. Given the optical and near infrared wavelength coverage of PFS, [O II] emission-line galaxies (ELG; [O II]  $\approx 3727\text{\AA}$ ) are particularly useful tracers allowing an efficient survey out to high redshift beyond  $z = 1$ , a redshift range that is difficult to probe with 4m-class telescopes. Luminous red galaxies (LRGs) are a further potentially-useful tracer of large-scale structure as studied by the SDSS survey, but at  $z \gtrsim 1.4$  they reveal weaker spectral features and are less abundant per unit

TABLE 1  
INSTRUMENTATION PARAMETERS

Number of fibers	2400 (600 for each spectrograph)		
Field of view	1.3 deg (hexagonal – diameter of circumscribed circle)		
Field of view area	1.098 deg <sup>2</sup>		
Fiber diameter	1.13'' diameter at the field center; 1.03'' at the edge		
	Blue arm	Red arm	IR arm
Wavelength coverage [nm]	380–670	650–1000	970–1300
Spectral resolution $\lambda/\Delta\lambda$	1900	2400	3500
Pixel scale [ $\text{\AA}/\text{pix}$ ]	0.71	0.85	0.81
Read-out noise [ $e^-$ rms/pix]	3	3	4 <sup>a</sup>
Detector type/read-out mode	CCD	CCD	HgCdTe/SUTR
Thermal background [ $e^-/\text{pix}/\text{sec}$ ]	None	None	0.013
Dark current [ $e^-/\text{pix}/\text{sec}$ ]	$3.89 \times 10^{-4}$	$3.89 \times 10^{-4}$	0.01
Spectrograph image quality [ $\mu\text{m}$ rms/axis]	14	14 <sup>b</sup>	14
Sky continuum	21.56 mag AB/arcsec <sup>2</sup> @ $1 \mu\text{m}$ at zenith <sup>c</sup>		
OH line brightness	16.6 mag AB/arcsec <sup>2</sup> @ $J$ band at zenith <sup>c</sup>		
Moonlight	None (dark time)		
Atmospheric extinction	Variable; continuum is 0.05 mag/airmass @ $\lambda > 0.9 \mu\text{m}$ <sup>c</sup>		
Instrument throughput	Provided from the project office		
Grating wings	Lorentzian with $\frac{1}{3}$ of the true number of lines		
Diffuse stray light	2% of the total light reaching the detector		
Sky subtraction residuals	2% per pixel <sup>d</sup>		

NOTE. — PFS instrumentation parameters and associated assumptions used for estimating an expected signal-to-noise ratio for an observation of emission-line galaxies.

<sup>a</sup> Per sub-exposure; if the NIR channel is not reset between exposures, the actual assumption corresponds to  $4\sqrt{2} = 5.6 e^-$  rms.

<sup>b</sup> Defocus within the thick CCD is considered separately.

<sup>c</sup> Option 0x11003 in the Exposure Time Calculator, v1.

<sup>d</sup> Equivalent to 1% per 4-pixel resolution element.

volume. In the following we focus on ELGs to explore an optimal survey design. We may retain LRGs in future considerations of our survey plans, but their study is not required to meet the PFS cosmology objectives defined above.

### 2.2.1. Sensitivity of the PFS spectrograph

To estimate the feasibility of PFS for a wide-field survey of ELGs, we have studied the expected performance of measuring a [O II] line of a galaxy in our targeted redshift range for a representative exposure time during the dark lunar phase. In doing so, we properly account for the sky emission (continuum plus OH emission lines) and absorption as well as the instrumentation parameters for the current baseline design (as listed in Table 1).

Fig. 2 shows the expected signal-to-noise ratio of the [O II] line as a function of redshift, measured with each of the blue, red and near-infrared (NIR) arms of PFS. As a working example, here we assume  $f_{[\text{OII}]}$  =  $5 \times 10^{-17}$  erg/s/cm<sup>2</sup> for the total flux of the [O II] doublet, 15min for the exposure time, 0.8'' seeing size and  $E(B - V)$  = 0.05 for the Galactic dust extinction, respectively. The galaxy radial profile is assumed to be an exponential disk with a half-light radius of 0.3''. Note that for the galaxy yield forecasts, we use half-light radii from the COSMOS Mock Catalog (Jouvel et al. 2011), and re-compute the fiber aperture correction for each galaxy.<sup>16</sup> We have assumed the 15 minute integration is split into 2 sub-exposures for cosmic ray (CR) detection in the CCD channel. The NIR channel will perform CR rejection by processing of the frames acquired during sample-up-the-ramp (SUTR) mode. The cosmology ETC assumes  $4 e^-$  read noise per sub-exposure (appropriate for  $\sim 90$  samples along a

450sec ramp). We will probably *not* reset the NIR channel in between sub-exposures, so an overall read noise of  $4\sqrt{2} = 5.6 e^-$  per pixel would enable the survey described herein.

In addition to throughput and sky brightness considerations, we have considered several other potential limitations. Their amplitude is difficult to estimate, but they have been important for previous spectrographs and so we make an explicit allowance for them so as to adopt a conservative approach. The systematic sky subtraction residuals and small-angle stray light are very important factors in the study of galaxy spectra where [O II] is partially blended with a sky line. Diffuse stray light is a concern when [O II] lies in a cleaner part of the NIR spectrum.

- *Systematic sky subtraction residuals* – These are modeled by adding a “noise” term corresponding to some percentage of the sky counts in each spectral pixel. We currently set this to 2% of the brightest of the pixel and its neighbor on either side (equivalent to 1% sky subtraction accuracy on a 4-pixel resolution element).
- *Small-angle stray light* – We assign to the grating an effective number of lines that is  $1/3$  of the actual number.
- *Diffuse stray light* – We take 2% of the OH line flux incident on the detector and uniformly spread it over all pixels. (This may be appropriate for a detector that reflects 10% of the incident radiation, and then there are many surfaces that could potentially reflect this radiation back. Refining this parameter will be a priority since the  $S/N$  forecasts degrade rapidly if it gets worse.)

<sup>16</sup> This assumes that the [O II] emission traces the  $I$ -band continuum in which the galaxy sizes were measured.

Continuing our conservative approach, we assumed the instrumentation throughput at the edge of the focal plane and 26

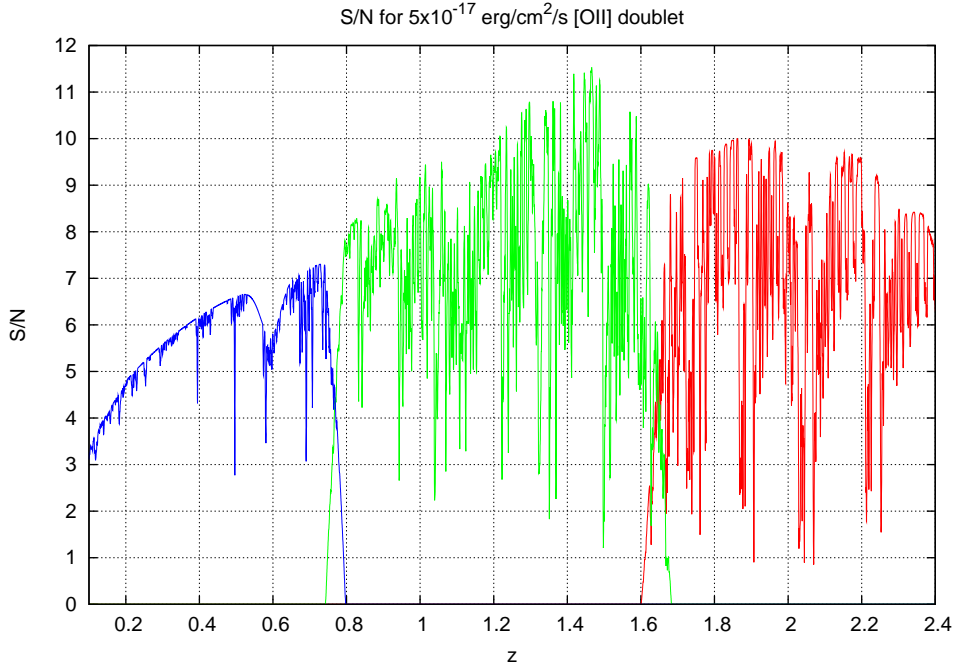


FIG. 2.— Expected signal-to-noise ( $S/N$ ) ratio for measuring the [O II] emission line as a function of redshift; the blue, green and red curves show the results for the PFS blue, red and IR arms in Table 1, respectively, for an total emission line flux of  $5 \times 10^{-17}$  erg/cm<sup>2</sup>/s. To properly account for the uncertainties, we assumed the instrumentation parameters of the current baseline design listed in Table 1, an observation at the edge of the focal plane, and included the sky emission/absorption and the Galactic dust extinction of  $E(B - V) = 0.05$  and 26 degrees for the zenith angle of the telescope. This computation assumes 15 min total exposure (split into two exposures; 450sec  $\times$  2),  $\sigma_v = 70$  km/s for the velocity dispersion (the intrinsic line width), and  $0.8''$  for the seeing FWHM. We also accounted for the finite galaxy size relative to the seeing profile and the fiber size, assuming an exponential profile with scale radius  $0.3''$  for the emission-line region. Note that  $S/N$  is estimated by the root-sum-square of the spectral pixels (i.e. it is a matched filter combining both doublet members). The current design allows a significant detection of [O II] emission line over a wide range of redshift, up to  $z \simeq 2.4$  with near-equal sensitivities of the red and NIR arms.

degrees for the zenith angle. (The latter corresponds to observations at declination  $5^\circ$ S, the southern boundary of the HSC survey region, and  $\pm 0.5$  hours away from transit.)

Fig. 2 shows that the current design of PFS allows a significant detection of the [O II] line over a wide range of redshift, up to  $z \simeq 2.4$ . Most importantly, the baseline design provides near-equal sensitivity of the red and NIR arms for measuring the [O II] line for the same exposure time. Hence PFS can execute a cosmological survey very efficiently over a wide range of redshift, provided sufficiently bright ELGs are available for study (see below).

In the following analysis, we set a threshold of  $S/N = 8.5$  (matched filter) for detection of an ELG. In principle, it may be possible to accept less significant detections. However given the uncertainties in the airglow and the early stage of the instrument design, we consider it prudent to set aside some margin in  $S/N$ .

### 2.2.2. Target selection of emission-line galaxies

We now address how to optimally select ELGs as suitable targets in the proposed redshift range. We will assume that we can use the multi-color imaging data of the planned HSC survey which will be executed ahead of the PFS survey. The currently-planned HSC survey will reach  $i \simeq 26$  ( $5\sigma$  for a point source and  $2''$  aperture), in the 5 passbands *grizy* over  $\sim 1500$  square degrees.

As seen in Fig. 2, if we target ELGs over the wide redshift range  $0.8 \leq z \leq 2.4$ , the wide wavelength coverage of red and NIR arms allows a very efficient selection of [OII] emission-line galaxies. A  $g - r$  color cut is ideal for selecting galaxies in this redshift range: if an object is blue

( $g - r < 0.3$ ), then it likely has no spectral breaks in the  $g$  and  $r$  bands – this means the redshift is high enough for the Balmer/4000Å break to have redshifted beyond the  $r$  band, but the Lyman break has not yet entered the  $g$  band. Furthermore,  $g - r < 0.3$  implies a blue rest-frame UV slope, which has a strong correlation with the star-formation activity that produces the [O II] emission.

To estimate the efficiency of various target selections, we used the COSMOS Mock Catalog (Jouvel et al. 2011), where fluxes of various emission lines of each galaxy are estimated based on physical parameters (SFR, stellar mass and metallicity) using the COSMOS 30 passband photometric data and zCOSMOS spectroscopic data. We have chosen the preliminary target selection cuts:

$$\begin{aligned} 22.8 \leq g \leq 24.2 \text{ AND } -0.1 < g - r < 0.3 \\ \text{AND NOT } (g > 23.6 \text{ AND } r - i > 0.3). \end{aligned} \quad (1)$$

The HSC depth ( $g, r, i \simeq 26$  mag AB at  $5\sigma$ ) is sufficient to find the target galaxies *and* to provide accurate  $g - r$  and  $r - i$  colors. The ELGs in the redshift range  $0.8 \lesssim z \lesssim 2.4$  are primarily selected from the color cut  $-0.1 < g - r < 0.3$ , the  $g$ -magnitude cut gives preference to bright objects while reducing low-redshift contamination as can be seen in Fig. 3. The condition on  $r - i$  for fainter magnitudes is designed to tilt the redshift distribution in favor of more objects at  $z > 1$ . We can further divide the targets into a “bright subsample” ( $g \leq 23.9$ ) and a “faint subsample” ( $g > 23.9$ ), with the brighter targets prioritized when there is an option to increase the success rate.

In the COSMOS Mock Catalog there are 7847 target galax-

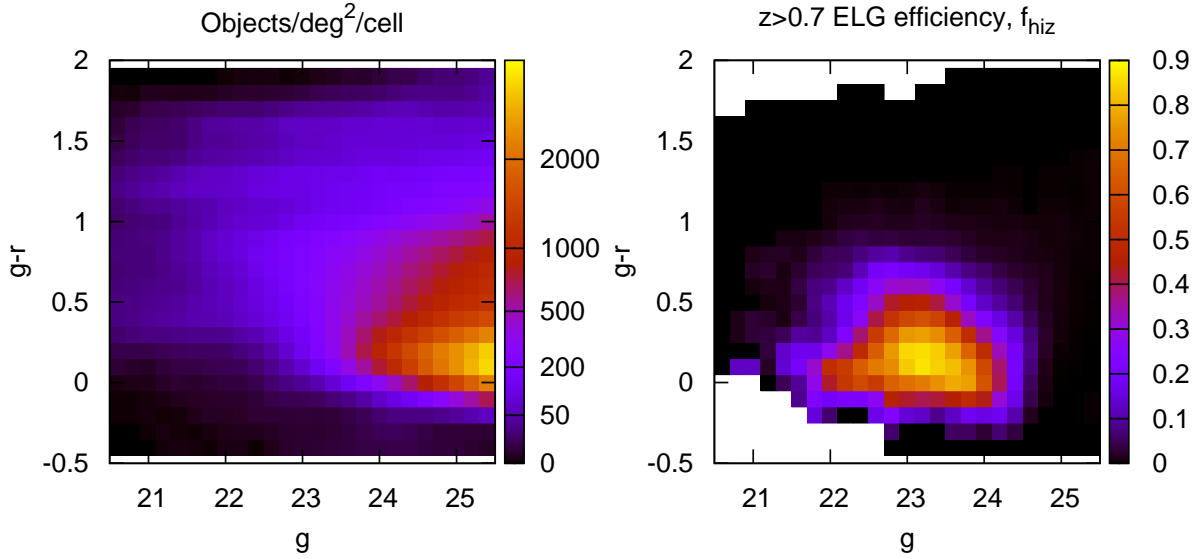


FIG. 3.— *Left panel:* The distribution of objects in the COSMOS Mock Catalog on the color-magnitude diagram. *Right:* The fraction of objects in each cell that are  $z > 0.7$  ELGs with [O II] doublets detectable at  $\geq 8.5\sigma$  in PFS in  $2 \times 7.5$  min exposures. The third dimension ( $r - i$ ) is not shown on this 2D plot, but allows us to select lower or higher redshift galaxies within the PFS survey range.

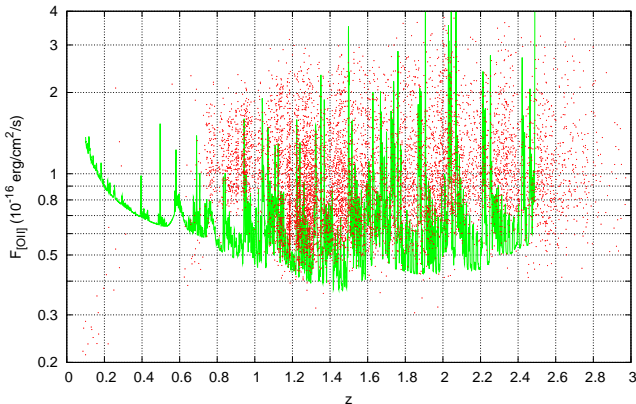


FIG. 4.— The sensitivity of PFS (green curve;  $8.5\sigma$ ,  $2 \times 450$ s exposures, dark time) to the [O II] doublet at  $r_{\text{eff}} = 0.3''$  and 1:1 line ratio, versus the selected targets (red points). Note that the redshift  $z = 2.49$  corresponds to the long wavelength end of the NIR arm. Most targets will yield successful redshifts, but some are lost within the atmospheric emission or absorption lines, a few are at  $z \geq 2.5$ , and there is a small number of faint blue nearby objects (lower-left corner). Note that the line ratio ( $F_{3726} : F_{3729}$ ) and effective radius are re-computed for each galaxy in the COSMOS Mock Catalog, and hence the sensitivity curve drawn does not correspond to an exact boundary between detections and non-detections.

ies available per PFS field-of-view ( $1.098 \text{ deg}^2$  for the  $1.3^\circ$  FoV diameter). Hence there are a sufficient number of target galaxies compared to the number of fibers ( $N=2400$ ) for the baseline design. The blue-solid curve then shows the redshift distribution of [O II] galaxies with  $S/N \geq 8.5$  for a 15 minutes exposure. To estimate the expected  $S/N$  for each galaxy, we employed the same method used in Fig. 2 and also used the galaxy size information and [O II] doublet ratio available from the COSMOS mock catalog.

Assuming 2400 fibers in the focal plane as in Table 1 and using the results in Fig. 5, we can estimate a success rate of finding [O II] emission-line galaxies among the target galaxies. We show the magnitude and [O II] flux distributions of the targets in Fig. 4, and the redshift histogram of the successful [O II] detections in Fig. 5. Of the targets, 74% have successful [O II] detections, 6% are faint blue local ( $z \leq 0.3$ ) objects, 6% fail due to an [O II] feature that falls off the red end of the spectrograph, and the remaining 14% fail due to some combination of too faint [O II] feature or overlap with an atmospheric emission or absorption complex. To have a sufficiently dense sampling of galaxies to trace large-scale structures in each redshift slice, we will need multiple visits of each field; our BAO forecasts found that 2 visits gave the best constraints.

To obtain a reliable estimate of the number of observable targets, we took into account the fiber allocation efficiency assuming a Poisson distribution of target galaxies on the sky, which should be a good approximation for a given wide redshift coverage. We conservatively assume non-overlapping patrol zones between the different fibers.<sup>17</sup> The fiber assignment algorithm is designed to put the easier targets in one of the visits (“Visit A”) and then the harder targets that require better conditions in another (“Visit B”). We divide our targets into two tiers – the bright ( $g \leq 23.9$ ) and faint ( $g > 23.9$ ) subsamples. The fiber assignment logic within each patrol zone is then:

- If at least two bright targets are available, one is assigned to Visit A and another to Visit B.
- If one bright target and at least one faint target are avail-

<sup>17</sup> That is, we allow a galaxy only to be observed by the nearest fiber, even though 21% of galaxies are in overlaps and could potentially be observed by either of two fibers.

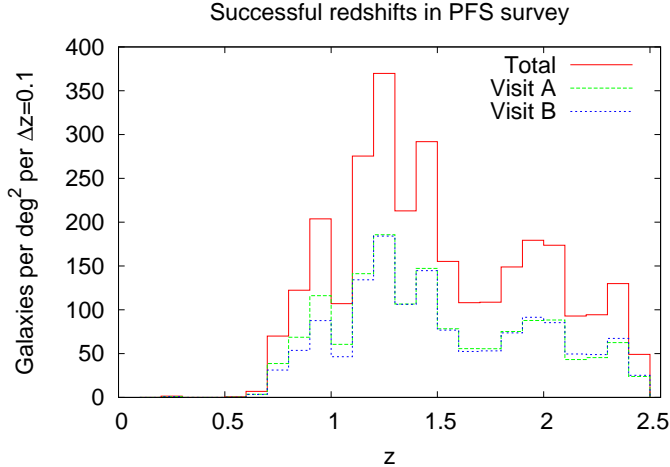


FIG. 5.— The distribution of successful redshifts ([O II] detected at  $S/N > 8.5$ ) for the proposed PFS cosmology survey, including breakdown into the two visits. The jagged features in the curves reflect the effect of sampling variance of large-scale structures in the COSMOS field due to the finite survey area (the mock is based on the data of 1.24 square degrees). We refer to the two visits as “Visit A” and “Visit B” (see text for details), respectively, where we preferentially select brighter targets with  $g < 23.9$  in Visit A in order to have some flexibility between dark/grey nights.

able, then the bright target is observed in Visit A and one of the faint targets is observed in Visit B.

- If one bright target and no faint targets are available, then the bright target is observed in Visit A and the fiber becomes a sky fiber in Visit B.
- If no bright targets are available and there are at least two faint targets, then a faint target is observed in both Visits A and B.
- If no bright targets are available and there is only one faint target, then the fiber becomes a sky fiber in Visit A and the faint target is observed in Visit B.
- If no targets are available, then the fiber is a sky fiber in both Visits A and B.

This algorithm produces a roughly balanced abundance of sky fibers in the two visits. The predicted allocations of the fibers are:

- Visit A: 85% bright targets, 6% faint targets, 9% sky.
- Visit B: 56% bright targets, 33% faint targets, 11% sky.

Thus this leave about 240 sky fibers in each visit for a calibration of the sky spectrum.

Note that the two visits could be scheduled in either order. Since Visit A has the brighter targets, it can achieve a high success fraction under worse conditions than Visit B. We have therefore assumed that Visit B takes place during dark time, whereas Visit A is scheduled on a night of 7 days from the new moon (but at least  $45^\circ$  from the targets). The exposure times in both cases are kept at  $2 \times 450\text{sec}$ . The predicted redshift success rate for a  $S/N > 8.5$  threshold is 75% (Visit A)<sup>18</sup> or 73% (Visit B).

<sup>18</sup> This would rise to 79% if Visit A were during dark time.

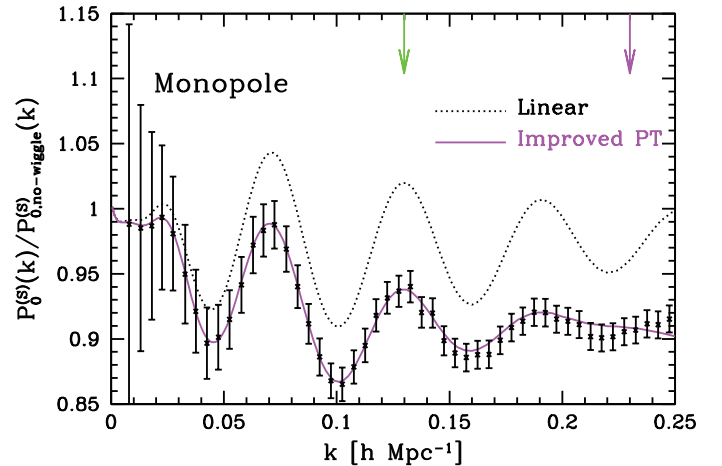


FIG. 6.— An illustration of the BAO features in the power spectrum. The cross symbols with error bars show the N-body simulation results, where the error bars are the expected  $1\sigma$  statistical errors of power spectrum measurement at each  $k$ 's bins for the PFS BAO survey of  $z \sim 1$  slices. The solid curve shows the analytical prediction at  $z = 1$ , computed using the refined perturbation theory of nonlinear structure formation (Taruya et al. 2009). The perturbation theory prediction is in remarkable agreement with the simulation result on scales up to  $k \gtrsim 0.25 h\text{Mpc}^{-1}$ . For comparison, the dotted curve represents the prediction from linear theory.

An alternative to the baseline (using gray time for Visit A) would be to use dark time only for the cosmology survey, and shorten the exposure time for Visit A, thereby reducing the total number of nights required but using time that may be in high demand by other programs. This trade will be made when we design an integrated observing schedule for PFS (see Section 6).

### 2.2.3. Survey Strategy

Using the results of target selection in Fig. 5, we have adopted parameters for the PFS cosmology survey summarized in Table 2. Since our primary observable is the galaxy two-point correlation function or the galaxy power spectrum, the key factors that govern the results are the geometrical volume surveyed and the ratio of clustering power to shot noise,  $\bar{n}_g P_g$ . To have a galaxy power spectrum measurement that reaches the sampling variance limit for our volume and is not degraded by shot noise, the number density of galaxies must satisfy  $\bar{n}_g P_g \gtrsim 1$  at BAO scales (see Fig. 6). As given by the columns of Table 2, the PFS survey we are proposing has  $\bar{n}_g P_g \gtrsim$  a few and slightly less than 1 at  $k = 0.1$  and  $0.2 h/\text{Mpc}$ , respectively, over an entire target redshift range. With only one visit per field, these numbers are about a factor 2 smaller than in Table 2. On the other hand, if we have more than two visits, the survey area we can cover for a given number of nights becomes smaller. Incorporating multiple visits ensures more flexibility in optimizing the survey, for example in including a mixture of targets in different magnitude ranges.

We have assumed that the bias factor for the ELGs is given by  $b_g(z) = 0.9 + 0.4z$ . This specific function was a fit to semi-analytic models (Orsi et al. 2010), but compares very well to real data: e.g. the DEEP2 “main blue” sample has a measured bias of  $b_g = 1.28 \pm 0.04$  at  $z = 0.9$  (Coil et al. 2008).<sup>19</sup> We have much less information about clustering of

<sup>19</sup> This was normalized to a  $\sigma_8 = 0.9$  model; with the lower  $\sigma_8$  now

TABLE 2  
PFS COSMOLOGY SURVEY PARAMETERS

redshift	$V_{\text{survey}}$ [Gpc/h] <sup>3</sup>	$N_g$ per field	$\bar{n}_g$ [10 <sup>-4</sup> (h/Mpc) <sup>3</sup> ]	bias $b_g$	$\bar{n}_g P_g(k)$ $k = 0.1 h/\text{Mpc}$	$\bar{n}_g P_g(k)$ $k = 0.2 h/\text{Mpc}$
0.6 < $z$ < 0.8	0.59	85	1.9	1.18	0.74	0.25
0.8 < $z$ < 1.0	0.79	358	6.0	1.26	2.23	0.74
1.0 < $z$ < 1.2	0.96	420	5.8	1.34	2.10	0.68
1.2 < $z$ < 1.4	1.09	640	7.8	1.42	2.64	0.87
1.4 < $z$ < 1.6	1.19	491	5.5	1.50	1.78	0.59
1.6 < $z$ < 2.0	2.58	598	3.1	1.62	0.95	0.31
2.0 < $z$ < 2.4	2.71	539	2.7	1.78	0.76	0.25

NOTE. — The leftmost column shows the redshift range of each slice, and the other columns show the comoving volume ( $V$ ), the number of [OII] galaxies per field ( $N_g$ ), the mean comoving number density ( $\bar{n}_g$ ), the linear bias parameter ( $b_g$ ) and the values of  $\bar{n}_g P_g(k)$  at  $k = 0.1$  and  $0.2 h/\text{Mpc}$  for each slice, respectively. The survey volume is for a survey area of 1464 square degrees, which is estimated assuming 15 min of open-shutter time per visit, 2 visits per field, 3 min overhead per visit, and 100 clear nights. For comparison, the BOSS BAO survey has the survey parameters: 10000 sq. degrees area coverage over  $0.4 < z < 0.7$ ,  $V_{\text{survey}} = 4.4 (\text{Gpc}/h)^3$ ,  $\bar{n}_g = 3 \times 10^{-4} (h/\text{Mpc})^3$ ,  $b_g = 2.3$  and  $\bar{n}_g P_g(k = 0.1 h/\text{Mpc}) \simeq 5$ .

ELGs at redshifts beyond the DEEP2 survey, but H $\alpha$  emitters at  $z = 2.23$  have a correlation length of  $r_0 = 3.1 \pm 0.7 \text{ Mpc}/h$  (Sobral et al. 2010), implying a bias of  $b_g = 1.87_{-0.26}^{+0.24}$ .

The power spectrum measurement accuracy depends also on the area coverage. In order for the PFS survey to have a constraining power of cosmological parameters comparable with the existing or planned BAO surveys, we need a sufficiently large area coverage. We have found that, if about 100 clear nights are allocated to the PFS cosmology survey, it can meet our scientific goals. Hence we assume 100 clear nights for the following analysis, and the total area covered is estimated as

$$\frac{100 \text{ [nights]} \times 8 \text{ [hours]} \times 60 \text{ [min]}}{2 \text{ [visits]} \times (15 \text{ [min]} + 3 \text{ [min]})} \times 1.098 \text{ [sq. degrees per FoV]} = 1464 \text{ sq. degrees} \quad (2)$$

Here we conservatively assumed 3min overhead for each new pointing, which covers readout, slewing and the time for accurate fiber positioning, and assumed that 8 hours per night are available for observation on source. The comoving volume in each redshift slice is given in Table 2. The total volume is about  $9.3 (\text{Gpc}/h)^3$ , a factor 2 larger volume than the SDSS BOSS galaxy survey, which is about  $4.4 (\text{Gpc}/h)^3$ . A notable strength of the PFS survey is that it probes large-scale structure in higher redshifts, where the fluctuations are largely in the linear regime and therefore allow a cleaner estimation of cosmological parameters. In fact the genuine cosmological power comes from the volume in Fourier space; the effective volume at each wavenumber is given as  $V_{\text{eff}}(k) = [\bar{n}_g P_g(k) / (1 + \bar{n}_g P_g(k))]^2 V_{\text{survey}}$ , where  $V_{\text{survey}}$  is the comoving volume. The total number of the Fourier modes usable of constraining cosmology is estimated by integrating the effective volume in Fourier space up to the maximum wavenumber  $k_{\text{max}}$  which is determined such that the theoretical model to be compared with the measurement is reliable up to the  $k_{\text{max}}$ . The larger the redshift, the higher the wavenumber we can use, because the nonlinear scale becomes smaller (higher  $k$ ). Hence, the proposed PFS survey offers much more than a factor 2 improvement compared to the BOSS constraint (e.g., Anderson et al. 2012). Although Table 2 also gives estimates for the lower redshift slice  $0.6 < z < 0.8$ , which partially overlaps the ongoing

BOSS and WiggleZ surveys, the cosmological constraining power of this slice is not as great due to the smaller areal coverage and reduced galaxy number density. However, we consider it important to retain this redshift slice as it can give a useful benchmark in comparison with other surveys such as the BOSS and WiggleZ surveys, particularly for calibrating systematic issues.

#### 2.2.4. Expected cosmological constraints

We now can estimate the power of the PFS cosmology survey in Table 2 for constraining cosmological parameters. To ensure a fair comparison with other surveys, we primarily assess the power of PFS survey in terms of its BAO geometrical constraints.

##### Geometrical constraints:

The galaxy two-point correlations are measured as a function of the separation lengths between paired galaxies. The position of each galaxy needs to be inferred from the measured redshift and angular position. Then the separation lengths perpendicular and parallel to the line-of-sight direction from the measured quantities are given as  $r_{\perp} \propto \Delta\theta$  and  $r_{\parallel} \propto \Delta z$ , where  $\Delta\theta$  and  $\Delta z$  are the differences between the angular positions and the redshifts of the paired galaxies. For this conversion, we need to assume a reference cosmological model to relate the observables ( $\Delta\theta$ ,  $\Delta z$ ) to the quantities ( $r_{\perp}$ ,  $r_{\parallel}$ ). Thus, the wavenumbers are given as

$$k_{\perp, \text{ref}} = \frac{D_A(z)}{D_{A, \text{ref}}(z)} k_{\perp}, \quad k_{\parallel, \text{ref}} = \frac{H_{\text{ref}}(z)}{H(z)} k_{\parallel}. \quad (3)$$

The quantities with subscript ‘‘ref’’ are the quantities estimated from the observables assuming a ‘‘reference’’ cosmological model, and the quantities without the subscript are the underlying true values. Since the reference cosmological model assumed generally differs from the underlying true cosmology, it causes an apparent distortion in the two-dimensional pattern of galaxy clustering. In principle, the distortion could be measured using only the isotropy of clustering statistics (Alcock & Paczynski 1979), but a more robust measurement can be obtained using features in the power spectrum, particularly if they are at a known scale so that we can measure both  $D_A(z)$  and  $H(z)$ . In particular, the CMB-inferred BAO scale of 150 Mpc gives a powerful standard ruler for this geometrical test (Eisenstein et al. 2005; Perci-

avored, the bias would be higher, i.e. ‘‘better’’ for the BAO analysis.



val et al. 2007; Blake et al. 2011; Hu & Haiman 2003; Seo & Eisenstein 2003).

The use of this scale without edge effects in a survey field requires the survey to be contiguous on a scale large compared to the BAO length; at our minimum redshift ( $z = 0.8$ ), 2.5 BAO lengths corresponds to 7.5 degrees on the sky, so we set this as our minimum width. This requirement will be refined further by simulations.

In more detail, the galaxy power spectrum in redshift space is given in the linear regime as

$$P_{g,s}(k_{\perp,\text{ref}}, k_{\parallel,\text{ref}}; z) = \frac{D_{A,\text{ref}}(z)^2 H(z)}{H_{\text{ref}}(z) D_A(z)^2} \left[ 1 + \beta(z) \frac{k_{\parallel}^2}{k^2} \right]^2 \times b_g^2 P_m^L(k; z) + P_{\text{sn}}, \quad (4)$$

where  $b_g$  is the linear bias parameter,  $\beta$  is the linear redshift-space distortion (RSD) parameter, defined as  $\beta \equiv (1/b_g) d \ln D / d \ln a|_z$  (Kaiser 1987),  $D$  is the linear growth rate,  $P_m^L$  is the linear mass power spectrum, and  $P_{\text{sn}}$  is a parameter to model the residual shot noise. We can use the BAO features in the linear power spectrum  $P_m^L$  as a standard ruler in order to constrain  $D_A(z)$  and  $H(z)$ . The BAO constraints are relatively robust against the galaxy bias uncertainty and the other nonlinearity effects, because none of the systematic effects introduces any particular length scale comparable with the BAO scale. Further, if we can use the shape and amplitude information in the galaxy power spectrum, we can constrain the growth rate as well as other cosmological parameters such as the neutrino mass and the primordial power spectrum parameters (Takada et al. 2006), as we will discuss below.

To make the parameter forecast, we have used the method developed in Seo & Eisenstein (2007). In this method, we include the smearing effect of the BAO features due to the bulk flow of galaxies in large-scale structure (Matsubara 2008; Taruya et al. 2009; Nishimichi & Taruya 2011). For the BAO survey of multiple redshift bins, the Fisher information matrix of model parameters can be computed as

$$F_{\alpha\beta} = \sum_{z_i} \int_{-1}^1 d\mu \int_{k_{\text{min}}}^{k_{\text{max}}} \frac{2\pi k^2 dk}{2(2\pi)^3} \frac{\partial \ln P_{g,s}(k, \mu; z_i)}{\partial p_{\alpha}} \times \frac{\partial \ln P_{g,s}(k, \mu; z_i)}{\partial p_{\beta}} V_{\text{eff}}(k; z_i) \times \exp \left[ -k^2 \Sigma_{\perp}^2 - k^2 \mu^2 (\Sigma_{\parallel}^2 - \Sigma_{\perp}^2) \right], \quad (5)$$

where  $\mu$  is the cosine between the wavevector and the line-of-sight direction,  $\mu \equiv k_{\parallel}/k$ ;  $\sum_{z_i}$  is the sum over different redshift bins;  $\partial P_{g,s}/\partial p_{\alpha}$  is the partial derivative of the galaxy power spectrum (Eq. 4) with respect to the  $\alpha$ -th parameter around the fiducial cosmological model; the effective survey volume  $V_{\text{eff}}$  and the Lagrangian displacement fields  $\Sigma_{\parallel}$  and  $\Sigma_{\perp}$  to model the smearing effect are given as

$$V_{\text{eff}}(k, \mu; z_i) \equiv \left[ \frac{\bar{n}_g(z_i) P_{g,s}(k, \mu; z_i)}{\bar{n}_g(z_i) P_{g,s}(k, \mu; z_i) + 1} \right]^2 V_{\text{survey}}(z_i) \quad (6)$$

$$\Sigma_{\perp}(z) \equiv c_{\text{rec}} D(z) \Sigma_0, \quad (7)$$

$$\Sigma_{\parallel}(z) \equiv c_{\text{rec}} D(z) (1 + f_g) \Sigma_0. \quad (8)$$

Here  $V_{\text{survey}}(z_i)$  is the comoving volume of the redshift slice centered at  $z_i$ ; the present-day Lagrangian displacement field is  $\Sigma_0 = 11 h^{-1} \text{Mpc}$  for  $\sigma_8 = 0.8$  (Eisenstein et al. 2007);

$D(z)$  is the growth rate normalized as  $D(z = 0) = 1$ ;  $f_g = d \ln D / d \ln a$ . The parameter  $c_{\text{rec}}$  is a parameter to model the reconstruction method of the BAO peaks (see below). In Eq. (5), we take the exponential factor of the smearing effect outside of the derivatives of  $P_{g,s}$ . This is equivalent to marginalizing over uncertainties in  $\Sigma_{\parallel}$  and  $\Sigma_{\perp}$ . The growth rate in  $\Sigma_{\parallel}$  or  $\Sigma_{\perp}$  takes into account the smaller smearing effect at higher redshift due to the less evolved large-scale structure. For the parameters, we included the cosmological parameters, the distances in each redshift slice, and the nuisance parameters:

$$p_{\alpha} = \{ \Omega_{\text{m}0}, A_s, n_s, \alpha_s, \Omega_{\text{m}0} h^2, \Omega_{\text{b}0} h^2, D_A(z_i), H(z_i), b_g(z_i), \beta(z_i), P_{\text{sn}}(z_i) \}, \quad (9)$$

where  $A_s$ ,  $n_s$  and  $\alpha_s$  are parameters of the primordial power spectrum;  $A_s$  is the amplitude of the primordial curvature perturbation, and  $n_s$  and  $\alpha_s$  are the spectral tilt and the running spectral index. The set of cosmological parameters determines the shape of the linear power spectrum. By using the method above, we can estimate the cosmological distance information solely from the BAO peaks, not from the broadband shape of the power spectrum. For the  $k$ -integration, we set  $k_{\text{min}} = 10^{-4} h/\text{Mpc}$  and  $k_{\text{max}} = 0.5 h/\text{Mpc}$  for all the redshift slices, but the exponential factor in Eq. (5) suppresses the information from the nonlinear scales. The Fisher parameter forecasts depend on the fiducial cosmological model for which we assumed the model consistent with the WMAP 7-year data (Komatsu et al. 2011).

Further, we assume that we can implement the promising method of Eisenstein et al. (2007) for improving the BAO measurements. Since the peculiar velocity field of galaxies in large-scale structure can be inferred from the measured galaxy distribution, the inferred velocity field allows for pulling back each galaxy to its position at an earlier epoch and then reconstructing the galaxy distribution more in the linear regime. As a result, one can correct to some extent the smearing effect in Eq. (5) and sharpen the BAO peaks in the galaxy power spectrum. Recently, Padmanabhan et al. (2012) implemented this method with real data from the SDSS DR7 LRG catalog, and showed that the reconstruction method can improve the distance error by a factor of 2. The improvement was equivalent to reducing the nonlinear smoothing scale from 8.1 to  $\Sigma_{\text{nl}} = 4.4 h^{-1} \text{Mpc}$ , about a factor 2 reduction in the displacement field. To implement this reconstruction method requires a sufficiently high number density of the sampled galaxies in order to reliably infer the peculiar velocity field from the measured galaxy distribution. Each redshift slice of the PFS survey (see Table 2) satisfies the requirement; the number density of galaxies in each redshift slice is higher than that of both the SDSS DR7 LRGs ( $\bar{n} \simeq 10^{-4} (h/\text{Mpc})^3$ ) and the BOSS LRGs ( $\bar{n} \simeq 3 \times 10^{-4} (h/\text{Mpc})^3$ ). Hence we can safely assume that the reconstruction method can be applied to the PFS BAO experiment. In the Fisher matrix calculation, we used  $c_{\text{rec}} = 0.5$  for an implementation of the reconstruction method<sup>20</sup>.

Finally, we have used the CMB information expected from the Planck satellite experiment, which gives a precise constraint on the sound horizon scale in order for us to use the BAO scale as a standard ruler. In addition to the cosmological parameters ( $\Omega_{\text{m}0}, A_s, n_s, \alpha_s, \Omega_{\text{m}0} h^2, \Omega_{\text{b}0} h^2$ ), we included, in the CMB Fisher matrix,  $\tau$  (the optical depth to the

<sup>20</sup> Then we found we can roughly reproduce the distance measurement accuracy for the SDSS LRGs as found in Padmanabhan et al. (2012).

last scattering surface) and  $D_A(z_{\text{CMB}})$  (the angular diameter distance to the last scattering surface). Then we can compute the Fisher matrix for the BAO experiment by adding the galaxy and CMB Fisher matrices;  $\alpha'\beta' = F_{\alpha'\beta'}^{\text{galaxy}} + F_{\alpha'\beta'}^{\text{Planck}}$ . The dimension of the Fisher matrix for the PFS survey in combination with the expected Planck information is  $38 \times 38$  (see Eq. 9). When further combined with the SDSS and BOSS BAO information, the dimension of the Fisher matrix increases accordingly.

Fig. 7 shows the expected accuracies of determining the angular diameter distance and the Hubble expansion rate in each redshift slice with the PFS cosmology survey (Table 2). The errors include marginalization over uncertainties of other parameters. The PFS forecasts can be compared with the accuracies of the existing and ongoing SDSS/BOSS surveys. As can be clearly seen, the PFS cosmology survey can constrain  $D_A(z)$  and  $H(z)$  over a wider range of redshift yet with similar precision to the SDSS and BOSS surveys. Even though the PFS area coverage is smaller than that of SDSS or BOSS surveys by a factor of 10 (1400 vs. 10000 sq. degrees), the PFS survey covers a factor 10 and 2 times larger comoving volume than the SDSS and BOSS surveys, respectively.

#### Cosmological implications:

It is worth noting that the BOSS survey will give the clustering statistics of the Lyman- $\alpha$  forest over  $2.1 \lesssim z \lesssim 3.4$ . PFS thus serves to fill a natural ‘gap’ in-between the galaxy and Lyman- $\alpha$  BAO experiments, allowing for probing the expansion history over the entire range of redshifts,  $0 \lesssim z \lesssim 3$ , i.e. through the period where it is believed that the cosmic expansion went from decelerated to accelerated phases. If we model the expansion history as parametrized by the dark energy model  $(w_0, w_a)$  (Linder 2003) and the curvature parameter  $(K)$ ,

$$H^2(z) = H_0^2 \left[ \Omega_{\text{m}0}(1+z)^3 - \frac{K}{H_0^2}(1+z)^2 + \Omega_{\text{de},0} a^{-3(1+w_0+w_a)} e^{3w_a(a-1)} \right], \quad (10)$$

we can propagate the distance measurement errors into the accuracies of estimating the parameters. To be more explicit, we can do this, based on the Fisher information matrix formalism, by projecting the BAO Fisher matrix into different parameter space:

$$F_{\alpha'\beta'} \equiv \frac{\partial \tilde{p}_a}{\partial p_{\alpha'}} F_{ab}^{\text{sub}} \frac{\partial \tilde{p}_b}{\partial p_{\beta'}}. \quad (11)$$

Here the new set of parameters  $\tilde{p}_{\alpha'}$  is given as  $\tilde{p}_{\alpha'} = (\Omega_{\text{de}0}, \Omega_{\text{m}0} h^2, \Omega_K, w_0, w_a)$ , which specifies the cosmic expansion history given by the above equation, and  $F_{ab}^{\text{sub}}$  is the sub-matrix computed by inverting the sub-matrix of the inverse of the full BAO matrix,  $[F^{-1}]_{\alpha\beta}$ , containing only the parts of the geometrical parameters,  $p_a = \{\Omega_{\text{m}0}, \Omega_{\text{m}0} h^2, D_A(z_i), H(z_i)\}$ . Hence the derived constraints on  $\tilde{p}_{\alpha'}$  include marginalization over other parameters such as the galaxy bias and the  $\beta$  parameters. Table 3 shows the expected accuracies of the dark energy parameters and the curvature parameter for the PFS survey. Here  $w_{\text{pivot}}$  is the dark energy equation state at the ‘pivot’ redshift, at which the dark energy equation of state is best constrained for a given survey. The quantity  $\text{FoM}_{\text{de}}$  is the dark energy figure-of-merit defined in the Dark Energy Task Force Report (Albrecht et al.

2006), which quantifies the ability of a given survey for constraining both  $w_0$  and  $w_a$ ;  $\text{FoM}_{\text{de}} \equiv 1/[\sigma(w_{\text{pivot}})\sigma(w_a)]$ , which is proportional to the area of the marginalized constraint ellipse in a sub-space of  $(w_0, w_a)$ . Table 3 clearly shows that the PFS BAO can significantly tighten the parameter constraints over the SDSS and BOSS surveys. Most interestingly, the PFS has the potential to constrain the curvature parameter to a precision of 0.3%. If we can detect a non-zero curvature, this would represent a *fundamental discovery* giving a critical constraint on the physics of the early universe, for example insight into different inflation scenarios (Efstathiou 2003; Contaldi et al. 2003; Freivogel et al. 2006; Kleban & Schillo 2012; Guth & Nomura 2012).

#### Nature of dark energy:

The parametrization  $(w_0, w_a)$  adopted for the dark energy equation of state samples only a narrow range of dark energy models. Given there is no well-accepted model for dark energy we seek to interpret our PFS data in a more model-independent way. The wide redshift coverage of PFS surveys, in combination with the SDSS and BOSS surveys, allows us to do this by directly reconstructing the dark energy density as a function of redshift solely based on the geometrical BAO constraints. To illustrate this, we use the Hubble expansion history parametrized in terms of dark energy density parameters in each redshift bins:

$$H^2(z) = H_0^2 \left[ \Omega_{\text{m}0}(1+z)^3 - \frac{K}{H_0^2}(1+z)^2 + \frac{\rho_{\text{de},z_i}(z \in z_i)}{\rho_{\text{cr}0}} \right], \quad (12)$$

where  $\rho_{\text{de},z_i}$  is the dark energy parameter in the redshift bin centered at  $z_i$ . For the combined BAO survey of SDSS, BOSS and PFS, we include the 9 dark energy densities,  $\rho_{\text{de}}(z_i)$ , given in 9 redshift bins (8 redshift bins of the galaxy surveys plus the redshift bin from 2.4 to  $z_{\text{CMB}}$ ). Then, similarly to the method described around Eq. (11), we can propagate the BAO-measured distance errors into the accuracies of reconstructing the dark energy densities in each redshift bin. Fig. 8 shows the result, where we assumed the cosmological constant,  $\rho_{\text{de}} = \text{constant}$ , as the fiducial model. The figure clearly shows that the PFS BAO survey is capable of reconstructing dark energy densities up to high redshift,  $z \simeq 2$  for a model in which  $\rho_{\text{de}}(z) \simeq \text{constant}$ , thereby testing various types of early dark energy models.

Further, we should emphasize that adding the PFS BAO measurements to the SDSS and BOSS information can significantly improve the reconstruction of dark energy density at low redshift, partly because the SDSS+BOSS BAO alone cannot break degeneracies between parameters  $(\Omega_{\text{m}0}, \Omega_{\text{m}0} h^2, K, \rho_{\text{de}}(z_i))$  given the distance measurements to the three redshifts ( $z_{\text{SDSS}}, z_{\text{BOSS}}, z_{\text{CMB}}$ ), and also because the angular diameter distances for the PFS redshifts are all sensitive to dark energy densities at low redshift via the integration relation between the angular diameter distance and the Hubble expansion rate. However, we should note that the constraint on the curvature parameter is significantly degraded in this case to  $\sigma(\Omega_K) = 0.057$  from the result in Table 3 because of the larger number of free parameters. Thus the accuracy of the curvature parameter is sensitive to which dark energy model we use for marginalization.

#### Testing the growth of structure:

We now turn to the utility of measuring the *redshift-space distortion (RSD) effect* and the broad-band shape of the galaxy power spectrum. If we can reliably model the RSD and the

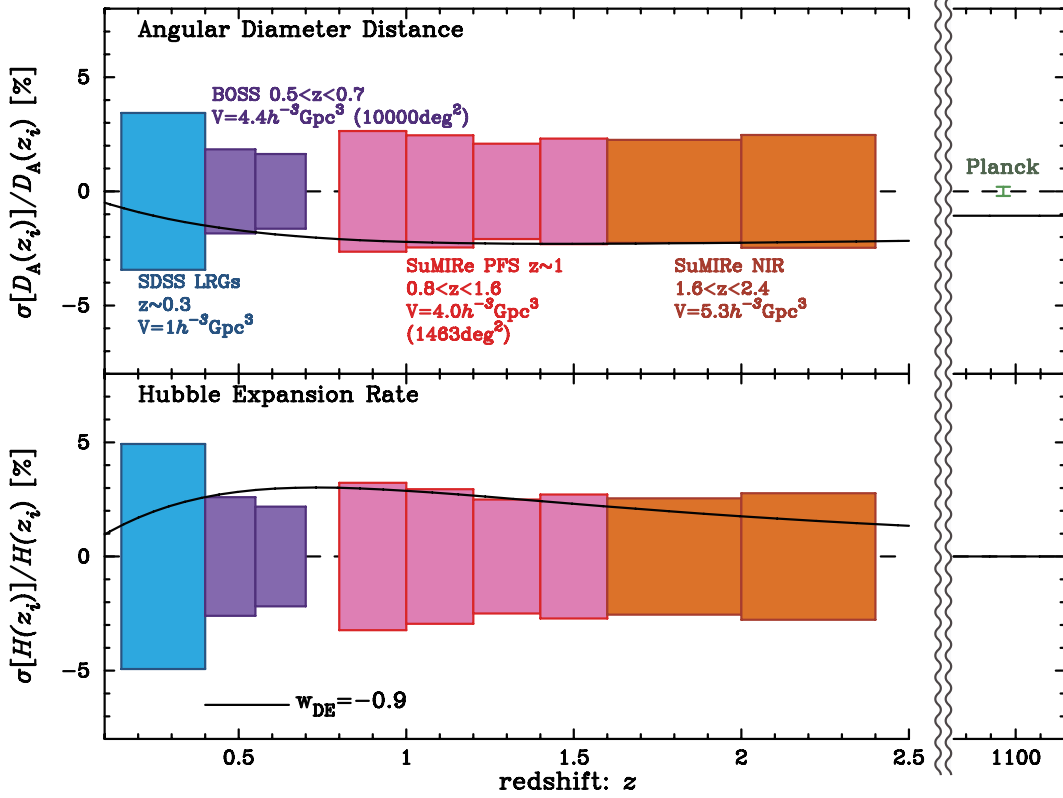


FIG. 7.— Fractional errors of determining the angular diameter distance and the Hubble expansion rate via the PFS BAO experiment (see Table 2) including marginalization over uncertainties of other parameters. The expected accuracies are compared to the existing and ongoing SDSS and BOSS surveys. The PFS survey will provide geometrical constraints to higher redshift than the SDSS and BOSS surveys, but with comparable precision. The solid curve in each panel shows the fractional difference when changing the dark energy equation of state parameter from the fiducial model  $w = -1$  to  $w = -0.9$ .

TABLE 3  
FORECASTED ACCURACIES OF COSMOLOGICAL PARAMETERS

Survey	$\Omega_{\text{de}0}$	$w_{\text{pivot}}$	$w_a$	FoM <sub>de</sub>	$\Omega_K$	$m_{\nu,\text{tot}}$ [eV]	$f_{\text{NL}}$
SDSS+BOSS	0.0061	0.076	1.2	11	0.0071	0.188	16
SDSS+BOSS+PFS	0.0051	0.059	0.36	47	0.0030	0.133	11

NOTE. — The constraints on  $\Omega_{\text{de}0}$ ,  $w_{\text{pivot}}$ ,  $w_a$  and  $\Omega_K$  ( $\equiv -K/H_0^2$ ) are from the BAO distance measurements in Fig. 7, i.e. not including the information on the broadband shape of the galaxy equation spectrum. Note that  $w_{\text{pivot}}$  is the dark energy equation state at the “pivot” redshift, at which the dark energy equation state parameter is best constrained for the given PFS BAO measurements. The constraints on the neutrino mass  $m_{\nu,\text{tot}}$  and  $f_{\text{NL}}$  are derived by including the broadband shape information. See text for the details.

shape of the power spectrum in the weakly nonlinear regime including a possible scale-dependent bias, we can use this information not only to improve the cosmological constraints (Takada et al. 2006), but also to constrain the growth rate which is sensitive to theory of gravity on cosmological scales. Encouraging progress is being made via many efforts to develop a more accurate model of the redshift-space power spectrum in the weakly nonlinear regime (see Fig. 6) (Matsubara 2008; Taruya et al. 2009; Nishimichi & Taruya 2011; Tang et al. 2011; Hikage et al. 2012).

To estimate the power of the PFS survey, we use the linear theory prediction for the amplitude of the RSD effect,  $\beta(z) = f_g(z)/b_g(z)$ , in Eq. (4), where  $f_g$  is defined by the growth rate as  $f_g \equiv d \ln D / \ln a$ . Then we can include the RSD effect in the Fisher matrix formalism by using  $f_g$  in each redshift slice instead of treating  $\beta$  as parameters (see Eqs. 4

– 9). With this implementation, we can break degeneracies between the RSD effect  $f_g/b_g$  and the galaxy bias uncertainty  $b_g$  from the measured anisotropic modulations in the redshift-space galaxy power spectrum. Then we can in turn use the amplitude and shape information of the underlying linear power spectrum.

Fig. 9 shows the expected accuracies of constraining the growth rate,  $f_g (= d \ln D / d \ln a)$ , in each redshift slice via the RSD measurements. The PFS survey can constrain the growth rate in each redshift to a 6% accuracy. In particular, PFS will provide accurate constraints on the growth rate at redshifts beyond  $z = 1$ , when the cosmic expansion is in its decelerated phase. Such constraint are very important for testing whether dark energy is an illusion caused by an incomplete understanding of General Relativity.

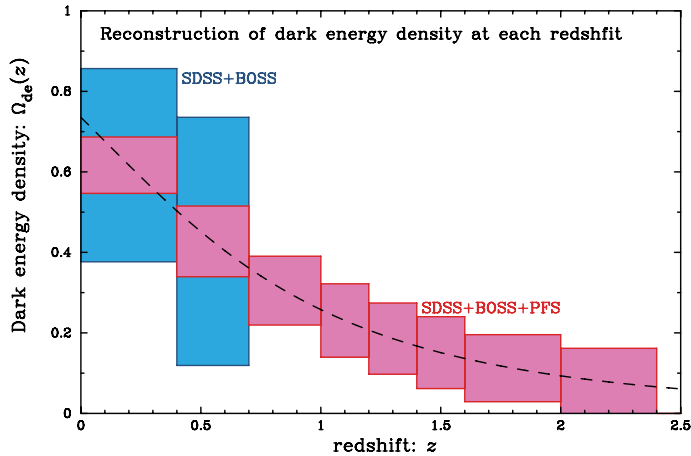


FIG. 8.— Expected accuracy of reconstructing the dark energy density parameter at each redshift,  $\Omega_{\text{de}}(z) \equiv \rho_{\text{de}}(z)/[3H^2(z)/8\pi G]$  from the BAO-measured  $D_A(z)$  and  $H(z)$  in Fig. 7. Here we considered the cosmological constant ( $\rho_{\text{de}}(z) = \rho_{\text{de}0} = \text{constant}$ ) and the flat universe ( $\Omega_K = 0$ ) as the fiducial model. Adding the PFS BAO constraints to the SDSS and BOSS constraints enables reconstruction of the dark energy density to  $z \simeq 2$ , and also significantly improves the precision at low redshifts, as the comoving distance at the high redshift arises from an integration of  $H(z)$ .

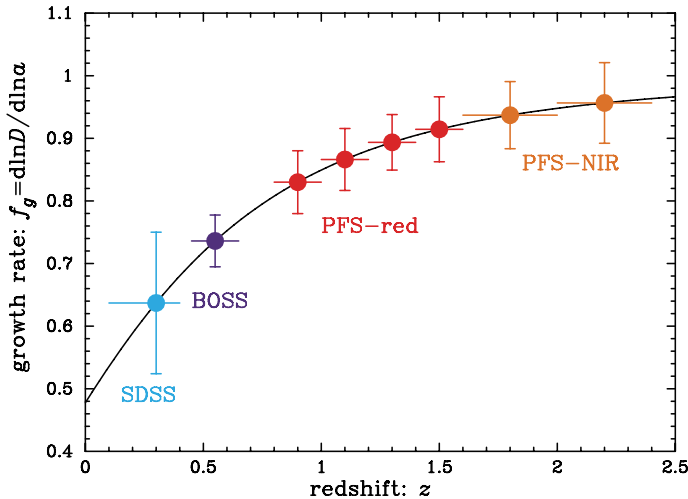


FIG. 9.— Marginalized errors of reconstructing the growth rate,  $f_g \equiv d \ln D / d \ln a$ , in each redshift slice.

#### Other constraints:

With the growth rate constraints and the information on the shape of the galaxy power spectrum, we can also constrain other interesting parameters such as the sum of neutrino masses ( $m_{\nu, \text{tot}}$ ) and the degree of primordial non-Gaussianity ( $f_{\text{NL}}$ ). Primordial non-Gaussianity induces a characteristic scale-dependent biasing effect on the galaxy distribution at very large scales (Dalal et al. 2008) that are well in the linear regime and cannot be explained by other nonlinearity effects. Hence we can use the largest-scale signal of galaxy clustering to explore the signature of the primordial non-Gaussianity. Table 3 shows the expected accuracy of constraining  $f_{\text{NL}}$  to an accuracy of  $\sigma(f_{\text{NL}}) \simeq 11$ . PFS does not have a comparable power of constraining  $f_{\text{NL}}$  to the constraints expected from other probes such as the Planck experiment ( $f_{\text{NL}} \sim 5$ ) due to the relatively small area coverage, which limits the access to the largest-length scales.

On the other hands, the neutrinos of finite mass scale, as found by terrestrial experiments, cause a suppression in the galaxy clustering power on scales smaller than the neutrino free-streaming scale, which imprints a characteristic scale-dependent effect on the galaxy power spectrum (Takada et al. 2006). The amount of the suppression effect scales with the sum of neutrino mass as  $\Delta P_g / P_g \simeq -8\Omega_{\nu 0} / \Omega_{\text{m}0} \simeq -8m_{\nu, \text{tot}} / (94.1 \text{ eV} \Omega_{\text{m}0} h^2)$ ; the neutrinos of  $m_{\nu, \text{tot}} = 0.1 \text{ eV}$ , close to the lower bound of the inverted neutrino mass hierarchy, leads to about 6% suppression in the galaxy power spectrum compared to the case without the massive neutrinos. Hence, we can use the measured clustering amplitude to constrain the neutrino mass. However, the achievable precision of neutrino mass depends on the level of our understanding on the nonlinear power spectrum including the galaxy bias uncertainty (Saito et al. 2008, 2009). Here, by assuming that an accurate model of the galaxy power spectrum is available, we estimate the power of PFS for constraining the neutrino mass. To be more precise, we assumed that the following set of parameters, instead of Eq. (9), can model the redshift-space galaxy power spectrum based on the extended perturbation theory based method in combination with numerical simulations:

$$p_\alpha = \{\Omega_{\text{m}0}, A_s, n_s, \alpha_s, \Omega_{\text{m}0} h^2, \Omega_{\text{b}0} h^2, \Omega_K, w_0, w_a, m_{\nu, \text{tot}}, b_g(z_i), P_{\text{sn}}(z_i)\}. \quad (13)$$

In this parameter estimation we did not use the reconstruction method (i.e., set  $c_{\text{rec}} = 1$  for the reconstruction parameter in Eq. 8), because the reconstruction method of BAO peaks alters the shape and amplitude of power spectrum. With this implementation, we can include the shape and amplitude information of the power spectrum for constraining the cosmological parameters, marginalized over uncertainties of the nuisance parameters. As can be found from Table 3, the PFS survey can achieve a precision of  $\sigma(m_{\nu, \text{tot}}) \simeq 0.13 \text{ eV}$ .

#### Synergy with HSC:

Finally we note there will be many synergistic opportunities enabled by the fact that the PFS survey will be undertaken in the same sky areas as the HSC imaging survey. Weak lensing information from HSC will be very effective in correcting and calibrating systematic effects inherent in the galaxy clustering analysis, the nonlinear redshift-space distortion and the galaxy bias uncertainty, up to the  $z \sim 2$  slice (Hikage et al. 2012; Nishizawa et al. 2012). The spectroscopic data from PFS survey can likewise be used to calibrate the photo- $z$  errors or the redshift distribution of HSC imaging galaxies, which is one of the major uncertainties in the HSC cosmology. Thus, by combining the HSC imaging and PFS spectroscopic surveys, we can significantly improve the cosmological constraints making the joint HSC and PFS experiments comparable to a Stage-IV Dark Energy experiment in the parlance of recent US studies.

#### 2.3. Scientific Requirements for PFS Cosmology Survey

As discussed above, PFS has the unique capability to execute a very powerful cosmology survey across a wide range of redshifts, extending considerably current and planned BAO surveys on  $\leq 4 \text{ m}$ -class telescopes. Here we summarize the survey and instrumental requirements for the cosmological applications. These requirements are listed in Tables 4 and 5. We regard these as minimum requirements and, of course, where possible will strive to improve upon these subject to cost and schedule impact.

TABLE 4  
COSMOLOGY SURVEY REQUIREMENTS

Science yield requirements	
Distance measurements	$\lesssim 3\%$ measurement of $D_A(z)$ and $H(z)$ in each of 6 redshift bins via BAO (0.8–1.0, 1.0–1.2, 1.2–1.4, 1.4–1.6, 1.6–2.0, and 2.0–2.4)
Dark energy reconstruction	$\lesssim 7\%$ measurement of $\Omega_{\text{de}}(z)$ in each of 6 redshift bins via BAO
Curvature	Measure $\Omega_K$ to $\lesssim 0.3\%$ via BAO
Growth of structure	$\lesssim 6\%$ measurement of the growth rate of structure in each of 6 bins via RSD
Galaxy catalog requirements	
Redshift range	$0.8 \leq z \leq 2.4$ ( $0.8 \leq z \leq 1.6$ minimum)
Number density of galaxies	$\geq 2900 \text{ deg}^{-2}$
$dN/dz$ of ELGs	$\bar{n}_g P_g > 1$ ( $0.8 < z < 1.6$ ) or $\bar{n}_g P_g > 0.5$ ( $1.6 < z < 2.4$ ) at $k = 0.1 h/\text{Mpc}$
Total survey area	$\geq 1400 \text{ deg}^2$
Incorrect redshift fraction	$< 1\%$
Redshift precision, accuracy	$\Delta z/(1+z) < 0.0007$ , $1\sigma$ ( $\sigma_v < 200 \text{ km/s}$ )
Survey geometry	Width $> 7.5$ degrees; $\leq 4$ contiguously-connected survey regions
Survey implementation requirements	
Total nights	$\approx 100$ clear nights
Lunar phase	Dark (1 of 2 visits) or age $< 7$ days (other visit)
Imaging survey	HSC <i>gri</i> data to $\approx 26$ th magnitude AB ( $5\sigma$ )

TABLE 5  
PFS INSTRUMENT REQUIREMENTS

Wavelength coverage	$650 \leq \lambda \leq 1300\text{nm}$ ( $650 \leq \lambda \leq 1000\text{nm}$ minimum)
Number of fibers	2400
Overhead	$< 0.2 \times$ the open-shutter time
Throughput	Average $> 22\%$ (red) or $> 24\%$ (NIR) Worst part of band, $> 20\%$ (red) or $> 18\%$ (NIR) (Excludes atmosphere, central obscuration + WFC vignetting, and fiber aperture effect.)
Fiber aperture factor	Encircled energy in fiber is $\geq 59\%$ (point source) or $\geq 45\%$ (galaxy, $r_{\text{eff}} = 0.3''$ ) (Equivalent to $0.8''$ FWHM seeing + $11 \mu\text{m}$ rms/axis additional aberration + $0.12''$ fiber offset.)
Spectrograph image quality	$\leq 14 \mu\text{m}$ rms per axis (excluding fiber geometric size, pixel tophat, and internal defocus due to thickness of red CCD)
Spectral resolution	Red: $R \sim 3000$ ; NIR: $R \sim 4000$ (to resolve out OH lines but limit read noise)
Stray light	Near OH lines: Lorentzian wings at $\leq 3 \times$ amplitude of perfect grating Diffuse: equivalent to $\leq 2\%$ of total sky brightness spread over detector
Read noise	$\leq 3$ (red) or $\leq 4$ (NIR) $e^-$ rms per pixel (If the NIR channel is not reset between exposures, $\leq 4\sqrt{2}$ $e^-$ rms is acceptable.)
Sky subtraction accuracy	$< 1\%$ of sky background per 4-pixel resolution element

### 3. GALACTIC ARCHAEOLOGY: NEAR-FIELD COSMOLOGY

*Summary: The nature of dark matter and its role in galaxy formation are best tested on the scale of, or below, an individual galaxy. We propose a PFS survey of ancient resolved stars in the Milky Way and in the Andromeda Galaxy (M31) to address this question. There is significant tension between the predictions of the standard Cold Dark Matter cosmogony and the observations of galaxies on small scales, such that one must appeal either to a baryonic or dark matter solution. As the baryonic physics governing how galaxies formed and evolved can be traced by the properties of stars of all ages, including those from the earliest epochs, PFS can contribute fundamentally to this area of near-field cosmology.*

*Our proposed PFS Galactic Archaeology (GA) Survey aims to measure radial velocities and metallicities for a large sample of stars, in synergy with both HSC and the ESA space mission Gaia. It can be viewed as an extension of SDSS/SEGUE, going significantly deeper. The targets consist of ancient Galactic stars belonging to the stellar halo and disks, both in the smooth components and in streams and satellites, and bright red giants in the halo of M31. Our proposed survey makes full use of the current spectrograph design, i.e. resolving power of  $R = 2,000$  to  $3,000$ , wavelength cover-*

*age of  $3,800 \text{ \AA}$  to  $9,000 \text{ \AA}$  with 2,000-3,000 fibers per PFS field. Importantly, it has already been demonstrated by the SDSS/SEGUE team that stellar spectra we will obtain with this resolution can provide the necessary high quality data for our science.*

#### 3.1. Galactic Archeology Objectives

Our understanding of how galaxies like the Milky Way and M31 formed and evolved in the expanding Universe remains enigmatic. The current paradigm of cosmic structure formation based on Cold Dark Matter (CDM) models proposes that galaxy formation is driven by hierarchical assembly of dark matter halos, starting from sub-galactic scales. The repeated merging and overall clustering of many small dark halos over cosmic time forms a larger, galaxy-sized halo. The associated cooling and collapse of baryonic matter confined in the dark halos at each stage of the hierarchy forms the visible galaxies, with the morphology of the final galaxy set by the physics of star formation and of the merging process. Indeed, mergers are predicted to play a key role in the creation of stellar halos, bulges, thick disks and even some parts of thin disks.

However, CDM models have encountered several fundamental difficulties in explaining observations on galactic scales consistent with an excess of small scale power. One

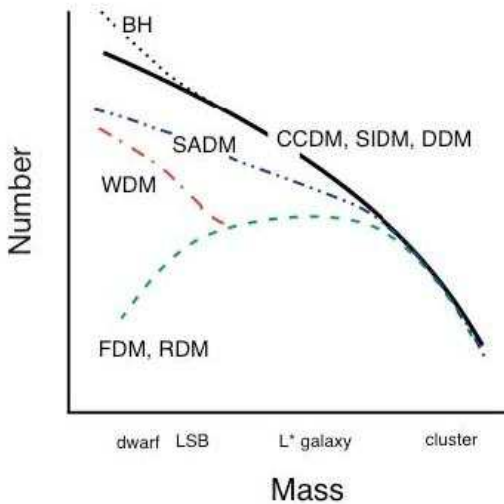


FIG. 10.— An illustration of how the number of objects of a given type depends on their present day mass for different dark matter models (Ostriker & Steinhardt 2003) including Collisionless Cold dark matter (CCDM), Strongly Self-Interacting dark matter (SIDM), Warm dark matter (WDM), Repulsive dark matter (RDM), Fuzzy dark matter (FDM), Self-Annihilating dark matter (SADM), Decaying dark matter (DDM) and Massive Black Holes (BH). Observations on small scales are key to distinguishing these.

of the most serious issues is the prediction of many more subhalos in a Milky Way-sized system than the modest number of visible satellites. This discrepancy can only be reconciled if the vast majority of small halos are dark. They would then only reveal their presence through their dynamical effects on visible systems. Our understanding of the star formation process on these small scales, which correspond to dwarf satellite galaxies, remains limited, so there may well be a large population of dark satellites. Alternatively, the assumption of collisionless CDM models may not be correct (Ostriker & Steinhardt 2003, see Fig. 10 for the predictions of various dark matter models). The merging history of the ‘building blocks’ of galaxies is determined by the power spectrum, i.e. by the nature of dark matter, and this we plan to investigate through the study of the stellar populations in both the Milky Way and M31.

Our primary science goal with Subaru/PFS is thus to test the assembly process of CDM on Galactic scales, by dedicated observations of old stars nearby, formed at high look-back times. Resolved ancient stars in the Milky Way and other Local Group galaxies are ideal targets because they offer us our most detailed views of galactic structure and evolution through their kinematics and chemical abundances (Freeman & Bland-Hawthorn 2002). Kinematics of stars reflect past galaxy collapse and/or merging events and their distribution in phase space as defined by integrals of motion such as angular momentum remains basically unchanged (Fig. 11). The chemical abundances of stars reflect their past star-formation history and chemical evolution, possibly in association with the dynamical state of proto-galactic clouds such as their collision and merging. All of these processes are actually controlled by hierarchical clustering of CDM via self-gravity on galactic and sub-galactic scales. Thus, to assess what CDM models predict, it is essential to derive the spatial distribution of dark matter subhalos in the Galaxy and Andromeda through their dynamical effects on visible stellar systems. Stars are indeed ideal tracers of a background gravitational field dominated by dark matter.

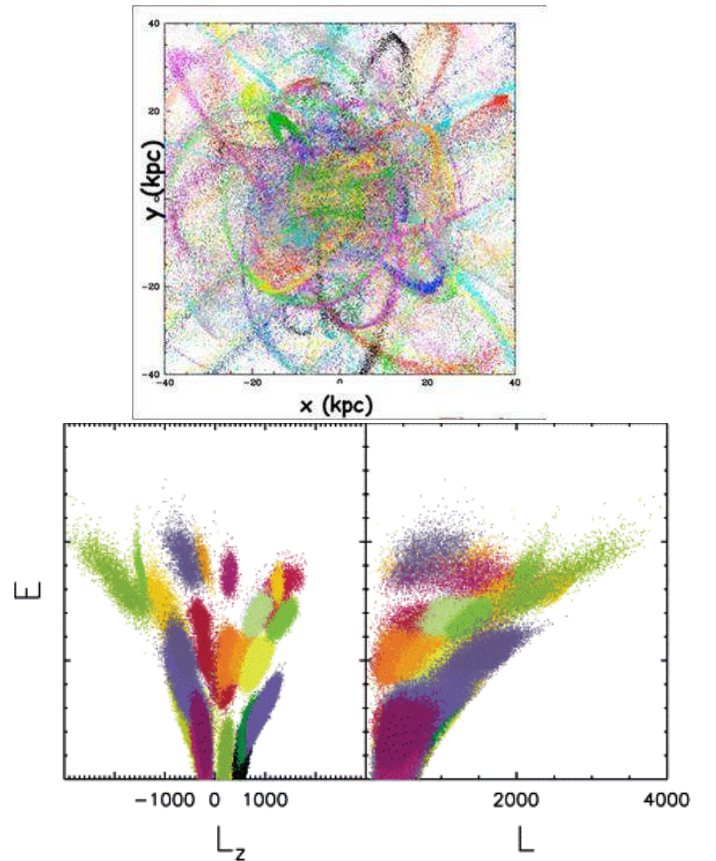


FIG. 11.— Left: Model distribution of tidal streams in spatial coordinates where the different colors represent different satellites (from Freeman & Bland-Hawthorn 2002). These stream-like features disappear after several dynamical times. Right: Model distribution of nearby stars in the integrals of motion space, i.e.,  $E$  vs.  $L_z$  and  $E$  vs.  $L$ , based on numerical simulations of falling satellites into the Milky Way (from Helmi & Zeeuw 2000). The different colors represent different satellites. Shown is the final distribution of stars after 12 Gyr within about 6 kpc from the Sun, after convolution with the errors expected for Gaia. It is clear that each of the progenitor galaxies can be traced via the current phase space distribution.

To make progress we propose to obtain spectra for about a million stars in the Milky Way and Andromeda, as one component within the framework of the proposed PFS Subaru Strategic Program. These spectroscopic studies will be in perfect synergy with the upcoming astrometric satellite, Gaia, that will provide very precise measurements of distances and proper motions for Galactic stars, and the HSC survey which will provide the essential large imaging data set. Therefore, PFS, in combination with Gaia and HSC, will provide us with unique data in the area of near-field cosmology. With these data we hope to gain an ultimate understanding of the nature of dark matter and the associated galaxy formation processes.

The main questions we seek to address in our dedicated Galactic Archaeology (GA) survey are summarized as follows.

1. *What is the merging history of the Milky Way? – addressing the role and nature of dark matter in galaxy formation.*
2. *How did the old Galactic components (thick disk and stellar halo) form? – addressing baryonic physics in the context of CDM.*

3. *How does M31 differ from the Milky Way? – contrast merging and baryonic processes on small scales in two systems.*

3.2. *PFS Galactic Archaeology Survey*

A summary of our GA survey plan is shown in Table 6. Its primary goal is to measure radial velocities and overall metallicities for about a million stars belonging to the field stellar halo and thick disk in the Milky Way, together with stars associated with substructure – streams and satellites – and bright red giant stars in a wide area of M31’s halo, along its minor axis. Our proposed survey will allow metallicities to be determined to  $\sim 0.2$  dex using the SDSS/SEGUE stellar-parameter pipeline (as detailed below) and radial velocities to a few  $\text{km s}^{-1}$ . The survey comprises two parts.

3.2.1. *The Milky Way Survey*

The primary targets in this survey lie in the old stellar components of the Milky Way. PFS will measure spectra of stars with  $17 < V < 21.5$  mag, thereby complementing data from Gaia. The Gaia mission will provide astrometric observations for  $\simeq 1$  billion stars with a precision of 12-25  $\mu\text{as}$  for  $V < 15$  and 300  $\mu\text{as}$  for  $V < 20$ , whereas radial velocities and metal abundances will only be measured for bright stars with  $V < 17$  and  $V < 12$ , respectively. The Milky Way survey is therefore primarily aimed at obtaining radial velocities and metal abundances for two samples. In the first *Gaia sample*, we will select stars in the magnitude range of  $V < 20$  mag, for many of which accurate distances and full spatial motions will be available by the time of our PFS survey and the full final data will be released by 2022. Targeting F/G dwarf stars is especially important to densely map the phase space distribution and find kinematic streams (Fig. 11) within distances of  $\sim 10$  kpc from the Sun. In the second *Faint sample*, PFS will target stars beyond the Gaia astrometry limit, i.e., with  $V > 20$  and as faint as  $V = 21.5$  to map the dense phase-space distribution up to 30 kpc and to reach very distant, giant stars at more than 100 kpc. This sample is selected from stars associated with halo substructures in the form of stellar streams (Sagittarius Stream and Orphan Stream) and those in the outskirts of the closest ultra-faint Galactic dSph (Segue I and associated 300  $\text{km s}^{-1}$  stream). This sample also targets general field stars located in the outer-most parts of the disk and halo from beyond the range of Gaia ( $V > 20$ ) to the PFS limit, which corresponds to a distance range from 60 to 130 kpc for a luminous giant, and from 100 to 200 kpc for a HB or RR Lyr star. Measurements of radial velocities as well as metal abundances of these stars will set important constraints on chemo-dynamical properties of the outer reaches of the disk and halo.

This PFS survey will complement the on-going Gaia-ESO Survey with VLT in the Southern hemisphere. Gaia-ESO is a dedicated spectroscopic survey, led by G.Gilmore, targeting  $\geq 10^5$  stars, systematically covering the various structural components of the Galaxy, providing homogeneous data of radial velocities and elemental abundances also in synergy with Gaia astrometry. Based on high-resolution spectra taken from two wavelength windows ( $R = 19,800$  for 5339-5619  $\text{\AA}$  and  $R = 16,200$  for 8484-9000  $\text{\AA}$ ) and 110 science fibers, the survey is measuring multi-element chemical abundances of stars over 300 nights. The team has made significant efforts to define spectroscopic standard fields, some of which are equatorial and so can be accessed from Mauna Kea.

We now discuss the two components of our PFS Milky Way survey in more detail:

(i) *Gaia sample:*

The justification for studying around a million stars in synergy with Gaia is as follows. For mapping of the phase-space distribution for different stellar populations, we assume that the stellar masses of the building blocks for the halo/thick disk range from  $10^3$  to  $10^7 M_{\odot}$  as deduced from the luminosities of Galactic satellites (e.g., Belokurov et al. 2006). Then the stellar halo whose total mass is  $\sim 10^9 M_{\odot}$  is comprised of about  $\sim 10^4$  building blocks (assuming a power law mass function with index in the range  $-1.8$  to  $-1.5$ ). If at least 100 member stars are needed for each building block to characterize its velocity and metallicity distribution with 10 % statistical significance, we need to observe  $\sim 1$  million stars in total.

For separating and characterizing each of the Galactic components through its velocity, space and metallicity distributions, we require at least 40 velocity bins for  $-200$  to  $200 \text{ km s}^{-1}$  with  $\Delta v = 10 \text{ km s}^{-1}$ , 100 spatial positions with 10 bins for each of two dimensional  $(R, z)$ ,  $(b, l)$ , or (along, perpendicular to) the line of sight, and 2 to 3 metallicity ranges. Again, provided that at least 100 stars at each velocity bin are needed to characterize its velocity distribution with 10 % statistical significance, we require a sample of a million stars in total.

This science is most robustly achieved with F/G-type dwarf stars at distances up to 10 kpc, i.e., consisting of both halo and disk stars in roughly equal proportions. Based on accurate space motions and overall metallicities available for these stars, phase-space and metallicity distributions of each of the stellar systems/substructures can be derived. As detailed below (see Fig. 16), we will have about 300 F/G dwarfs at  $l = 180^\circ$  per PFS field per 2 magnitude interval in the relevant magnitude range, suggesting about 500 F/G dwarfs per PFS field for  $17 < V < 20$ . To enable ancillary science using other stellar populations, no color cut will be adopted for the Gaia sample. Many of these additional subsamples will contain stars in the boundary of inner/outer halo at around  $r \sim 20$  kpc whose full spatial motions will be determined for the first time. Such data will provide an excellent tracer of the underlying gravitational potential dominated by the dark halo and hence the density distribution of dark matter in its inner part of  $r < 20$  kpc (e.g., Holmberg & Flynn 2000; Garbari et al. 2011; Smith et al. 2012).

To acquire the necessary data for as many as 1 million stars, the total survey area must be at least  $\sim 400$  sq. degree ( $\sim 300$  PFS pointings) at  $b \sim 30$  deg, in which  $\sim 55$  %,  $\sim 40$  % and  $\sim 5$  % belong to the halo, thick disk and thin disk, respectively. We require spectra with a  $S/N \sim 30$  per resolution element at  $\lambda = 5000 \text{ \AA}$  for precisions in metal abundance to 0.2 dex and radial velocity to a few  $\text{km s}^{-1}$ , on the basis of the SDSS/SEGUE calibration method as detailed below.

(ii) *Faint sample:*

The Milky Way halo contains numerous tidally elongated stellar streams covering the sky, as depicted in Fig. 12 (Belokurov et al. 2006). The most impressive feature is the stream emanating from the Sagittarius dSph galaxy together with a second, fainter stream nearby. The Sgr dSph galaxy has been hailed as the ‘Rosetta Stone’ for the merging processes since its discovery in 1994 (Ibata et al. 1994) but we still do not understand its detailed origin (for example, how many orbits it has been losing material) or the kinematics and metallic-

TABLE 6  
SUMMARY OF GALACTIC ARCHAEOLOGY SURVEY

Survey	Magnitude range (mag)	Area (deg <sup>2</sup> )	No. Fields	Survey Time (nights)	Comments
LR-mode survey:					
1. The Milky Way	$17 < V < 21.5$		(208)		(1) $b = 30, 0 < l < 270$
			(46)		(2) $b = -30, 60 < l < 120$
			(10)		(3) $b = 60, l = 90$
			(12)		(4) Outer disk $l = 180$
			(24)		(5) 'Field of Streams'
		390	300	75	Sum of (1)-(5)
2. M31 halo	$21.5 < V < 22.5$	65	50	30	HSC sample
Total		455	350	105	

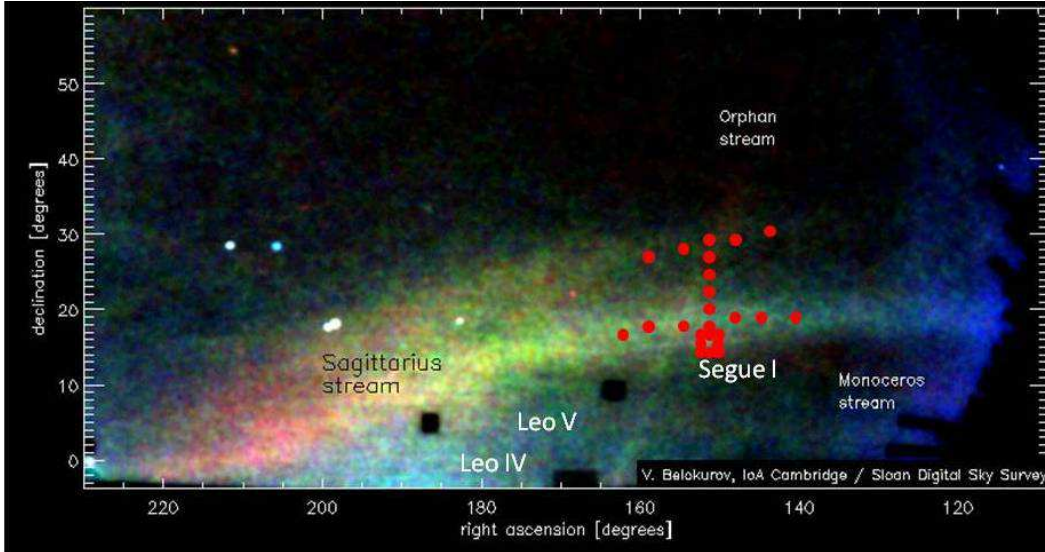


FIG. 12.— Stellar substructures revealed in the SDSS imaging data (taken from Belokurov et al. 2006), and proposed PFS pointings (filled red circles) over these streams and the surroundings of the faint satellite, Segue I.

ity distribution of the associated streams. Although the lower stream appears to represent tidal material from the Sgr dSph, the upper stream cannot be explained currently (e.g., Fellhauer et al. 2006; Penarrubia et al. 2010) (see also Koposov et al. 2011, for the extension of these streams in the Southern Galactic hemisphere). The Orphan Stream is another striking feature. Although numerous faint dSphs have been revealed by SDSS in its general vicinity, its origin remains unclear.

To better understand the origin and dynamical importance of these streams and their association with satellite galaxies, or more generally, with building blocks and their assembly process of the stellar halo, PFS will undertake a comprehensive chemo-dynamical mapping of the region containing the Sgr Stream, Orphan Stream and the outskirts of Segue I (Fig. 12). This satellite galaxy shows an extended stellar distribution possibly due to tidal interaction and/or overlapping fore/background stellar populations (see Belokurov et al. 2008; Simon et al. 2010, for more details). Recently Carlin et al. (2012) suggested that Segue I may be associated with the tidal disruption of the progenitor galaxy of the Virgo Overdensity.

In addition to such faint, known substructures beyond the reach of Gaia, large parts of the Galactic components especially at the faint limits are still unexplored. Examples include the outer parts of the thin disk at  $l = 180^\circ$ , where Monoceros stream (which is a Northern hemisphere target) is located, as yet unidentified kinematically cold struc-

tures at high Galactic latitudes at  $b \sim 60^\circ$ , the interface of halo/disk/bulge components and more. Subaru/PFS will allow us to measure detailed velocity distributions of these faint parts of the Galactic components. By the time of the PFS survey, proper motions available from ground-based imaging survey, such as PanSTARRS, combined with the photometric distance obtained from the stellar parameters will provide us with the six dimensional phase space distribution at distances beyond those reached by Gaia.

We propose to observe a total area of  $\sim 390$  sq. degree ( $\sim 300$  pointings) covering all the survey fields for both the Gaia and faint samples. Survey fields include stripes along constant Galactic latitudes at around  $b = 30^\circ$  with  $0^\circ < l < 270^\circ$  (208 pointings) and  $b = -30^\circ$  with  $60^\circ < l < 120^\circ$  (46 pointings), high latitude fields ( $b = 60^\circ$ ) at  $l = 90^\circ$  (10 pointings), the outer-disk fields at  $l = 180^\circ$  (12 pointings) and the Field of Streams (24 pointings). A total of  $\sim 75$  nights is required assuming 2 hr exposures to obtain  $S/N \sim 30$  spectra for stars with  $V = 21.5$  mag and that 4 fields per night are observed. For the brighter stars with  $V < 20$ , grey time can be used.

### 3.2.2. The M31 halo survey

The primary targets in the M31 survey are bright red giants with  $21.5 < V < 22.5$  mag, i.e., stars around the tip of the RGB with  $I \simeq 20.5$  selected along the minor axis of the galaxy (Fig. 13). Pre-imaging observations and selec-



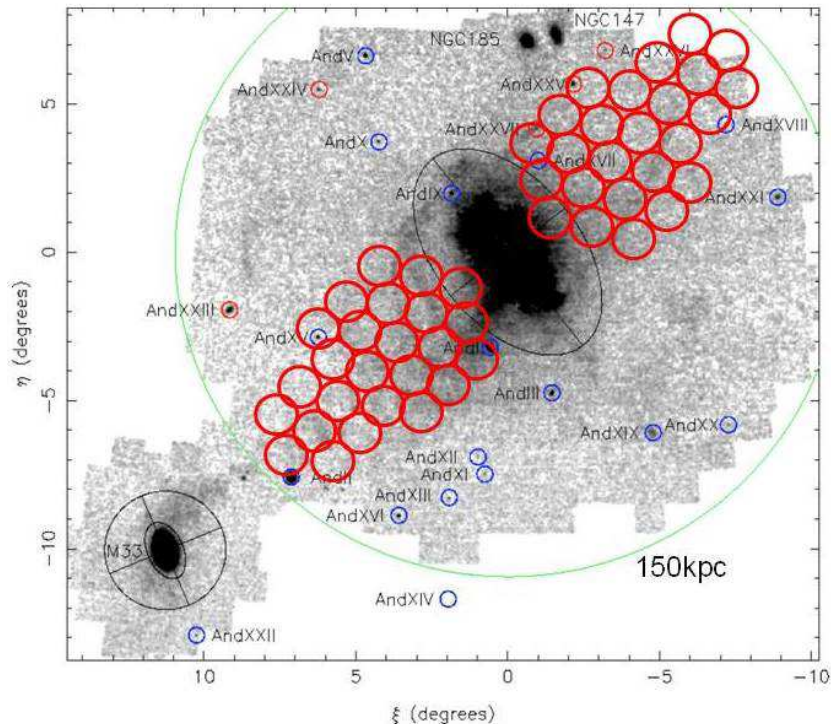


FIG. 13.— Proposed PFS pointings along the minor axis of M31’s halo ( $\sim 50$  pointings), in which several stellar streams are included. The map of RGB stars is taken from Richardson et al. (2011).

tion of the candidate halo giants will be provided by an HSC imaging survey and we will utilize a newly-developed narrow-band filter (NB515 filter with  $CW = 5145 \text{ \AA}$  and  $BW = 80 \text{ \AA}$ , which is similar to the DDO51 filter<sup>21</sup>), to assist in removing foreground Galactic dwarfs. A survey along the minor axis will enable us to derive the chemo-dynamical properties of the general M31 halo as well as to study in detail several stellar streams, including a cold stream-like feature in the north-west part of the halo, part of which corresponds to Stream F discovered by previous Subaru observations (Tanaka et al. 2010). The distribution of stars along these M31 streams will be especially useful in constraining the number of orbiting dark matter subhalos, which induce visible density variations along the stream through dynamical disturbances (Carlberg 2011). A careful subtraction of foreground Milky Way stars through spectroscopic observations will be crucial for constraining the number of orbiting CDM subhalos in Andromeda and comparing with theoretical predictions.

PFS will measure radial velocities and metal abundances for M31 halo stars to set important constraints on their intrinsic chemo-dynamical properties. Individually-determined spectroscopic metallicities will represent a major advance over those derived photometrically or by stacking spectra. To estimate the number of RGB stars in the M31 halo per PFS field, we follow the recent observations with Keck/DEIMOS by Gilbert et al. (2012), in which the pre-selection of candidate RGB targets using the DDO51 filter was made. At a projected distance of 80 kpc from the M31 center, we expect  $\sim 2600$  objects per PFS field (including significant foreground/background contamination even after NB515 pre-

selection), among which about 100 secure RGB stars of the M31 halo can be extracted. We propose to observe  $\sim 66$  sq. degrees ( $\sim 50$  pointings) as shown in Fig. 13. In order to obtain spectra with  $S/N \simeq 20$  per resolution element at  $\lambda = 5000 \text{ \AA}$ , 5 hr exposures are required at  $V = 22.5$  mag. Thus,  $\simeq 30$  nights are required for this component of the survey.

### 3.3. Deriving stellar atmospheric parameters from PFS spectra

We now briefly discuss how we will derive the key measures of chemical composition essential to our science objectives from our PFS spectra.

A number of techniques estimating the stellar metallicity  $[\text{Fe}/\text{H}]$  and other atmospheric parameters (effective temperature  $T_{\text{eff}}$  and surface gravity  $\log g$ ) are available to exploit our PFS spectra, in combination with photometric data provided by, e.g., SDSS and HSC. Well established techniques include, e.g., fitting observed spectra with grids of synthetic ones for obtaining the most likely set of ( $[\text{Fe}/\text{H}]$ ,  $T_{\text{eff}}$ ,  $\log g$ ) (e.g., Wilhelm et al. 1999; Allende Prieto et al. 2008; Kirby et al. 2008, 2009, 2010; Re Fiorentin et al. 2007; Kordopatis et al. 2011), using the Ca II K line, auto-correlation analysis of the stellar spectrum, and Ca II triplet lines for obtaining  $[\text{Fe}/\text{H}]$  (Beers et al. 1999; Norris et al. 2008; Starkenburg et al. 2010), and using gravity-sensitive Ca I line and Mg features for obtaining  $\log g$  (Morrison et al. 2003). Each of these methods is usually optimal over restricted ranges of color ( $g - r$ ), metallicity  $[\text{Fe}/\text{H}]$ , and signal-to-noise ratio  $S/N$ . A great advantage of PFS in this respect is that PFS stellar spectra are designed to cover a broad wavelength range from the blue ( $\sim 3900 \text{ \AA}$ ) to red ( $\sim 9,000 \text{ \AA}$ ) continuously, so that it will be possible to apply various calibration methods and arrive at a robust set of stellar parameters ( $[\text{Fe}/\text{H}]$ ,  $T_{\text{eff}}$ ,  $\log g$ ).

Using such multiple techniques for the estimation of stel-

<sup>21</sup> The DDO51 filter is an intermediate filter in the Washington photometric system, where the strong surface gravity sensitivity of the Mg I triplet and MgH band features near  $5150 \text{ \AA}$  allows discrimination between dwarfs and giants of F-K spectral type.

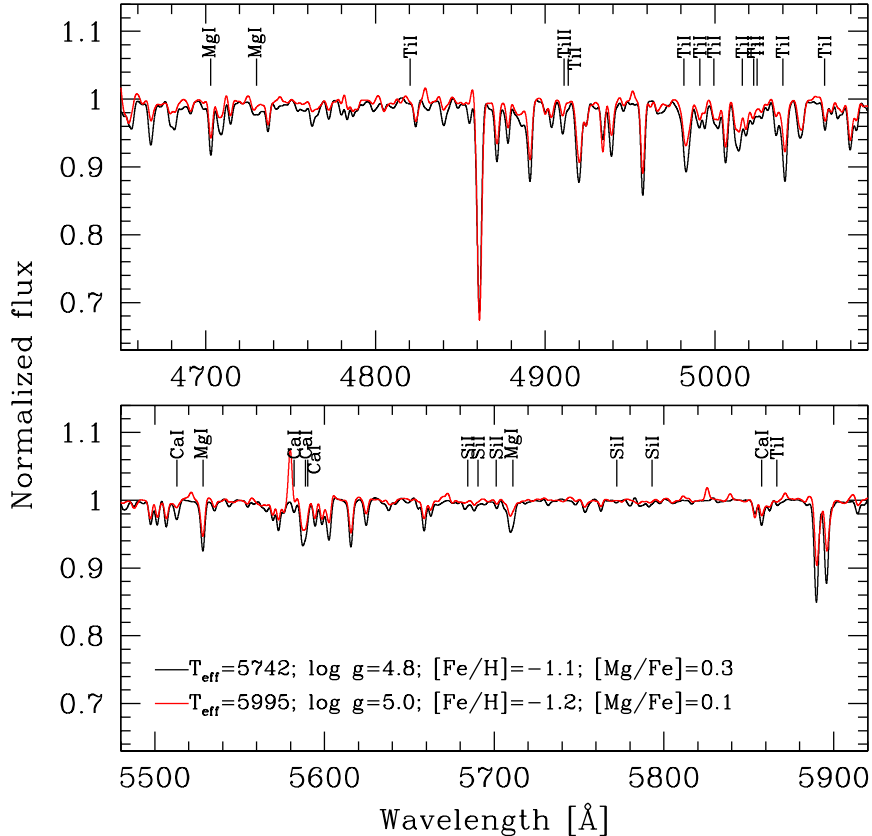


FIG. 14.— Spectra of metal-poor dwarf stars in the Milky Way with  $R = 2,000$ , which are obtained by degrading Subaru/HDS spectra with  $R = 50,000$  taken from Ishigaki et al. (2012). This spectral region contains dominant  $\alpha$ -element spectral features in the wavelength window, which can be used to determine  $[\alpha/\text{Fe}]$  with  $\Delta[\alpha/\text{Fe}]$  as small as 0.1 dex for  $S/N \sim 30$  spectra (Lee et al. 2011). The black and red lines show dwarf stars, BD+13 2995 and G 18–24 with  $[\text{Mg}/\text{Fe}] = 0.3$  and 0.1, respectively.

lar parameters, the SEGUE Stellar-Parameter Pipeline (SSPP) has been developed and utilized in the SDSS/SEGUE survey (Lee et al. 2008; Allende Prieto et al. 2008). Recent work (e.g., Li et al. 2010) has successfully demonstrated that the SSPP can provide reasonable estimation of stellar atmospheric parameters, even for non-SEGUE data with similar spectral resolutions (as low as  $R = 1,000 \sim 2,000$ ), provided the wavelength coverage extends from 3800 Å (to include Ca II HK) to 5200 Å (to include Mg features at 5150 Å which are sensitive to surface gravity). Adopting the SSPP (and implements its subsequent improvements up to the time of our PFS survey) as the calibration pipeline of PFS spectra will enable us to obtain, for our sample of a million stars, metallicities  $[\text{Fe}/\text{H}]$  to a precision of 0.2 dex. Furthermore, with this pipeline, the  $[\alpha/\text{Fe}]$  ratio commonly used to distinguish enrichment by Type II or Ia SNe, will be secured to a precision of  $\sim 0.1$  to 0.2 dex for spectra with a  $S/N = 30$  (Lee et al. 2011). Fig. 14 shows spectra of metal-poor dwarf stars in the Milky Way with  $R = 2,000$ , where the spectral region contains dominant  $\alpha$ -element spectral features, which can be used for the calibration of the  $[\alpha/\text{Fe}]$  ratio, as demonstrated by Lee et al. (2011).

Flux calibrated spectra will provide independent measurements of stellar atmospheric parameters, and can be advantageous for the abundance measurements. Regular observations of flux standards should be sufficient to define the relative cal-

ibration to better than 5%. Absolute flux calibration is not necessary since the absolute fluxes can be deriving by adjusting the relative fluxes to match the extant photometry data.

### 3.4. Technical Requirements

We now summarize the technical requirements essential for the GA PFS survey to meet its scientific objectives.

As discussed above, we require spectra with  $S/N > 30$  per resolution element for a broad range of wavelengths, including the Ca II lines (3933 Å), in order to determine metallicities better than  $\sim 0.2$  dex and radial velocities better than  $\sim 10 \text{ km s}^{-1}$ . The latter velocity accuracy is essential to distinguish stellar components in velocity or phase space and corresponds to a precision better than the velocity dispersion of the Galactic disk or typical dSphs. The wavelength region around 5150 Å is also important as it includes Mg Ib and MgH features which provide good sensitivity to surface gravity.

We need to observe many target stars per PFS field in order to assemble a statistically meaningful sample. Based on a standard star-count model by Robin et al. (2003), there are  $\sim 2,300$  stars of  $V = 17$  mag at Galactic latitude  $b = 30$  deg per PFS field and a comparable number of stars is expected at fainter magnitudes (Fig. 15). We have further examined the SDSS DR8 to estimate the observed number of stars per PFS FoV at various Galactic longitudes and latitudes within SDSS footprints. Fig. 16 illustrates the number of stars with a given (extinction corrected)  $g$  magnitude range at  $l = 180^\circ$  as

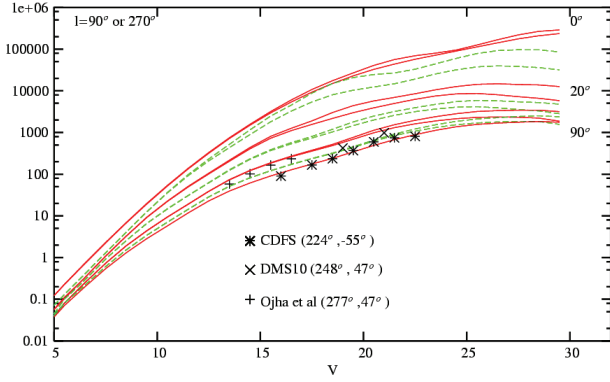


FIG. 15.— Star count predictions (per magnitude and per  $\text{deg}^2$ ) from the Besançon model of the Milky Way (Robin et al. 2003) in the  $V$  band at  $l = 90^\circ$  or  $270^\circ$ , for latitudes  $10^\circ$  to  $90^\circ$  from top to bottom ( $0^\circ$ ,  $20^\circ$ ,  $45^\circ$  and  $90^\circ$  with solid lines,  $10^\circ$ ,  $30^\circ$  and  $60^\circ$  with dashed lines). For each latitude the bifurcation is due to the warp, the highest part being for  $l = 90^\circ$ ,  $b > 0$  or  $l = 270^\circ$ ,  $b < 0$ .

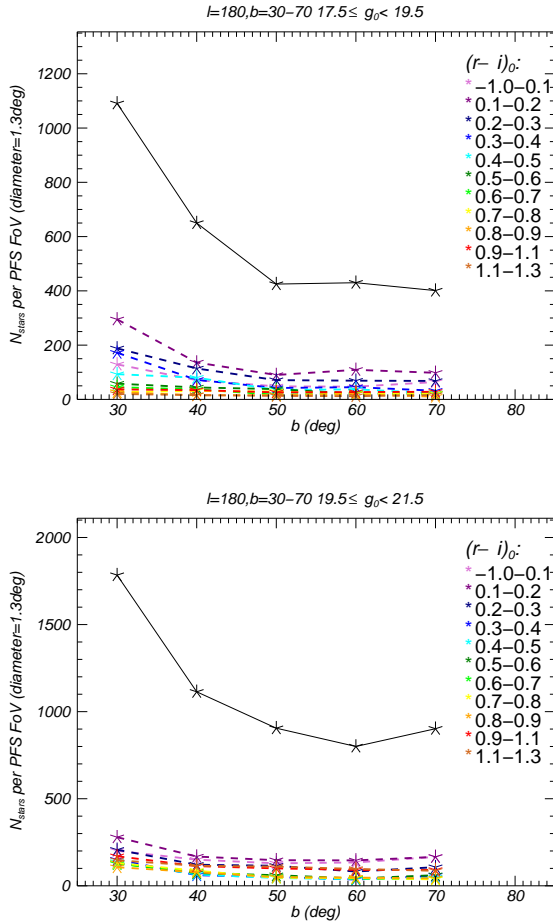


FIG. 16.— Number of stars from the SDSS DR8 with a given  $g_0$  magnitude range per PFS field of view at  $l = 180^\circ$  is plotted against Galactic longitudes. Left and right panels are for the magnitude ranges of  $17.5 < g_0 < 19.5$  and  $19.5 < g_0 < 21.5$ , respectively.

a function of Galactic latitudes,  $b$ . The total number of stars per PFS FoV with  $g < 21.5$  is as high as 3000 at  $b = 30^\circ$  and 1500 at  $b = 60^\circ$ . We will set no color cuts in selecting targets but will utilize all stars for different science aspects. Thus, a multiplex gain of 2000-3000 will be sufficient for the pro-

posed Galactic studies. Also with this setup, it is possible to target a sufficient number of stars in the direction of the M31 halo (red giants in M31 and foreground/background contamination) as already mentioned in the previous subsection.

#### 4. GALAXY EVOLUTION

*Summary: The goal of the PFS Galaxy Evolution Survey is to follow the growth of the full panoply of the galaxy population from cosmic dawn to the present. While many of the basic physical processes that drive galaxy evolution (dark matter halo merging, gas accretion, star formation and associated energy release, galaxy merging, black hole accretion and associated energy release) are known, how and when they operate remain unknown. We will use the unprecedented wavelength coverage of PFS, in particular its  $1 - 1.3\mu\text{m}$  near-infrared coverage, to explore the redshift range  $1.4 < z < 2.2$  when the star formation rate density and black hole growth were at their peak. Using  $\text{Ly } \alpha$  emission, we will trace the growth of galaxies and black holes all the way to the epoch of reionization,  $2 < z < 7$ . With the deep broad- and narrow-band imaging from the HSC survey, we will study these young galaxies with unprecedented statistics using PFS. We propose a 100 night survey covering  $16 \text{ deg}^2$  with 3 main components: (i) a color-selected survey of half a million galaxies with  $1 < z < 2$  to  $J_{\text{AB}} = 23.4 \text{ mag}$ , with a  $z < 1$  component limited to  $J_{\text{AB}} = 21$ , (ii) a survey of 30,000 bright dropout galaxies and  $\text{Ly } \alpha$  emitters over  $2 < z < 7$  and (iii) a survey of color-selected quasars from  $3 < z < 7$ .*

##### 4.1. Galaxy Evolution Objectives

SDSS has provided a detailed understanding of the optical properties and large-scale distribution of present-day galaxies. Fainter surveys such as zCOSMOS (Lilly et al. 2009), DEEP2 (Cooper et al. 2006), and VVDS (Le Fèvre et al. 2005) have studied areas of  $\leq 2$  square degrees at  $z \sim 1$ ; at this epoch galaxies had similar morphologies, luminosity ranges, and environmental characteristics as they do today. However, the rates per unit comoving volume of star formation and black hole growth were at their highest at somewhat higher redshifts  $1 < z < 2$  (Fig. 17). We seek to understand how galaxies, gas, and dark matter halos are distributed at these epochs, how each of these components interact (via merging, cooling flows, star formation, energy feedback, and reionization), and whether star formation was fundamentally different from what we deduce today. To date there are spectroscopic samples of only a few thousand blue, star-forming galaxies with  $z > 1.4$ , covering  $< 1 \text{ deg}^2$  (e.g., Steidel et al. 2010). Particularly difficult to study is the so-called redshift desert  $1.4 < z < 2.2$ , since no strong and reliable redshift indicators fall in the optical bandpass. The PFS spectrograph, with a wavelength coverage of  $0.38\text{-}1.3 \mu\text{m}$ , is specifically designed to explore the redshift desert over volumes comparable to the SDSS at low redshift.

PFS can also study galaxies from  $z \sim 2$  to the redshift frontier of  $z \sim 7$  (Fig. 17). Here we will utilize HSC to target Lyman break galaxies (LBGs) and  $\text{Ly } \alpha$  emitters (LAEs), obtaining unprecedented numbers of spectra of both populations. PFS will thereby probe the epoch when the star formation of early galaxies changed the ionization state of the intergalactic medium (IGM). Its panoramic capability will enable studies of the topology of ionized bubbles as well as the clustering properties of young galaxies at  $2 \lesssim z \lesssim 7$ .

It is now recognized that all massive galaxies contain supermassive black holes (SMBHs) in their centers, with masses

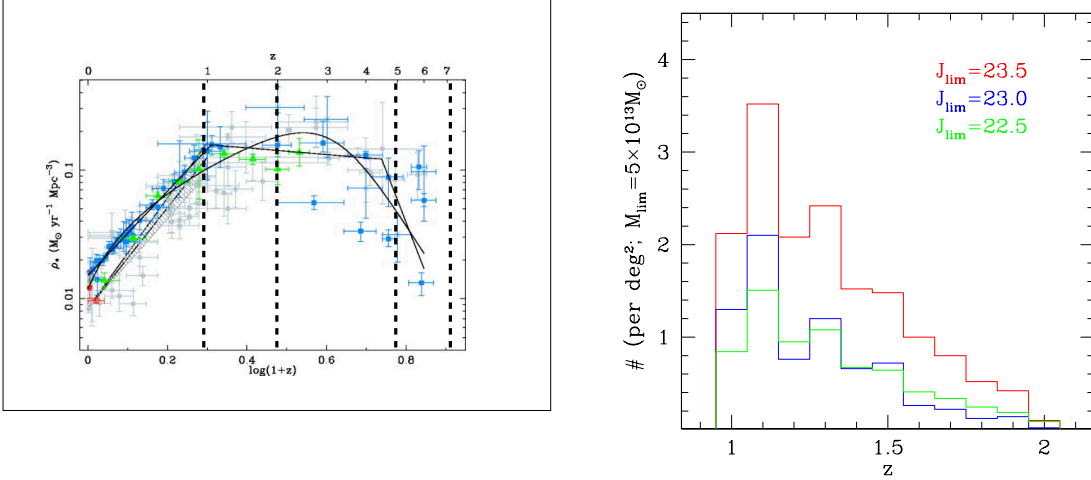


FIG. 17.— *Left*: Star formation rate per comoving volume as a function of redshift (Hopkins & Beacom 2006). Different symbols show measurements made at different wavelengths. The solid lines show parametric fits to the data (refer to Hopkins & Beacom for details). The PFS redshift ranges are shown as black dashed vertical lines. *Right*: Expected number of clusters with  $M > 5 \times 10^{13} M_{\odot}$  per  $\text{deg}^2$  survey volume with the stated depths. The estimates use the “lightcone” simulations of Sehgal et al. (2010), and populate halos with galaxies using the halo occupation distribution model from Tinker & Wetzel (2010).

ranging from  $10^5 - 10^{10} M_{\odot}$ . The evolution of black hole growth with cosmic time resembles that of the star-formation activity. The steep drop-off of both at  $z < 2$  points to a link between supermassive black hole growth and galaxy formation. Moreover, the masses of SMBHs are correlated with those of their host bulges in the present-day Universe, suggesting that they evolved together (e.g., Kormendy & Richstone 1995; Magorrian et al. 1998; Marconi & Hunt 2003). A full understanding of galaxy evolution requires study of the accretion history of SMBHs. PFS will target color-selected quasars  $\sim$  three magnitudes fainter than the SDSS to a redshift of  $z = 7$  and will study their clustering properties, the evolution of BH mass density with cosmic time, and the evolution in the metal content and ionization state of the inter-galactic medium.

The wide wavelength coverage and large area of the PFS will enable an enormously powerful galaxy redshift survey. We envision a survey of  $16 \text{ deg}^2$  over  $\sim 100$  nights. At  $1 < z < 2$ , we will survey to  $J_{\text{AB}} \approx 23.4$  mag with 3 hour exposures, yielding a fair sample with stellar masses above  $\sim 10^{10} M_{\odot}$  at  $z \approx 2$ . To cover comparable objects at lower redshifts, we will also survey  $z < 1$  targets down to  $J = 21$  mag with 2 hour integrations. We will measure redshifts for  $\sim$  half a million galaxies allowing us to determine luminosity/mass functions that are not cosmic-variance limited. At  $2 \lesssim z \lesssim 7$  we will target bright, star-forming galaxies. We expect to observe 15,000 LBGs and LAEs, more than an order of magnitude more than existing spectroscopic samples. We will focus on three imaging surveys for target selection, based on the Hyper-Suprime Cam (HSC) imaging survey. The survey will have three components; we focus on the HSC Deep layer, which will reach a  $5 \sigma$  depth of  $i < 27.2$  mag. We will target  $16 \text{ deg}^2$  of the HSC Deep survey that contains existing deep NIR imaging down to  $J_{\text{AB}} = 23.4$  mag. HSC Ultra-deep covers  $3.5 \text{ deg}^2$  and we will perform deeper spectroscopy in this area. Finally, HSC Wide covers  $1400 \text{ deg}^2$ , over which we will search for rare high-redshift quasars ( $z > 3$ ).

The scientific objectives of the PFS Galaxy Evolution Survey are as follows:

1. *The Build-up of Stellar Mass Density*: We will derive stellar masses and star formation rates from the spectra (Fig. 19). It has been shown that stellar population modeling works well even at our low resolution (e.g., Kriek et al. 2006, 2011; Panter et al. 2007; Chen et al. 2012). We will measure star formation rates both from the modeling and from [O II] emission out to  $z \sim 2.5$ , which we will calibrate using  $\text{H}\alpha$  emission at low redshift. At yet higher redshift, we can use the UV continuum as a star formation rate indicator (Fig. 19). We will trace the stellar mass function and star formation history of galaxies as a function of color and galaxy density at  $1 < z < 2$ .
2. *The Growth of Structure*: We will measure the spatial correlation functions of galaxies on both small and large scales (i.e., one and two halo terms; Fig. 18 right). Spectroscopic redshifts give significantly better clustering measurements than do photometric redshifts. On large scales, we will measure the galaxy bias as a function of galaxy properties and redshift, which is a key constraint on galaxy formation models. On smaller scales, we can study the properties of galaxies in cluster and group environments, and see how galaxy formation is related to environment and dark matter halo mass. We will tie the evolution in stellar mass to that of the underlying dark halos from  $1 < z < 7$ . We will also study the cluster/proto-cluster population as a function of redshift. Over the survey volume, we expect to find  $\sim 325$  clusters with mass  $M > 5 \times 10^{13} M_{\odot}$  (and  $\sim 65$  massive clusters with  $M > 10^{14} M_{\odot}$ ) at  $1 < z < 2$  (Fig. 17), an unprecedented sample when compared to the very few found in current deep pencil-beam surveys. At  $2 \lesssim z \lesssim 6$  we expect to find  $\sim 100$  proto-clusters using LBGs and LAEs as tracers.
3. *Gas Inflow and Outflow*: We will trace the interplay between gas accretion and feedback using both direct and indirect means. We will trace the mass-metallicity relation using strong emission-line diagnostics for  $z < 1.6$

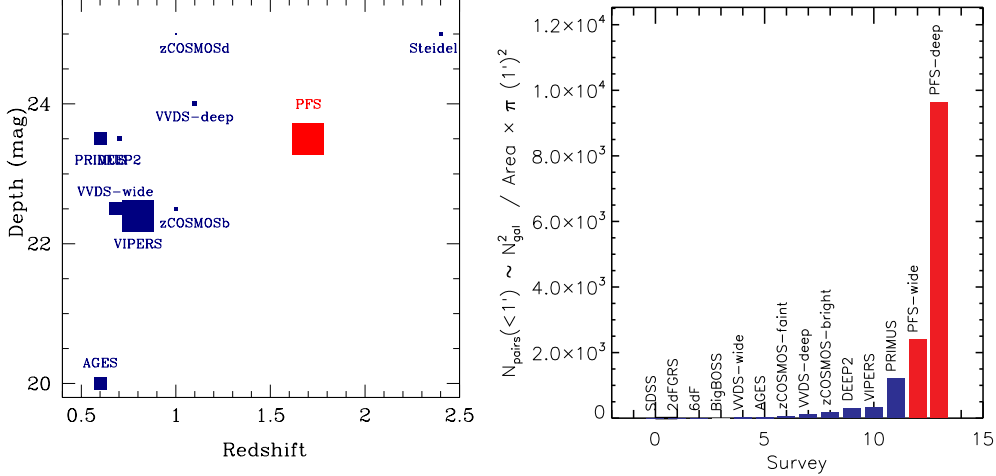


FIG. 18.— *Left*: Depth versus redshift for existing and planned large redshift surveys. The symbol size represents survey area. Each survey is placed roughly at the median redshift of the survey. PFS occupies a unique position in this parameter space, as it is the *only* large survey capable of filling in the redshift regime between  $1.5 < z < 2$ . *Right*: This figure shows the number of spectroscopic pairs separated by less than one arcminute. It highlights the power of PFS to (i) study small-scale clustering on the group scale and (ii) probe the gas distribution in galaxy halos using absorption line probes. Fiber-based spectroscopic surveys doing only one pass over the sky suffer from the fiber collision limitation and cannot access small-scale pairs. We note that we have not counted overlap regions for the BigBOSS survey.

and with stellar photospheric lines in the UV at  $z > 2$  by stacking spectra (Ando et al. 2007). We will search for outflow or inflow using interstellar absorption lines such as Mg II, S IV, C IV, etc in stacked spectra. We will also stack background galaxy and quasar spectra as a function of impact parameter around foreground galaxies to map out the gas kinematics in the outer halos of star forming galaxies (e.g., Steidel et al. 2010; Tumlinson et al. 2011; Bordoloi et al. 2011). Using the galaxies themselves as a backlight, we will search for the signature of cold-gas inflow and test the cold accretion hypothesis with a sample  $\sim 20$  times larger than that of Steidel et al.

4. *The Build-up of Supermassive Black Holes*: We will measure the quasar luminosity function from  $3 < z < 7$  to  $\sim 3$  mag deeper than the SDSS. A wide-area search of  $\gtrsim 1000 \text{ deg}^2$  is needed to find rare luminous  $z > 6$  quasars, while we will study fainter populations over the  $16 \text{ deg}^2$  galaxy survey. Using quasar emission lines, we will study the evolution of the BH mass function, and the accretion history of these black holes. We will be able to study the clustering properties of the quasar population using cross-correlation with the dropout galaxies in our sample, which will reveal the typical dark halo mass of the quasar population as a function of redshift and luminosity (e.g., Adelberger & Steidel 2005), and relate the relative growth of galaxies and BHs. Finally, we will uncover obscured and low-luminosity active galaxies using emission-line diagnostics in the  $1 < z < 2$  survey.
5. *The Epoch of Reionization, Ionized bubbles*: For the first time, we will constrain the topology of ionized bubbles at  $z \sim 7$  with a complete spectroscopic sample of LAEs. Current surveys (e.g., Ouchi et al. 2010) have shown the promise of using the mean Ly  $\alpha$  profile shape as a tracer of neutrality, but the small samples of-

fer no information on large-scale spatial variations. An ambitious but practical opportunity will be to exploit the  $\sim 9,000$  LAEs from our PFS survey to investigate the possibility of detecting evolution in Ly  $\alpha$  profiles over scales of 10 Mpc, comparable to the expected size of typical ionized bubbles. We will calibrate the intrinsic Ly  $\alpha$  lineshape using a critical sample of LAEs at  $z \sim 2.3$ , for which we will have robust systemic redshifts from [O II].

6. *The Epoch of Reionization, Neutral Fraction*: We will utilize the evolution of the Ly  $\alpha$  luminosity function (e.g., Ouchi et al. 2010) and the complementary measure of the fraction of galaxies with Ly  $\alpha$  emission with unprecedented large samples of LAEs and LBGs, respectively (e.g., Stark et al. 2011). This dual approach will allow us calibrate possible intrinsic evolution in the Ly  $\alpha$  luminosity function arising from changes in the comoving star formation density and linking emission line demographics to LBG colors will address possible effects of dust extinction. The resulting decline in the visibility of Ly  $\alpha$  over  $6 < z < 7$  will then be interpreted in terms of a change in the neutral fraction using appropriate models (e.g., McQuinn et al. 2007). We will obtain complementary constraints on the neutral fraction using the Gunn-Peterson troughs of  $z \sim 6 - 7$  quasars.

The wide wavelength coverage of PFS is an unique asset. The NIR arm allows us to measure the [O II] line (and thereby reliable redshifts) out to  $z = 2.5$  (Fig. 19). It allows us to trace galaxy populations via their diagnostic spectral features from low to high redshifts with no gaps. As illustrated in Fig. 19, we will have access to many important emission and absorption features over an unprecedented range of redshifts, which will enable new and important science. We will cross-calibrate star-formation and metallicity indicators such as [O II] and H $\alpha$ ; both can be observed to  $z \approx 1$ .

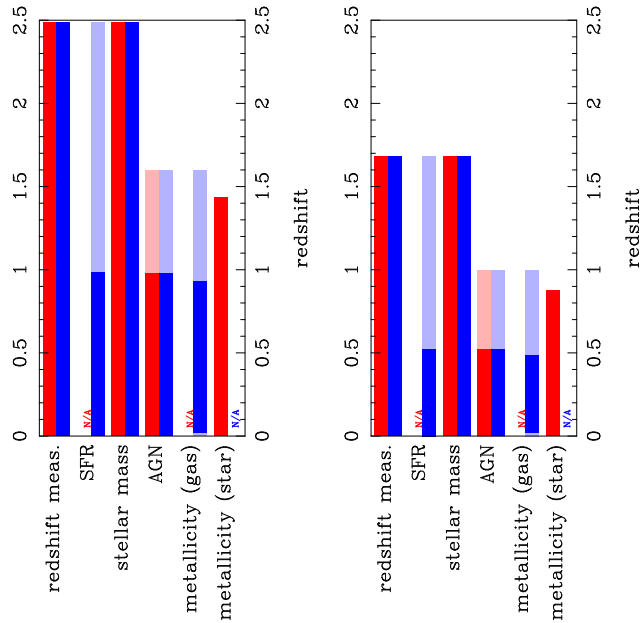


FIG. 19.— Redshift range over which various spectroscopic properties of galaxies can be tracked assuming a flux-limited survey down to  $i = 23.5$ . *Left*: The capabilities of PFS with the full wavelength coverage (optical+NIR). *Right*: The same, but with only the optical band. The dark and light areas show the redshift range where a primary and secondary set of spectral features will be available for galaxies with masses above a characteristic value ( $M_*$ ). Passive and star forming galaxies are marked in red and blue, respectively.

#### 4.2. Simulated Data

We have generated realistic simulated spectra to determine what types of measurements are feasible as a function of continuum and line luminosity. Our model for the throughput of the spectrograph includes the detector quantum efficiency, light-losses at the fiber due to seeing, losses in the fiber and fiber coupling, reflectivity of the Subaru primary mirror and transmission of the corrector, throughput of the camera and collimator (including vignetting) and dichroics as a function of wavelength, the grating transmission, and the atmospheric transparency. It is encouraging that our treatment is similar to (but independent of) that described in §2.2.1, and that we derive similar results.

The most important, and most challenging, aspect of our simulations involves modeling the sky subtraction. Sky emission lines are a major source of noise in the red and NIR arms. Again, our treatment is similar to that outlined in §2. We assume first that we can measure the overall sky level at a given time at the 0.5% level. This requirement is theoretically possible but technically challenging in practice. Then, for each sub-exposure of 20 min, a random-deviate wavelength error of 0.01 pixel and a 0.5% amplitude error in the subtracted sky, again easily supported by the Poisson noise in the lines themselves, is added and propagated forward into the final combined spectrum. Finally, we add 1 percent of the total flux on the detector as a smooth scattered background.

The spectra are combined with inverse-variance weighting to downweight pixels that are contaminated by the sky (no clipping is performed), and then resampled at  $R = 400, 300, 300$  for the blue, red, and NIR arms respectively (Figs. 20 and 21) for study of the continuum S/N. When we examine emission lines, we instead use a spectral resolution  $R \sim 1200$  to properly resolve emission lines with

$\sigma \approx 100 \text{ km s}^{-1}$ .  $R \approx 300$  is not ideal for measuring spectral absorption features either. However, because such a large fraction of the spectrum is eaten by night sky lines, it is convenient to examine spectra at this resolution as representative of the information content in the spectra.

In this subsection we will show that our main science goals are achievable. We assume exposure times of 0.3-3 hrs for the continuum-selected survey, spending three hours on the sources in the faintest half-magnitude bin ( $J_{AB} = 23 - 23.4$  mag). Further, we plan to reposition fibers rapidly, thereby allowing us to leave bright targets after as short as a single 20 min integration. We assume six-hour integration times for fainter LBGs and LAEs.

We have two primary sources for the spectral energy distributions that we use. For the continuum-selected survey, we use model fits to NEWFIRM Medium-Band Survey photometry for galaxies spanning the color-magnitude diagram. These fits, from the code EAZY (Brammer et al. 2008) include emission lines. In Fig. 20, we show a representative red and blue galaxy at our detection limit of  $J_{AB} = 23.4$  mag at  $z \approx 2$ , observed in a 3hr integration with PFS. The figure shows that the 4000 Å break is detected with enough significance to allow redshift detection at the magnitude limit even without the presence of emission lines.

To generate a representative LBG, we have started with the spectral energy distribution from Reddy et al. (2012). We add lines to match the observed EWs from Shapley et al. (2003); the objects shown in Fig. 21 in the bottom panel are representative of objects with high Ly  $\alpha$  EW in their sample. From these simulations it is clear that we will be able to detect both the Ly  $\alpha$  and interstellar absorption features in the continuum down to our detection limits. Finally the QSO spectra are generated from the composite spectrum from Vanden Berk et al. (2001).

We also generate a picket-fence of emission lines across the entire waveband. We generate [O II] models as a pair of Gaussians at  $\lambda, \lambda$  3726.2, 3728.9, with a ratio of 2 : 1. The pair of lines are assumed to have the same intrinsic width of  $\sigma_{\text{gas}} = 100$  and 200  $\text{km s}^{-1}$  for two different simulation. Ly  $\alpha$  is modeled with a red-asymmetric profile.

##### 4.2.1. Redshifts

Our greatest challenge comes in measuring absorption-line redshifts for  $z \approx 2$  galaxies at our flux limit. In practice, we expect that many of our targets will have some [O II] emission, since most red galaxies have low EW emission lines (e.g., Ho et al. 1997; Yan et al. 2006). Nevertheless, there will certainly be passive red galaxies for which the 4000Å break will be the primary source of redshift information. It will be measured in the NIR arm. The spectral simulations are very promising. It has been shown that reliable redshift measurements are possible if one achieves a signal-to-noise ratio of 10 per pixel in the continuum around the 4000 Å break (Tonry & Davis 1979). Thus, we expect that if we can characterize and subtract the sky as assumed here, we will be able to measure redshifts confidently at our continuum limit of  $J_{AB} = 23.4$  mag. Furthermore, as shown by Chen et al. (2012), it is possible to derive reliable stellar masses with 0.2 dex accuracy in spectra with S/N per pixel as low as 3, provided the 4000 Å break and H $\delta$  features are covered in the bandpass.

##### 4.2.2. Fluxes and Line-widths

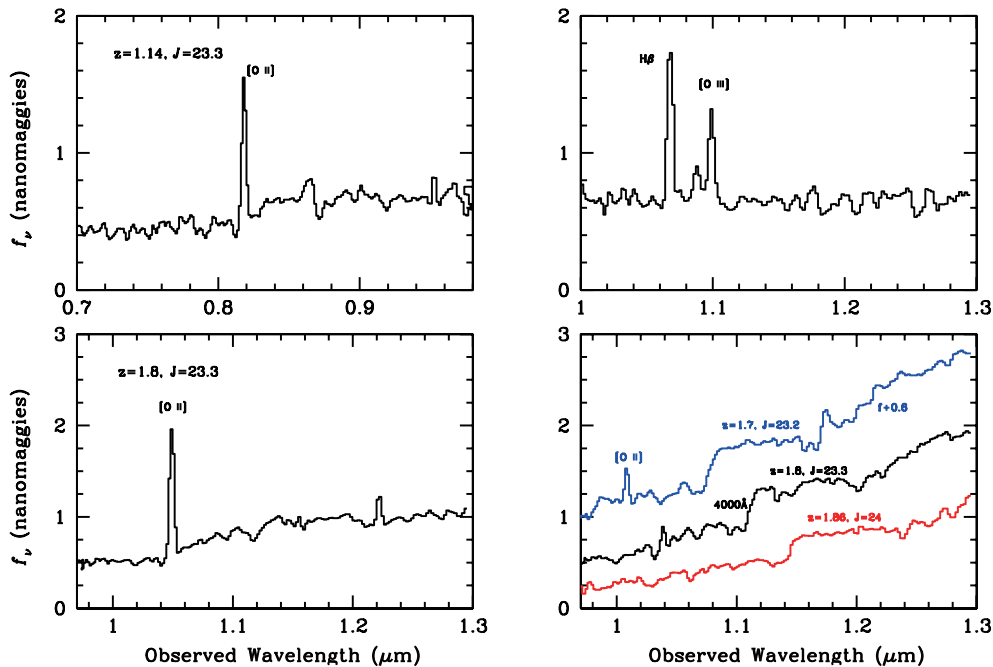


FIG. 20.— Simulated spectra (see text) demonstrating the power of PFS. The spectra are plotted in units of “nanomaggies”, a unit of flux used by the SDSS, defined such that one maggie is the flux from an  $AB=0$  object, 3631 Janskys. Thus 1 nanomaggie is equivalent to an apparent  $AB$  magnitude of 22.5, or  $3631 \times 10^{-9}$  Jy or  $3.631 \times 10^{-29}$  erg s $^{-1}$  cm $^{-2}$  Hz $^{-1}$ . The spectra have been binned to a resolution of  $R = 400, 300, 300$  in the blue, red, and NIR arms respectively. *Top Panel:* This is a typical star-forming galaxy at  $z = 1.14$  close to our detection limit, showing that we will have significant detections of [O II], H $\beta$ , and [O III], which we can use to measure gas-phase metallicity (Fig. 19). We show a three hour integration. These spectra are based on stellar population synthesis models of galaxies in the NEWFIRM Medium Band Survey. *Bottom:* A star-forming (*left*) and three passive (*right*) galaxies at  $z = 1.8$  and magnitudes as indicated as seen in a three-hour integration with PFS. The spectra were also generated as model fits to the NEWFIRM Medium Band photometric data, which provides some constraint on emission-line EW. We show that at our magnitude limit we will have a significant detection of either [O II] or the 4000 Å break for measuring redshifts.

Many of our science cases depend on our ability to measure not only the line centroid (the redshift) but also the line widths and fluxes. For [O II] lines with a combined flux of  $F = 10^{-17}$  erg s $^{-1}$  cm $^{-2}$ , we find that we can recover the total flux within  $< 20\%$ , and the line-width to within  $< 40\%$ , for all lines with S/N greater than 10 (over most of the band). We recall that this flux is typical of [O II] emitters at  $z \approx 2$  (Takahashi et al. 2007). We repeat the experiment for Ly  $\alpha$  emission lines with  $F = 0.8 \times 10^{-17}$  erg s $^{-1}$  cm $^{-2}$ , which is typical of LAEs at  $5 < z < 7$ . Since we will be measuring Ly  $\alpha$  in the blue and red arms, we can do a bit better, recovering fluxes and linewidths at the 10% level in the blue arm. In the red arm we can only recover linewidths at the 20% level (since the model is skewed, we fit a skewed Gaussian here). However, these limits are for individual objects, while our primary goal is to stack at least 500 spectra in a given patch. Thus, we will do a factor of  $\sim 20$  better at measuring the composite Ly  $\alpha$  profile of high redshift emitters. Finally, we attempt linewidth measurements for our QSO spectra. Even in half-hour exposures at our magnitude limit, we expect to measure the CIV linewidth with 10% precision. Our goal of measuring spectral shapes and estimating SMBH masses from these spectra will not be compromised by the S/N of the spectra. Obviously, there are well-known uncertainties in calculating reliable SMBH masses using broad UV lines, but we will be in a good position to perform internal cross-checks on various broad emission lines using simultaneous observations (e.g., Shen et al. 2008).

#### 4.3. Survey Design and Target Selection

##### 4.3.1. The Survey Fields

Over the coming years, HSC will perform an ambitious imaging survey in *grizy*. The survey will have three components with different depths. That of most interest to us is the HSC Deep layer, which will reach a  $5\sigma$  depth of  $i < 27.2$  mag. There is also narrow-band imaging planned that will be of crucial importance in selecting Ly  $\alpha$  emitters at high redshift. Of the more than 20 deg $^2$  covered by HSC Deep, we are most interested in the 16 deg $^2$  that already contain  $J$ -band data to at least  $J = 23.4$  mag from the UKIDSS DXS survey.

These fields (*XMM-LSS*, *ELAIS-N1*, and the *COSMOS* field) have been selected to maximize overlap with multi-wavelength data sets, including X-ray data to study accretion activity and mid-infrared data to probe obscured star formation and accretion. In particular, we are excited about the prospect to use *Spitzer* and *Herschel* data for measuring complementary star formation rates to those derived from emission lines or continuum fitting. For instance, we have good overlap with the Hermes fields (HerMES Collaboration et al. 2012). Likewise, our survey fields will provide natural targets for ALMA and/or CCAT.

##### 4.3.2. Survey Design: The $1 < z < 2$ Survey

The survey designs are different for the continuum-selected galaxy sample at  $1 < z < 2$  and the study of high-redshift LBGs and LAEs at  $2 \lesssim z \lesssim 7$ . For the  $1 < z < 2$  survey, the critical factors are:

1. We want to study the progenitors of local  $\sim L^*$  galaxies. Based on our spectral simulations, we can expect to reach a S/N  $> 10$  per resolution element (for

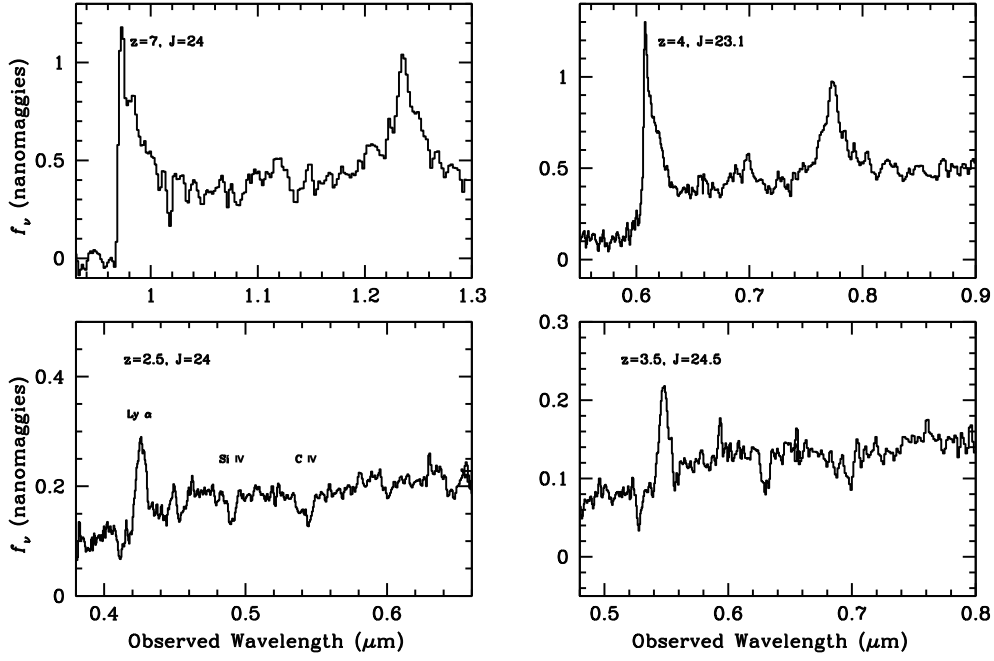


FIG. 21.— *Top Panel:* Similar to the previous figure, but for two QSO spectra assuming 30 minutes for the exposure time. The left-hand panel shows that for even a moderate-luminosity object at  $z = 7$ , a short exposure yields an unambiguous QSO with adequate signal/noise for measuring continuum and spectra line widths. *Bottom:* A star-forming galaxy selected as a  $U$ -band (*left*) and  $g$ -band (*right*) dropout as observed in a six-hour integration with PFS. The spectral energy distribution is based on a spectral synthesis model from Reddy et al. (2012). We expect to detect Ly  $\alpha$  with  $f = 5 \times 10^{-18} \text{ erg s}^{-1} \text{ cm}^{-2}$  at the  $5\sigma$  level in 6 hrs of integration. Note we can detect absorption lines in individual spectra at  $J = 24.5$  AB mag.

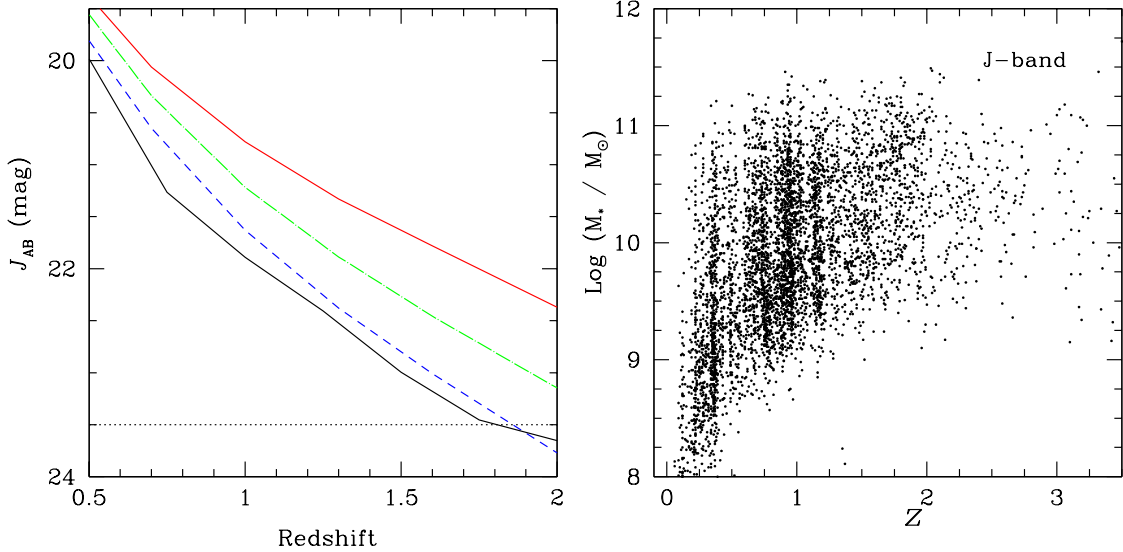


FIG. 22.— *Left:* Illustrative models of evolving galaxies with different evolutionary histories based on Maraston (2005) stellar population models. All models have  $\tau e^{-\tau}$  star formation histories, and are normalized to be  $L^*$  galaxies today. In red is a red galaxy progenitor with a final mass of  $M_* = 6 \times 10^{10} M_\odot$ . In green is a more typical star-forming galaxy with a final mass of  $M_* = 3.4 \times 10^{10} M_\odot$  with an extended history, while the blue line is a more extreme star forming system with a final mass of  $M_* = 2.3 \times 10^{10} M_\odot$ . For reference, in black is the mean apparent  $J$ -band magnitude of a  $3 \times 10^{10} M_\odot$  galaxy at each epoch from the  $K$ -band selected NEWFIRM medium-band survey. *Right:* Expected stellar mass distribution for our  $1 < z < 2$  survey, based on the NEWFIRM Medium Band Survey (Whitaker et al. 2011). We apply a  $J$ -band magnitude limit of 23.4 mag, but note that the total number of points in the figure correspond to a  $0.2 \text{ deg}^2$  survey; we will observe 125 times as many objects. Without a redshift selection, a large fraction of the galaxies in a magnitude-limited sample have  $z < 1$ . The banding in the figure is due to large scale structure; our much larger volume will average over this cosmic variance.

$R \sim 300$ ) in 3 hr exposures at our limiting magnitude of  $J_{\text{AB}} = 23.4$  mag. With this magnitude limit, we expect to probe masses as low as  $10^{10} M_\odot$  at  $z \approx 2$  based on the experience of NEWFIRM Medium-Band

redshift survey (Fig. 22). Note that we are only complete for stellar masses  $\gtrsim 10^{11} M_\odot$ , since below this limit we miss the red, passively evolving galaxies. We have investigated a selection based on *Spitzer*/IRAC de-



TABLE 7  
IMPACT OF COSMIC VARIANCE

Log $M^*$	$1 < z < 1.4$	$1.4 < z < 1.8$	$1.8 < z < 2.2$	$2.2 < z < 2.6$
9.1	0.02	0.02	0.02	0.03
9.6	0.02	0.02	0.03	0.03
10.1	0.02	0.02	0.03	0.03
10.6	0.02	0.03	0.03	0.04
11.1	0.03	0.03	0.04	0.05
11.6	0.04	0.05	0.06	0.07

NOTE. — The logarithmic error bars on the number density in each logarithmic stellar mass bin ( $\log M_\odot$ ) in the 16 deg<sup>2</sup> survey. Error bars are shown for four redshift ranges:  $1 < z < 1.4$ ,  $1.4 < z < 1.8$ ,  $1.8 < z < 2.2$ ,  $2.2 < z < 2.6$ . The error bars are derived using the method of Moster et al. (2010).

tection. However, we do not have deep enough IRAC imaging over all HSC Deep fields. Furthermore, we would have a large tail of galaxies with  $J_{AB} > 23.4$  mag, for which we would be unable to measure a redshift. Finally, selecting in the rest-frame optical ensures that we will observe both red and blue galaxies (Fig. 22). Thus, we have chosen a rest-frame optical (observed  $J$ -band) selection as a compromise between UV-selection on the one hand, and stellar-mass selection via *Spitzer* on the other. Further color selection will be needed to remove low redshift contaminants, as described in detail in point 4 below and §4.5.3.

- In order to observe the same population at low redshift, we also plan to observe all objects to a limiting magnitude of  $J_{AB} = 21$  mag. Since we will spend only 20 min per galaxy at these bright limits, and since we can rapidly reconfigure the fiber placement, we get these 6000 galaxies per deg<sup>2</sup> essentially for free, and they provide a low-redshift comparison sample (e.g., for comparing  $H\alpha$  and [O II]-derived star formation rates).
- The area should be large enough to minimize cosmic variance. In 16 deg<sup>2</sup> we cover a volume that is a few tenths that of the SDSS in a redshift bin at  $z \approx 2$ , which should sample a fair volume of the universe. To quantify the level of cosmic variance, in Table 7 we show the expected error bars on the number density of galaxies in mass and redshift bins derived using the method of Moster et al. (2010). The nominal survey area of 16 deg<sup>2</sup> will avoid limitations of cosmic variance.
- We want a sample selection that is as unbiased as possible with regard to galaxy color, stellar age, line emission, etc. We have considered various selection techniques, including photometric redshift selection, IRAC color, and optical-NIR color selection. None is perfect, but the pros and cons of each are outlined below.

#### 4.3.3. Target Selection: The $1 < z < 2$ Survey

A major strength of the SDSS galaxy survey was the simple magnitude-limited selection with an easy-to-model selection function. We would like to replicate that ideal to the extent possible. Recall that we must integrate for 3 hr per source at our magnitude limit of  $J_{AB} = 23.4$  mag to obtain scientifically useful spectra. There are 12,000 galaxies per deg<sup>2</sup> with  $23 < J < 23.4$ . Even with the multiplexing capabilities of PFS, a purely magnitude-limited survey over 16 deg<sup>2</sup> would take nearly 200 nights. Furthermore,  $> 50\%$  of our targets would be faint galaxies at  $z < 1$ . As we select in redder bands,

TABLE 8  
ALL TARGETS

Mag. (1)	$z$ (2)	Selection (3)	N (4)	Int. Time (5)	Area (6)
$J_{AB} < 21$	$z < 1$	photoz	6k	0.3	16
$J_{AB} = 21 - 22$	$1 < z < 2$	photoz	1.5k	0.3	16
$J_{AB} = 22 - 23$	$1 < z < 2$	photoz	8.4k	2	16
$J_{AB} = 23 - 23.5$	$1 < z < 2$	photoz	12k	3	16
$NB387 = 25$	$z = 2.2$	LAE	400	3	16
$NB816 = 25$	$z = 5.7$	LAE	230	6	16
$NB921 = 25$	$z = 6.6$	LAE	240	6	16
$NB101 = 26$	$z = 7.3$	LAE	14	6	3.5
$i = 22$	$z \sim 2.3$	LBG	5k	3	16
$i = 22$	$z \sim 3.0$	LBG	1.9k	3	16
$i = 22$	$z \sim 3.8$	LBG	500	3	16
$i = 24$	$z \sim 2.3$	LBG	56k	3	3.5
$i = 24$	$z \sim 3.0$	LBG	16k	3	3.5
$i < 25$	$3 < z < 7$	QSO	100	1	16

NOTE. — Col. (1):  $J$ -band magnitude (AB) or narrow-band magnitude. Col. (2): Redshift range. Col. (3): Selection method. Col. (4): Number of galaxies per deg<sup>2</sup>. For the continuum-selected sources, we have adopted the mean of the number densities from the COSMOS and NEW-FIRM catalogs. The LBGs are grouped in redshift with  $\delta z \approx 1$ . Col. (5): Integration time (hrs). Col. (6): Survey area (square degrees).

the fraction of  $z > 1$  targets increases. For instance, only 40% of  $23 < J < 23.4$  objects are low redshift contaminants (see also Table 8). We have chosen a  $J$ -band magnitude limit for this reason and because our spectra cover the  $J$ -band. Over the 16 deg<sup>2</sup> area, deep NIR imaging down to 23.4 mag is already available (in the fields *XMM*-LSS, ELAIS-N1, and the COSMOS field). Even with a  $J$ -band selection we will need to use additional color information to isolate the redshift range of interest. We will perform a purely magnitude-limited survey over two PFS pointings to be observed early in the survey, which will allow us to calibrate our selection methods. A similar strategy was adopted by DEEP2 (Davis et al. 2003).

We have explored various color-selection techniques to maximize the time spent in the redshift range of interest. We outline the strengths and weaknesses of three potential color selections here:

- Photometric redshifts:** As a straw-man, using photometric redshift is a very appealing strategy, as it utilizes all of the exquisite HSC imaging. We are testing the capability of HSC Deep to measure reliable photometric redshifts using simulations based on COSMOS data. In the simulations, the completeness, or the fraction of objects with  $z_{\text{spec}} > 1$  that correctly have  $z_{\text{phot}} > 1$ , is 93%. The contamination, which is the fraction of objects at  $z_{\text{spec}} < 1$  that have  $z_{\text{phot}} > 1$ , is 5%. Furthermore, our ability to measure reliable photometric redshifts should improve dramatically in the coming years, as we gain access to real HSC data, and take advantage of ongoing redshift surveys in our field (e.g., VIPERS). A major concern with using the photometric redshift is systematic error (for instance, in the template set). We will be measuring photometric redshifts for a population without good spectroscopic coverage, and therefore there is room for significant spectral differences between the templates and the targets. Much more work is needed to determine whether photometric redshift selection can provide an unbiased sample selection.
- IRAC CH1-CH2 Selection:** There is a peak in galaxy spectral energy distributions at  $\lambda = 1.6 \mu\text{m}$ , redward of which is the Raleigh-Jeans tail. As this fea-

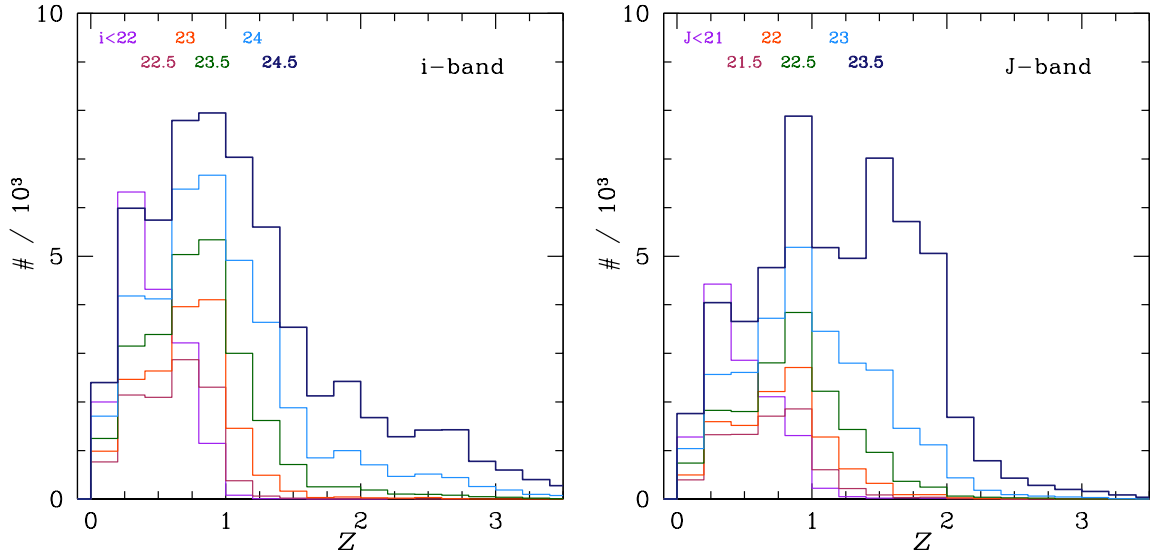


FIG. 23.— *Left*: Differential redshift distributions for an  $i$ -band (AB) selection with the half-magnitude bins indicated at the top. These numbers indicate the lower magnitude of each bin. The number counts come from the 30-band photometric redshifts from COSMOS (Ilbert et al. 2010) over a  $2 \text{ deg}^2$  area; the structures we see are due to cosmic variance. *Right*: Same, but for  $J$ -band (AB) selection.

ture moves through the IRAC bandpasses (particularly CH1 =  $3.6 \mu\text{m}$  and CH2 =  $4.8 \mu\text{m}$ ), the CH1-CH2 color goes through a distinct minimum at  $z \approx 0.8$  and then rises monotonically towards higher redshift (Fig. 24 *left*). Thus, a simple cut of CH1-CH2  $> -0.1$  effectively selects  $z > 1.3$  galaxies (e.g., Papovich 2008). Using the NEWFIRM Medium Band Survey, we find that the completeness, or the fraction of objects with  $z > 1$  that are selected by this method, is 64%, while the contamination, or fraction of selected objects that have  $z < 1$ , is 30%. The numbers are not as impressive as the photometric redshifts, but the selection is easily modeled and relatively free of systematics. The problem is that we would have to obtain sufficiently deep *Spitzer* data ( $\sim 2 \mu\text{Jy}$ ) over the entire  $16 \text{ deg}^2$  field to use this method.

3. ***griJ* Selection:** Inspired by the DEEP2 color selection, we have designed an optical/NIR color selection that is effective at removing  $z < 0.8$  interlopers. Note that  $K$ -band imaging would be better for the purpose of excluding low-redshift sources, but is not available. The color region we select is defined by  $i - J > 1.15$  or  $g - r < (0.5 + 0.359[i - J + 0.8])$  and  $J_{\text{AB}} < 23.4 \text{ mag}$  (Fig. 24 *right*). Again based on the NEWFIRM Medium Band Survey, the completeness (fraction of galaxies with  $z > 1$  that we select) in this case is 93%. The contamination (galaxies in the final sample with  $z < 1$ ) is 42%. However, if we look at galaxies in the final sample with  $z < 0.8$ , the contamination is only 24%. Therefore, this simple color selection, with all bands to be observed as part of HSC or in hand, is very promising. With a redshift limit of  $z > 0.8$ , the total number of objects per  $\text{deg}^2$  would increase by 37% from the straw-man survey presented here. The numbers come from the NEWFIRM catalog but change little when we use the COSMOS photometric redshift catalog instead. In what follows, the numbers assume a perfect cut at  $z = 1$ , but the appropriate correction would only be an increase of 30% for the number den-

sity of continuum-selected galaxies.

We can further mitigate contamination through real-time redshift determinations. The main contaminant in a continuum-limited sample is moderate-redshift, intrinsically faint galaxies that are likely strongly star forming. We should be able to identify their redshifts with a single 20 min exposure, if we can carry out real-time analysis of the spectra. Thus, we can move to another target in  $< 1 \text{ hr}$ , given the fact that the fibers are individually deployable. In addition, we will sharpen our target selection with our magnitude-limited component, as well as with the redshift information from the PFS cosmology survey and the VIPERS spectroscopy, which overlaps with our fields.

If we make a perfect cut at  $z_{\text{phot}} \approx 1$  and  $J_{\text{AB}} < 23.4 \text{ mag}$ , then we expect 22000 galaxies per sq. deg between  $1 < z < 2$ . These numbers, based on small angle surveys, are still subject to cosmic variance at some level. From comparisons between NEWFIRM-AEGIS and NEWFIRM-COSMOS, large-scale structure could change our numbers by as much as a factor of two. In Table 8 we show the number of targets as a function of magnitude, number density, and exposure time, using the average number densities between the NEWFIRM and COSMOS catalogs. *We plan for a total of 68 nights for this component of the survey, assuming 3 hrs per galaxy in the faintest half-magnitude bin.* In Fig. 22, we show that we will be able to observe galaxies with masses  $M > \sim 10^{10} M_{\odot}$  at our redshift limit, allowing us to study the progenitors of  $L^*$  galaxies today. Thanks to the  $J$ -band selection, we will be sensitive to the red sequence even at  $z \approx 2$ , as shown in Fig. 25. The PFS survey is compared in redshift, depth, and area to other existing and upcoming surveys in Fig. 18. Our survey is designed to explore a poorly explored epoch in cosmic history, at the time when star formation was at its peak and galaxies began to resemble those we see today.

Finally, we also propose to perform a purely magnitude-limited survey in 2 PFS pointings. With two independent pointings, we will sample different large-scale structures, and given that we expect  $\sim 10$  clusters with  $M > 10^{14} M_{\odot}$  with

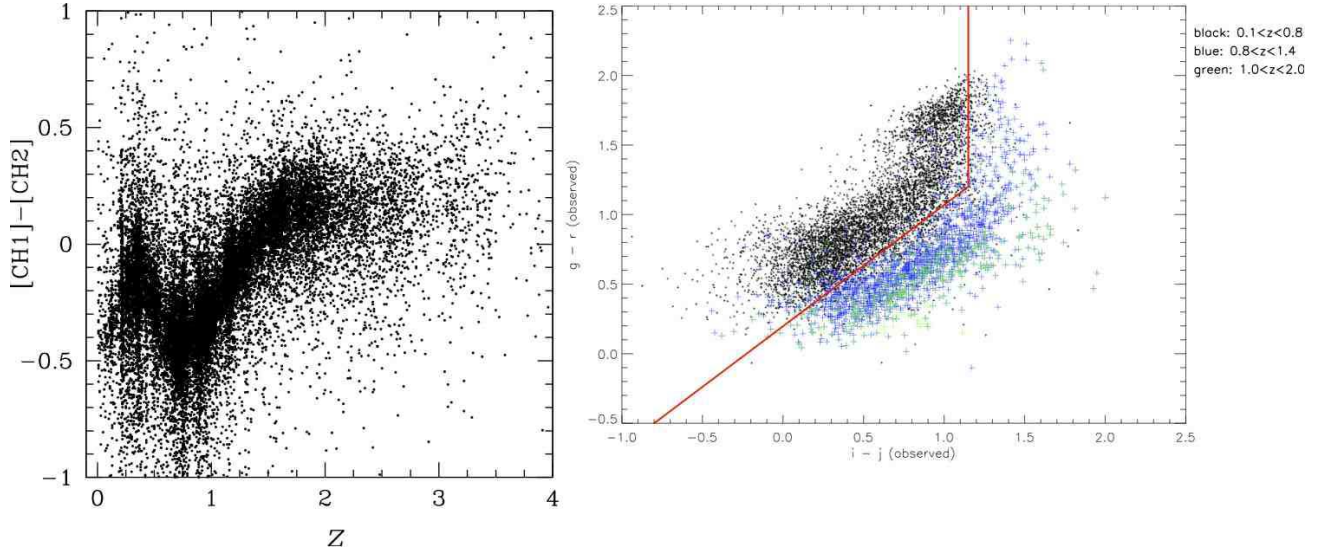


FIG. 24.— *Left*: The dependence of *Spitzer*/IRAC CH1-CH2 ( $3.6 - 4.8\mu\text{m}$ ) on redshift. Galaxies are from the NEWFIRM Medium Band Survey, and IRAC data have  $1\mu\text{Jy}$  depth. The structure is due to the  $1.6\mu\text{m}$  peak in galaxy spectra moving through the CH1 band. *Right*: The  $griJ$  color selection, where galaxies are from the COSMOS survey. We select galaxies with  $i - J > 1.15$  or  $g - r < (0.5 + 0.359[i - J + 0.8])$ ; the selection is highly complete ( $\sim 90\%$ ) while the contamination is only  $\sim 20\%$  for  $z < 0.8$ .

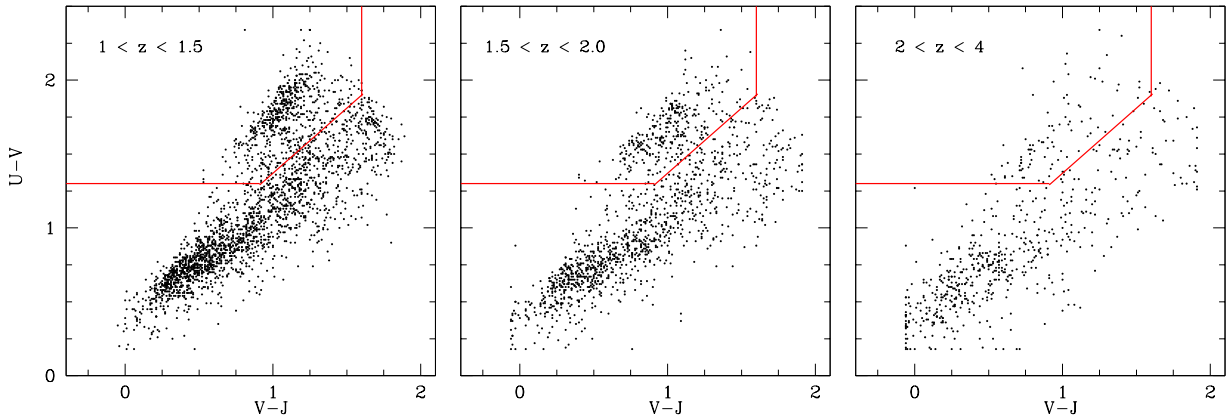


FIG. 25.— Rest-frame color-color plots of the NEWFIRM Medium Band Survey catalog, in the redshift bins indicated and with the  $J$ -band cut of 23.4 mag. In red are the color cuts used to define the red sequence by Williams et al. (2009). It is clear that we will sample the red sequence all the way to  $z \approx 2$ .

$z > 1$ , we do not expect to be cosmic variance limited. Ideally, this component would be completed early in the survey. This small ( $\sim 10$  night) investment, including observations of an additional 24k galaxies per  $\text{deg}^2$  over the nominal color-selected survey, is essential for the following reasons:

1. It will allow us to tune and understand our color selection in detail in preparation for the main survey.
2. Our color cuts will certainly exclude certain rare populations with extreme colors, such as luminous obscured quasars (Zakamska et al. 2003), massive post-starburst galaxies (Tremonti et al. 2007), and other strong line-emitting systems. Within a pure magnitude-limited survey we can assess the missing populations, study their properties, and decide whether to design special color selection to target them.
3. The bias of the galaxies used for the cosmology survey may be a strong function of redshift, as it involves

a color cut which may select astrophysically distinct populations of galaxies at different redshifts. The bias, and the relationship of the selected galaxies to the full galaxy population, needs to be understood in order to use the sample for cosmological inferences, especially when combining clustering measurements at different redshifts. (Note that the BAO scale itself is actually fairly insensitive to these details, as the bias is scale-independent on these very large scales).

#### 4.3.4. Survey Design and Target Selection: Galaxies at the Earliest Epoch

For the  $2 \lesssim z \lesssim 7$  LBGs and LAEs the deciding factors in survey design are:

- We require a wide enough area to study bright and rare Lyman break galaxies. Existing spectroscopic surveys are too narrow to study these populations robustly. Over our  $16\text{ deg}^2$  survey we expect to find 6400  $U$ -band

dropouts brighter than  $i < 24$  mag.

- The area must be large enough to span multiple ionized bubbles in the IGM at  $z \approx 7$ , since the size of ionized bubbles are as large as  $\sim 1$  degree at the end of the reionization epoch.

We will identify LAEs and LBGs at  $2 < z < 7$  down to  $NB \approx 25$  mag and  $i_{AB} = 24$  mag. We expect to spend 3-6 hrs. per target (Table 8) in the same  $\sim 16$  deg<sup>2</sup> field. The LAEs will be selected from the HSC Deep and Ultradeep narrow-band imaging, while the LBGs will be selected as dropouts (Fig. 26). The narrow-band filters in the Ultradeep survey are  $NB387; z = 2.2$ ,  $NB526; z = 3.3$ ,  $NB717; z = 4.9$ ,  $NB816; z = 5.7$ ,  $NB921; z = 6.6$ , and  $NB101; z = 7.3$ . In the Deep survey, we will have imaging in  $NB387$ ,  $NB816$ , and  $NB921$ . We cannot possibly survey all LAE/LBG galaxies over this area and to this depth; there are far too many objects. We will therefore target the following populations:

1. At intermediate redshift ( $2.6 < z < 3.4$ ) we will target the bright end of the LBG luminosity function down to  $I_{AB} = 24$  mag (Fig. 26) over the full 16 deg<sup>2</sup> survey area. We will use a  $U$ -band dropout selection, and the existing depth of  $U = 26$  AB mag in the HSC Deep fields from the CFHT archive allows us to select dropouts down to  $i = 24.5$  mag. We will also select  $riz$ -band dropouts with  $i < 24.4$  mag and  $5 < z < 7$ . Such bright galaxies are relatively rare ( $\sim 430$  per deg<sup>2</sup>) and so their intrinsic properties are not well-studied. These bright systems serve as a good tracer of large-scale structure; we will investigate their clustering properties, and their cross-correlation with quasars. In addition, the intrinsic evolution in Ly  $\alpha$  luminosity from  $2.5 < z < 4$  will serve as an important benchmark for evaluating the impact of reionization on the Ly  $\alpha$  luminosity function at  $z > 5$ . Taking the total number of targets multiplied by the exposure time and dividing by the 1700 science fibers per PFS pointing, we require 12 hours to execute this program. However, note that the targets are spread over the entire survey area and thus will not be observed in a continuous 12 hr sequence. All exposure times quoted in this section have been calculated in this manner, and are only meant to demonstrate the fractional allocation to each survey goal.
2. We will also target LBGs over the same redshift range to a slightly fainter limiting magnitude of  $i_{AB} = 24.5$  mag over the HSC Ultradeep area (3.5 deg<sup>2</sup>). Our primary goal is to use these targets as backlights to study the halo gas of intervening galaxies. We will stack the background systems as a function of impact parameter and study the kinematics of gas in the outer regions of these halos. We will probe galaxy halos at  $z \approx 1.3$  using the continuum selected sample at  $z \approx 2$ , and halos at  $z \approx 2$  using background LBGs at  $z \approx 3$ . The foreground sources will be part of the continuum-selected survey above, and thus will have measured redshifts. The number density of these sources is 18k per deg<sup>2</sup>, exposure times are 3 hr per galaxy, and we observe them over 3.5 deg<sup>2</sup> so we are allocating 19 nights to this program.
3. Finally, we will target all LAEs with  $z = 5.7, 6.6$  to  $NB = 25$  mag over the full 16 deg<sup>2</sup> area. We will

use the evolution in line-shape, luminosity function, and clustering of this population as a probe of reionization. The wide area will allow us to study the patchiness of reionization that is expected to manifest on degree scales (e.g., McQuinn et al. 2007). These galaxies are very faint: we will devote 6 hrs per galaxy. Their number density is 500 per deg<sup>2</sup> for both redshifts combined, so we need 30 hours for this component of the survey. Crucially, we will also study the intrinsic line shapes of LAEs at  $z = 2.2$ , for which we can obtain a systemic redshift from the [O II] line. It is important to quantify the intrinsic variability in Ly  $\alpha$  line shape to distinguish from changes caused by neutral absorption at the epoch of reionization. We will observe these down to a limiting Ly  $\alpha$  flux of  $2 \times 10^{-16}$  erg s<sup>-1</sup> cm<sup>-2</sup>, corresponding to an [O II] flux of  $\sim 8 \times 10^{-18}$  erg s<sup>-1</sup> cm<sup>-2</sup>. The expected space density is  $\sim 50$  per deg<sup>2</sup> but we will need to target  $\sim 100$  per deg<sup>2</sup> for this success rate. We will have a final sample of 800 objects, and this will take six hours.

4. In addition to these primary goals, we also have a few galaxy populations that may be targeted as filler to improve survey efficiency. Since each fiber has limited reach, we may be unable to find a suitable target for a given fiber at a given time. Auxiliary high redshift targets that we are considering include Ly  $\alpha$  blobs (we expect  $\sim 150$  in 16 deg<sup>2</sup> over the entire redshift range), LAEs at  $3 < z < 5$ , and fainter LBGs at  $2 < z < 5$ . In the latter cases there are many thousands of targets per deg<sup>2</sup>, but we will prioritize those in the vicinity of either quasar candidates or Ly  $\alpha$  blobs.

#### 4.3.5. Target Selection: Quasars down the luminosity function

Like the LBG samples described above, we will pursue a two-tiered quasar selection. However, since the quasar population is so rare, we will perform a shallow survey over 1400 deg<sup>2</sup> and then a deeper survey over the 16 deg<sup>2</sup> HSC Deep area. Our target strategy is summarized in Table 8.

The PFS-AGN wide survey is based on the wide layer of the HSC multi-band imaging legacy survey (5-band optical images of  $g, r, i, z$ , and  $y$ , combined with available wide NIR surveys by VISTA and UKIRT over 1400 deg<sup>2</sup>). We focus on the color-selected quasar candidates at  $3 < z < 7$  using color cuts similar to those used by the SDSS (Richards et al. 2002). We will target a few tens of quasar candidates per PFS pointing to a magnitude limit of  $i \leq 24$ , to achieve the number-density of quasars shown in Table 8. The primary goals include identifying  $6 < z < 7$  candidates for deeper spectroscopy to study reionization, measuring the quasar luminosity and mass function over  $3.5 < z < 7$ , and measuring the quasar auto- and cross-correlation functions and their dependence on redshift, mass, and luminosity. The total number of targets is small, and it will be integrated into the wide-field cosmology survey. As shown in §4, we can achieve these goals in 0.5 hr exposure times even at our magnitude limit.

The PFS-AGN deep survey is based on the deep layer of the HSC legacy survey. In addition to color selection, we will also target variable objects and X-ray and mid-infrared selected objects. We will go a magnitude deeper than the PFS-AGN wide survey, and expect to target 100 active galaxies per deg<sup>2</sup>. The goals include finding  $\sim 10$  faint  $z \approx 7$  quasars, studying X-ray and variability selected active galaxies at  $1 < z < 4$ , cross-correlating absorption systems in

the quasar spectra with the foreground galaxy population, and studying obscured populations in the galaxy survey that are identified via narrow emission lines. If we spend an hour per target for the majority of these targets, then it will take very few fibers from the main galaxy evolution survey.

#### 4.3.6. Summary of the Survey

In Table 8 we show all the sub-samples that we plan to target, their expected number density per square degree, the required exposure times, and the proposed survey area. Throughout, when we quote the required number of nights, we are assuming 1700 science fibers per PFS pointing and zero overhead in changing targets. We quote the number of required clear nights (that is, no weather factor has been applied). We outline a two-tiered survey, with our primary galaxy survey covering  $16 \text{ deg}^2$  and a deeper component covering  $3.5 \text{ deg}^2$ . To summarize, we will study the following galaxy populations:

- We will perform a continuum-selected survey of  $1 < z < 2$  galaxies with  $J_{\text{AB}} < 23.4 \text{ mag}$  over  $16 \text{ deg}^2$  and  $0 < z < 1$  galaxies with  $J_{\text{AB}} < 21 \text{ mag}$ . We will target  $\sim 28,000$  galaxies per  $\text{deg}^2$ . The primary survey will be color-selected, using a combination of HSC and IRAC imaging. We will also perform a purely magnitude-limited survey over two PFS pointings early in the survey to calibrate our selection strategy.
- At  $2 < z < 7$ , we trace the galaxy population using bright dropouts down to a limiting magnitude of  $i > 24 \text{ mag}$  over the full  $16 \text{ deg}^2$ . We expect to target 430 galaxies per  $\text{deg}^2$ . We will survey fainter LBGs to  $i > 24.5 \text{ mag}$  over  $3.5 \text{ deg}^2$  to study intervening absorption systems.
- We focus on LAEs at  $z = 5.5, 6.6, 7.3$ , in order to use the Ly  $\alpha$  emission as a probe of reionization. Additionally we will study LAEs at  $z \sim 2.3$ , where we can use the [O II] emission line to measure the systemic redshift.

Adopting these survey areas and target densities, the survey requires 105 clear nights. The survey parameters are summarized in Table 9.

#### 4.4. Requirements

We are assuming the nominal sensitivities and resolution of PFS. The feasibility of our survey relies most heavily on the sensitivity of PFS in the red and NIR arms, from which we will derive redshifts and key diagnostic information. Our most important assumptions are:

1. We assume 1700 fibers per PFS pointing. We also assume that it is possible to reposition fibers rapidly, so that we move off of bright targets in a short time. This large multiplexing capability is crucial for our science case, otherwise we cannot achieve the large areas and high sampling rates that make our survey unique.
2. We assume that we can measure continuum-based redshifts at our magnitude limit of  $J_{\text{AB}} = 23.4 \text{ mag}$ . Based on our spectral simulations, we find that in a 3 hr integration we will have at least the required S/N of 10 per pixel in the NIR arm to measure continuum-based redshifts (Tonry & Davis 1979), assuming  $R \sim 300$ .

We suggest real-time spectral analysis to identify low redshift interlopers after the initial 20 min integration.

3. We expect to reach a  $5\sigma$  emission-line limit of  $8 \times 10^{-18} \text{ erg s}^{-1} \text{ cm}^{-1}$  for  $> 50\%$  of the band. This limit is reached in the NIR arm in 3 hrs of integration on the [O II] line. We are assuming intrinsic line widths in the galaxies of  $\sigma_{\text{gas}} \approx 100 \text{ kms}^{-1}$ . The S/N will degrade by  $\sim 30\%$  for a galaxy with twice the dispersion, as the light is spread over roughly twice as many pixels. This gets us to  $L_{[\text{OII}]} \sim 8 \times 10^{41} \text{ erg s}^{-1}$  at  $z \approx 2$ , which is below the [O II] luminosity of a typical  $L^*$  galaxy at this epoch (e.g., Takahashi et al. 2007).
4. We find that we can detect Ly  $\alpha$  with  $7 \times 10^{-18} \text{ erg s}^{-1} \text{ cm}^{-2}$  in the blue arm with  $R \approx 1300$  at the  $5\sigma$  level in 6 hrs of integration. Again we assume an intrinsic gas dispersion of  $100 \text{ kms}^{-1}$ , which is typical of measured LAEs (Ouchi et al. 2010). We are thus detecting sources with  $L > 1.5 \times 10^{42} \text{ erg s}^{-1}$ , which is a factor of five fainter than the typical LAE at these redshifts (Ciardullo et al. 2012). In the red arm, our limits are slightly better. In 6 hrs our  $5\sigma$  detection limit is  $5 \times 10^{-18} \text{ erg s}^{-1} \text{ cm}^{-2}$  for  $> 50\%$  of the band. Here our limits of  $8.5 \times 10^{42} \text{ erg s}^{-1}$  at  $z = 5$  and  $2 \times 10^{43} \text{ erg s}^{-1}$  at  $z = 6$  are around or slightly exceed  $L_{\text{Ly}\alpha}^*$  at these epochs (Ouchi et al. 2010). Our limits are comparable to those achieved by Ouchi et al. (2010) for an individual object, and we will increase the sample size by two orders of magnitude.
5. In order to achieve the above continuum and emission-line limits above, we place strong requirements on our software, specifically in regard to sky subtraction in the red and NIR arms. We currently assume that we are able to determine the sky level at a given time to 0.5%. This is easily supported by the Poisson noise in the lines themselves. We further assume that we achieve a wavelength solution that is good to 0.01 pixel. Finally, we assume that no more than 1% of the light hitting the detector is distributed across the entire chip as a smooth background. We therefore assume that we understand systematics in sky subtraction at this level, and that there are no other systematic errors.

## 5. SCIENCE REQUIREMENTS

We now summarize the science requirements arising from the earlier sections. These requirements are necessary for deriving lower level instrument requirements and in understanding the flow of requirements from the science to detailed engineering. Establishing the science requirements flow is likewise essential in order to track the science impact of potential changes to the instrument configuration in the future. The top level science requirements and observing requirements are intended to be directly verifiable items in the project. For convenience, we list the overall drivers, item by item, both in tabular form and in more detail below.

The top-level science requirements for the PFS surveys described in the previous chapters are summarized in Table 10<sup>22</sup>. We briefly discuss the individual entries in Table 10.

<sup>22</sup> Our instrumental requirements for the different scientific goals outlined in this document are somewhat different. In particular, the galaxy science, which requires the deepest exposures, have the strongest requirements on

TABLE 9  
SURVEY PARAMETERS

$1 < z < 2$	
Selection (optical)	HSC Deep: $i < 27.2$ mag
Selection (NIR)	<i>XMM</i> -LSS, ELAIS-N1, and COSMOS: $J_{AB} < 23.4$ mag
Exposure time at flux limit	3 hrs
Area	16 deg <sup>2</sup>
Number of nights	68 nights
Flux-limited survey	
Selection (NIR)	<i>XMM</i> -LSS, ELAIS-N1, and COSMOS: $J_{AB} < 23.4$ mag
Exposure time at flux limit	3 hrs
Area	2 PFS pointings
Number of nights	10
High-redshift galaxies	
Selection (optical)	HSC Deep: $i < 27.2$ mag
Selection (narrow-band)	HSC Deep: $NB < 25$ mag
Exposure time at flux limit	3 hrs
Area	16 deg <sup>2</sup>
Number of nights	27
Total number of nights	105

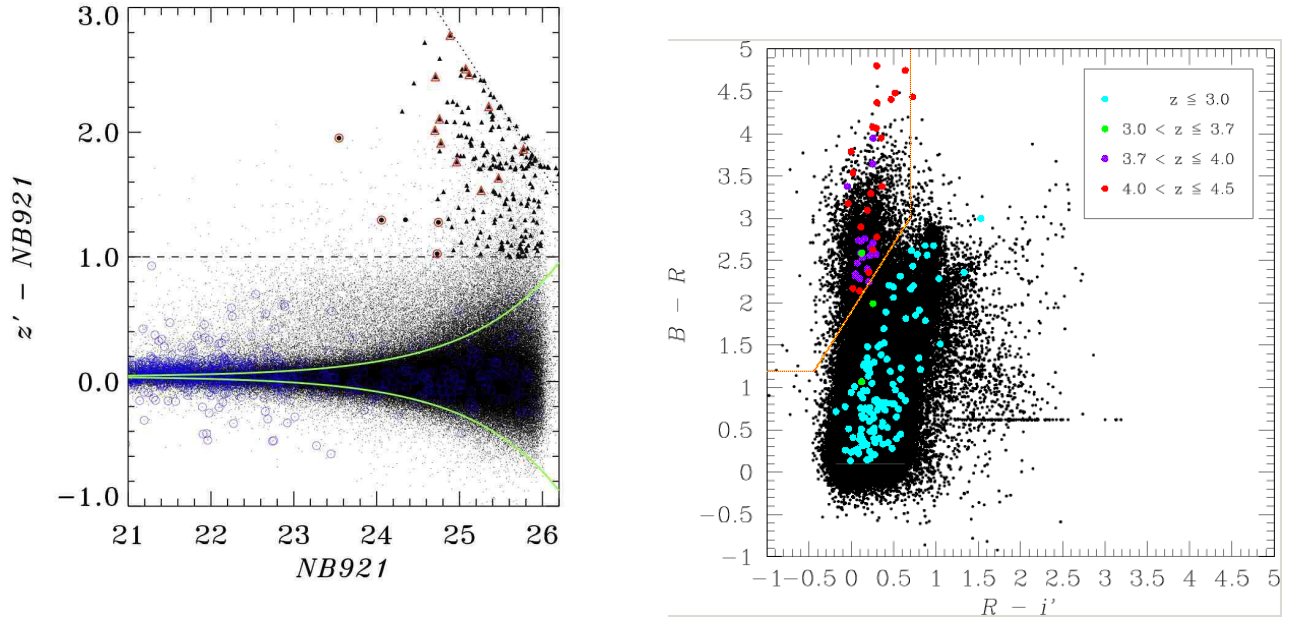


FIG. 26.— *Left*: Color magnitude diagram of narrow-band excess color ( $z' - NB921$ ) vs. narrow-band magnitude ( $NB921$ ) for selecting  $z = 6.6$  LAEs in the SXDS field (Ouchi et al. 2010), which will be applied to the LAE selection of our PFS survey. Black dots present colors of all the detected objects, while black filled circles and triangles denote the  $z = 6.6$  LAEs. Red and blue open symbols mark spectroscopically-identified objects in the redshift range of LAEs ( $z = 6.45 - 6.65$ ) and interlopers, respectively. The green lines indicate  $2\sigma$  errors of the color of  $z' - NB921$ . Dashed and dotted lines represent the color cut for the narrow-band excess and the  $1\sigma$  limit of  $z'$  data, respectively. *Right*: Two color diagram of objects down to  $i' \leq 26.85$  to select  $z \sim 4$  LBGs in the Subaru Deep Field (Yoshida et al. 2006). The horizontal sequence along  $B - R = 0.62$  shows objects which are fainter than the  $1\sigma$  magnitude in both  $B$  and  $R$ . The colored symbols show objects with spectroscopic redshifts, where cyan, green, violet, and red represent objects in the range  $z < 3.0$ ,  $3.0 \leq z < 3.7$ ,  $3.7 \leq z < 4.0$ , and  $4.0 \leq z < 4.5$ , respectively. The thick orange line indicates the boundary which are adopted for the selection of  $z \sim 4$  LBGs. Our PFS survey will use a broad-band set of  $g'r'i'$  different from this  $BRi'$  bands for selecting  $z \sim 4$  LBGs. However, the contamination rates of our  $z \sim 4$  LBG sample will be comparable, as demonstrated by another  $z \sim 4$  LBG selection with  $GRI$  bands (Steidel et al. 1999).

- **Wavelength Coverage:** The triple-armed spectrograph design offers complete and simultaneous spectral coverage from 380 through 1300 nm and clearly this represents a unique feature of PFS. The driver for this requirement arises from all 3 surveys discussed in Chap-

ters 2–4 but particularly the cosmology and galaxy surveys. The cosmology survey will enable the first BAO and RSD tests beyond  $z \simeq 2$  and the galaxy survey will track emission line properties of an unprecedented sample of galaxies with no ‘gaps’ in redshift coverage.

systematics such as stray light and sky subtraction. The overall requirements listed in Table 10 represent a compromise of sorts between the needs of the different scientific goals. As the instrument design becomes more solid, we will see to what extent the more stringent requirements of the galaxy evolution science are possible.

- **Spectral Resolution:** The resolutions of the three arms of each spectrograph are designed to ensure optimal efficiency in the study of stars and galaxies over the wide wavelength range. The resolution must be higher in the

TABLE 10  
Top-Level Science Requirements

Requirement	Value	Main Driver(s)
Wavelength Coverage	380 – 1300nm	All surveys
Spectral Resolution	Blue: $R \sim 2500$ Red: $R \sim 3000$ NIR: $R \sim 4000$	Matched survey efficiency sky subtraction, stellar metallicities radial velocity precision
Fiber Density	$\geq 2400$ per 1.3 deg. diameter hexagonally-shaped field	$\bar{n}_g P_g \simeq$ a few @ $k = 0.1 h/\text{Mpc}$ requirement in BAO survey
Throughput <sup>a</sup>	Average: $\geq 22\%$ (blue) $\geq 22\%$ (red) $\geq 24\%$ (NIR) Worst part of band: $\geq 20\%$ (blue) $\geq 20\%$ (red) $\geq 18\%$ (NIR)	Matched survey efficiency
Fiber Reconfig. Time	$\lesssim 3\text{min}$ in total	15min exposure in BAO survey
Sky Subtraction Accuracy	$\lesssim 1\%$ of sky background per 4-pixel resolution element	in all surveys
Stray Light	$\lesssim$ a few % of total sky brightness spread over detector	in all surveys
Read Out	$\leq 3$ (Red) $e^-$ rms per pixel $\leq 4$ (NIR) $e^-$	in all surveys
Wavelength Calibration	$\lesssim 0.1\text{\AA}$ ( $\sim 1/20\text{th}$ of a resolution element)	for velocity precision
Fiber Diameter	1.13'' deg. diameter at the field center 1.03'' at the edge	Optimal $S/N$ for galaxy survey
Pre-Imaging Data	<i>gri</i> to 25mag over 1400 deg <sup>2</sup> <i>griz+NB515</i> survey to $V \simeq 22.5\text{mag}$ <i>grizy+NBS+J</i> to $\sim 27\text{mag}$ over 16 deg <sup>2</sup>	Color selection of ELGs for BAO survey Selection of stars in Milky Way/M31 Color selection for galaxy survey
Survey Area	$\sim 1400$ deg <sup>2</sup> for BAO $\sim 500$ deg <sup>2</sup> for GA survey $\sim 16$ deg <sup>2</sup> for galaxy survey	Statistical requirements, cosmic variance, matching HSC data

<sup>a</sup> Excludes atmosphere, central obscuration + WFC vignetting, and fiber aperture effect.

red and near-infrared arm to ensure optimal sky subtraction in the dense OH forest. The minimum effective resolution in the red arm is set by our requirement to measure accurate velocities and stellar metallicities for the Galactic surveys.

- **Fiber Density:** The fiber density is set by the field of view of the provided Subaru prime focus corrector and our requirement that we optimally sample the  $0.8 < z < 2.4$  galaxy population for the cosmology survey at the wavenumber  $k$  where the BAO signal is to be recovered. Formally, this sets a requirement that the mean number density of target galaxies  $\bar{n}_g$  and the galaxy power spectrum  $P_g(k)$  should satisfy  $\bar{n}_g P_g \simeq 1$  (or a few) at  $k \simeq 0.1 h^{-1} \text{Mpc}$ .
- **Throughput:** The throughput requirement is driven by a combination of the  $S/N$  required for the various surveys and the available observing time, and is consistent with a preliminary assessment of the instrument performance. The values in the table exclude atmosphere, central obscuration, vignetting, and the fiber aperture effect.
- **Fiber Reconfiguration Time:** The reconfiguration time is set by the cosmology survey which is likely to have

the minimum exposure time given it must survey a large volume by targeting strong line emitting galaxies. If the exposure time is  $\simeq 15$  minutes, a reconfiguration time (including slewing, acquisition, guiding, fiber positioning and verification) should be completed in under 3 minutes to minimize survey inefficiency.

- **Sky Subtraction Accuracy:** This is set by the requirement for high quality spectra at faint limits in all surveys. It is particularly driven by the need for accurate absorption line measures in the red and near-infrared spectral regions where the OH forest is dense.
- **Stray Light:** As for sky subtraction, given the intensity of the OH night sky emission.
- **Detector Read Out:** This is set by the signal/noise requirements of each survey, noting their likely photon and sky-noise components.
- **Wavelength Calibration:** This is determined by the radial velocity accuracy for the Galactic surveys.
- **Fiber Diameter:** This is determined by the optimal signal/noise requirements of the galaxy and cosmology survey, noting the distribution of line emission in these extended sources.

- *Pre-Imaging Data:* This is determined by each individual survey and the various color-criteria to be adopted in optimally selecting either galaxies in a particular redshift range with certain star formation characteristics or stars of a given luminosity class in the Milky Way or M31. The aim is to ensure that all the relevant data not currently in hand is taken by HSC.
- *Survey Area:* This varies from one survey to another but is driven by statistical and/or cosmic variance requirements and the availability of HSC imaging data.

## 6. OUTSTANDING ISSUES

Our primary goal has been to present the science case for PFS in the context of an anticipated 300-night Subaru Strategic Program (SSP) and, thereby, to define the scientific requirements for the instrument as summarized in the previous section. The successful review of this science case and its associated technical document has led to an agreement to begin PFS construction with an anticipated first light in early 2017.

Science planning will naturally continue through to the Preliminary Design Review (anticipated in early 2013) and here we briefly describe those activities in the context of instrumental choices, the design of the survey and the broader impact of PFS beyond the initial SSP.

It should be understood that PFS planning involves two rather different communities: the international partnership focused scientifically via the PFS Survey Committee, and the Japanese astronomical community, whose interests are coordinated by the National Astronomical Observatory of Japan and its appointed national committees.

In the following we briefly introduce some of the items which will form the basis of the project discussions prior to the PDR.

### 6.1. Requirements Flowdown

As discussed in Section 5, for a project with the size and complexity of PFS, formal science and instrument requirements are necessary to guide the design and construction of the system, and allow the rapid assessment of design or performance changes during the course of the project. They will also guide the instrument test plan to be developed at a later stage in the project; each requirement will include the method for validating that it has been met. The full documentation of formal and tracked requirements will be completed by the PDR, and will define the required performance of the instrument system and the subsystems in order to achieve the science goals.

The requirements can be broken into several levels, and we will use the following definitions. The Level 1 (L1) requirements are the top level science requirements that comprise the reason for building the instrument. The Level 2 (L2) requirements are ones that are imposed on the entire instrument or multiple subsystems. Requirements on a single subsystem are Level 3 (L3) requirements. Level 4 (L4) requirements are the requirements created by the subsystem designers in order to implement the Level 3 requirements.

Although the top level science requirements, L2, are summarized in Section 5, they will be refined and formalized by PDR (the L1 requirements are described in detail in Sections 2 – 4 for each science case). These focus on the science driven requirements and may not yet be complete. Specifically, they do not yet include all of the instrument level operational and interface requirements. The L3 and L4 requirements are in the

process of being developed. Although there has been extensive discussion of these requirements, they are not yet ready for this documentation.

The PFS project office will lead the effort to refine, formalize, and document the L1-L4 requirements, in coordination with the science and instrument working groups. This process will be complete for the L1-L3 requirements before PDR, while the definition of L4 requirements may evolve after the PDR. The documentation will consist of a formal list of individual requirements with a description, rationale, and validation method listed for each requirement. The rationale will consist of a short paragraph explaining why the requirement is needed, any assumptions that were made, and what design effort drove the requirement. It puts the requirement in context, and helps reduce ambiguities and misunderstandings. All of the instrument requirements are intended to be verified during the acceptance testing of the instrument, under a written test plan.

### 6.2. Technical Design

The outstanding item here is related to an intermediate dispersion requirement which would significantly enhance the ability of PFS to measure chemical abundances for a wider range of elements. The Galactic Archeology working group has made a strong case for an additional spectroscopic mode with spectral resolution  $R=5000$  (and possibly higher) but with a limited wavelength coverage. This would enable PFS to unravel the temporal chemical evolution of each building block of Galactic halo and thick disk through their multi-element alpha abundances revealed in this wavelength range, namely  $[X/Fe]$  with  $X=Mg, Si, Ca, Ti$  in comparison with  $[Fe/H]$ .

The PFS team has acknowledged the strong scientific case for this component which is also well-suited to the Subaru 8.2 meter aperture giving PFS a distinct advantage over massively-multiplexed spectrographs on 4 meter telescopes. Incorporating this requirement into the design was not possible by the CoDR and we intend to evaluate and cost two possible technical solutions prior to PDR as well as to determine their operational feasibility.

- Reconfigure the current red arm spectrograph so that it is possible to switch from the default mode to one suitable for intermediate dispersion studies. Such an ‘intermediate dispersion mode’ might be undertaken during a dedicated period of Galactic science or at the end of the cosmology/galaxy surveys.
- Develop an independent spectrograph whose resolution is not restricted to lie within the boundaries of the current 3-arm design. Although a more expensive option this may better suit a dedicated Galactic campaign given the earlier WFMOS studies made a strong case for a much higher resolution instrument.

### 6.3. Planning the Subaru Strategic Program

The three Working Groups have, thus far, largely worked independently in defining their science requirements and there has been little discussion of how to integrate the 3 surveys into a single coherent observing program. Ultimately the PFS partnership will have to take Sections 2 – 4 forward and write one or more Subaru Strategic Programs for consideration by the NAOJ Subaru Time Allocation Committee.

Issues that the PFS team will address in discussions with NAOJ and the HSC team will include:



- Selecting fields within the HSC imaging survey
- Science prioritization of the various survey components
- Target sharing and exposure time optimization
- Bright and dark time balance on the telescope

The bright and dark time balance will depend critically on the question of how the Subaru Observatory intends to operate PFS alongside HSC and the bright time use of PFS will, in turn, depend on whether there is a feasible intermediate dispersion capability.

#### 6.4. Legacy Value

The Subaru archive is formally a responsibility of NAOJ but the quality and delivery of the survey products is that of the current PFS science team. No negotiations have yet taken place on this important issue, but we expect a full agreement on responsibilities, proprietary periods, international access etc by the time of the PDR.

#### 6.5. Synergy with Other Facilities

PFS will have a significant impact beyond the surveys discussed in this document in two ways.

Firstly, the survey fields will deliver spectroscopic data of value to extant imaging facilities. During the pre-LSST era we can expect inquiries from those international teams for access to PFS data. Such access could be dealt with largely under the auspices of the Subaru archive discussed above, but there may be cases where new collaborations are valuable, either to the PFS team, the Japanese community or both. Such opportunities will need to be considered and the roles and rights of the PFS team, NAOJ etc fully understood.

A potentially more interesting opportunity is the likelihood of new collaborations with both current imaging survey telescopes and future facilities such as LSST, Euclid and perhaps ultimately TMT, beyond the scope of the Subaru Strategic

Program (SSP) introduced here. Formally, beyond the SSP, PFS will become the property of NAOJ but the current partnership may have the opportunity to participate and contribute in future surveys conducted in conjunction with other facilities.

## 7. SUMMARY

Our intention via this document is to describe in as much detail as practical, the exciting scientific programs we have designed for the Subaru Prime Focus Spectrograph, as well as to present our first iteration for a Subaru Strategic Program (SSP) of  $\approx 300$  nights that would realize these goals. The flow-down from these science requirements has been summarized in the context of the top-level instrument requirements which provide important constraints on the technical design of each component of PFS.

PFS will likely be the first massively-multiplexed spectrograph on a large aperture telescope to achieve first light. Its unique capabilities on an 8 meter platform at an excellent site promises exciting discoveries in 3 broad areas: the nature of dark energy through an ambitious survey of emission lines galaxies over an unprecedented redshift range  $0.8 < z < 2.4$ , the assembly history of the Milky Way and M31 through strategically-designed programs that exploit astrometric data from the Gaia mission, and galaxy evolution over a wide range in redshift ( $1 < z < 7$ ) exploiting PFS' unique wide wavelength coverage.

Although our initial goal is to construct the instrument and conduct a refined version of the SSP presented in this article, we are strongly motivated to consider the longer term role of this survey instrument in the era of LSST, Euclid and TMT.

This work is supported in part by the JSPS Core-to-Core Program "International Research Network for Dark Energy", by World Premier International Research Center Initiative (WPI Initiative), MEXT, Japan, and by the FIRST program "Subaru Measurements of Images and Redshifts (SuMIRE)", CSTP, Japan.

## REFERENCES

- Adelberger, K. L., Steidel, C. C. 2005, *ApJ*, 630, 50  
 Albrecht, A., et al., The Dark Energy Task Force Report, astro-ph/0609591  
 Alcock, C., Paczynski, B. 1979 *Nature* 281, 358  
 Allende Prieto, C., Beers, T. C., Wilhelm, R., Newberg, H. J., Rockosi, C. M., Yanny, B., & Lee, Y. S. 2006, *ApJ*, 636, 804  
 Allende Prieto, C. et al. 2008, *AJ*, 136, 2070  
 Anderson, L. et al., 2012, arXiv:1203.6594  
 Ando, M., Ohta, K., Iwata, I., Akiyama, M., Aoki, K., Tamura, N. 2007, *PASJ*, 59, 717  
 Beers, T. C., Rossi, S., Norris, J. E., Ryan, S. G., & Sheer, T. 1999, *AJ*, 117, 981  
 Belokurov, V. et al. 2006, *ApJ*, 642, L137  
 Belokurov, V. et al. 2008, *ApJ*, 686, L83  
 Blake, C., et al. (WiggleZ team) 2011, *MNRAS*, 415, 2892  
 Bordoloi, R., et al. 2011, *ApJ*, 743, 10  
 Brammer, G. B., van Dokkum, P. G., Coppi, P. 2008, *ApJ*, 686, 1503  
 Carlberg, R. 2011, arXiv:1109.6022  
 Carlin, J. L. et al. 2012, arXiv:1205.2371  
 Chen, Y.-M., et al. 2012, *MNRAS*, 421, 314  
 Ciardullo, R., et al. 2012, *ApJ*, 744, 110  
 Coil, A., et al. 2008, *ApJ*, 672, 153  
 Contaldi, C. R., Peloso, M., Kofman, L., Linde, A. 2003, *JCAP* 07, 002  
 Cooper, M. C., et al. 2006, *MNRAS*, 370, 198  
 Dalal, N., Dore, O., Huterer, D., Shirokov, A. 2008, *Phys. Rev. D* 77, 123514  
 Davis, M., Faber, S. M., Newman, J., et al. 2003, *SPIE*, 4834, 161  
 Efstathiou, G. 2003, *MNRAS* 343, L95  
 Eisenstein, D., et al. 2005, *ApJ* 633, 560  
 Eisenstein, D., Seo, H.-J., Sirko, E., Spergel, D. N. 2007, *ApJ*, 664, 675  
 Fellhauer, M. et al. 2006, *ApJ*, 651, 167  
 Freeman, K., & Bland-Hawthorn, J. 2002, *ARAA*, 40, 487  
 Garbari, S., Read, J. I., & Lake, G. 2011, *MNRAS*, 416, 2318  
 Gilbert, et al. 2012, preprint  
 Guth, A. H., Nomura, Y. 2012, arXiv:1203.6876  
 Guzzo, L., et al. 2008, *Nature*, 451, 541  
 Hayashi, H., & Chiba, M. 2006, *PASJ*, 58, 835  
 Helmi, A., & de Zeeuw, P. T. 2000, *MNRAS*, 319, 657  
 HerMES Collaboration, Oliver, S. J., Bock, J., et al. 2012, arXiv:1203.2562  
 Hikage, C., Takada, M., Spergel, D. N. 2012, *MNRAS* 419, 3457  
 Ho, L. C., Filippenko, A. V., & Sargent, W. L. W. 1997, *ApJS*, 112, 315  
 Holmberg, J., & Flynn, C. 2000, *MNRAS*, 313, 209  
 Hopkins, A. M., Beacom, J. F. 2006, *ApJ*, 651, 142  
 Hu, W., Haiman, Z. 2003, *Phys. Rev. D* 68, 063004  
 Ibata, R. A., Gilmore, G., & Irwin, M. J. 1994, *Nature*, 370, 194  
 Ilbert, O., et al. 2010, *ApJ*, 709, 644  
 Ishigaki, N. M., Chiba, M. & Aoki, W. 2012, *ApJ*, in press  
 Jouvel, S., et al. 2011, *A&A* 504, 359  
 Kaiser, N., *MNRAS* 227, 1 1987  
 Kirby, E. N., Guhathakurta, P., & Sneden, C. 2008, *ApJ*, 682, 1217  
 Kirby, E. N. et al. 2009, *ApJ*, 705, 328  
 Kirby, E. N. et al. 2010, *ApJS*, 191, 352  
 Kleban, M., Schillo, M., arXiv:1202.5037  
 Komatsu, E., *WMAP Team* 2011, *ApJ Suppl.*, 192, 18  
 Kogosov, S. E. et al. 2011, arXiv:1111.7042  
 Kordopatis, G., et al. 2011, *A&A*, 535, A106+  
 Kormendy, J., Richstone, D. 1995, *ARA&A*, 33, 581  
 Kriek, M., van Dokkum, P. G., Whitaker, K. E., Labbé, I., Franx, M., Brammer, G. B. 2011, *ApJ*, 743, 168  
 Kriek, M., et al. 2006, *ApJ*, 649, L71  
 Le Fèvre, O., et al. 2005, *A&A*, 439, 845  
 Lee, Y. S. et al. 2008, *AJ*, 136, 2008  
 Lee, Y. S. et al. 2010, arXiv:1010.2934 (2011, *AJ*, 141, 90)  
 Lee, Y. S. et al. 2011, *ApJ*, 738, 187

- Li, H. N. et al. 2010, *A&A*, 521, A10+  
 Lilly, S. J., et al. 2007, *ApJS*, 172, 70  
 —. 2009, *ApJS*, 184, 218  
 Linder, E. 2003, *Rhys. Rev. Lett.*, 90, 091301  
 Linder, E. 2005, *Rhys. Rev. D* 72, 043529  
 Magorrian, J., et al. 1998, *aj*, 115, 2285  
 Maraston, C. 2005, *MNRAS*, 362, 799  
 Marconi, A., Hunt, L. K. 2003, *ApJ*, 589, L21  
 Matsubara, T. 2008, *Phys. Rev. D* 77, 063530; *Phys. Rev. D* 78, 083519  
 McQuinn, M., Hernquist, L., Zalzarriaga, M., & Dutta, S. 2007, *MNRAS*, 381, 75  
 Morrison, H. L. et al. 2003, *AJ*, 125, 2502  
 Moster, B. P., et al. 2010, *ApJ*, 710, 903  
 Nishimichi, T., Taruya, A. 2011, *Phys. Rev. D* 84, 043526  
 Nishizawa, A., Takada, M., Nishimichi, T., in preparation.  
 Norris, J. E. et al. 2008, *ApJ*, 689, L113  
 Orsi, A., Baugh, C., Lacey, C., Cimatti, A., Wang, Y., Zamorani, G. 2010, *MNRAS*, 405, 1006  
 Ostriker, J. P. & Steinhardt, P. 2003, *Science*, 300, 1909  
 Ouchi, M., et al. 2008, *ApJS*, 176, 301  
 —. 2010, *ApJ*, 723, 869  
 Padmanabhan, N., Xu, X., Eisenstein, D., Scalzo, R., Cuesta, A. J., Metha, K., Kazin, E., arXiv:1202:0090  
 Panter, B., Jimenez, R., Heavens, A. F., Charlot, S. 2007, *MNRAS*, 378, 1550  
 Papovich, C. 2008, *ApJ*, 676, 206  
 Peacock, J. A., et al. (the 2dF team) 2001, *Nature*, 410, 169  
 Penarrubia, J. et al. 2010, *MNRAS*, 408, L26  
 Percival, W., et al. 2007, *MNRAS*, 381, 1053  
 Re Fiorentin, P., Bailer-Jones, C. A. L., Lee, Y. S., Beers, T. C., Sivarani, T., Wilhelm, R., Allende Prieto, C., & Norris, J. E. 2007, *A&A*, 467, 1373  
 Reddy, N., et al. 2012, *ApJ*, 744, 154  
 Richards, G. T., et al. 2002, *AJ*, 123, 2945  
 Richardson, J. C., et al. 2011, *ApJ*, 732, 76  
 Robin, A. C., Reylé, C., Derrière, S., & Picaud, S. 2003, *A&A*, 409, 523  
 Saito, S., Takada, M., Taruya, A. 2008, *Phys. Rev. Lett.*, 100, 191301  
 Saito, S., Takada, M., Taruya, A. 2008, *Phys. Rev. D* 80, 083528; 2011, *Phys. Rev. D* 83, 043529  
 Sehgal, N., et al. 2010, *ApJ*, 709, 920  
 Seo, H.-J., Eisenstein, D. 2003, *ApJ*, 598, 720  
 Seo, H.-J., Eisenstein, D. 2007, *ApJ*, 665, 14  
 Shapley, A. E., Steidel, C. C., Pettini, M., Adelberger, K. L. 2003, *ApJ*, 588, 65  
 Simon, J. D. et al. 2010, arXiv:1007.4198  
 Smith, M. C., Whiteoak, S. H., & Evans, N. W. 2012, *ApJ*, 746, 181  
 Starkenburg, E. et al. 2010, *A&A*, 513, A34+  
 Shen, Y., Greene, J. E., Strauss, M. A., Richards, G. T., & Schneider, D. P. 2008, *ApJ*, 680, 169  
 Sobral, D., et al. 2010, *MNRAS*, 404, 1551  
 Stark, D. P., Ellis, R. S., & Ouchi, M. 2011, *ApJ*, 728, L2  
 Steidel, C. C., et al. 2010, *ApJ*, 717, 289  
 Freivogel, B., Kleban, M., Martinez, M. R., Susskind, L. 2006, *JHEP*, 03, 039  
 Takada, M., Komatsu, E., Futamase, T. 2006, *Phys. Rev. D* 73, 083520  
 Takahashi, M. I., et al. 2007, *ApJS*, 172, 456  
 Tanaka, M., Chiba, M., Komiyama, Y., Guhathakurta, P., Kalirai, J. S., & Iye, M. 2010, *ApJ*, 708, 1168  
 Tang, J., Kayo, I., Takada, M. 2011, *MNRAS*, 416, 2291  
 Taruya, A., Nishimichi, T., Saito, S., Hiramatsu, T. 2009, *Phys. Rev. D* 80, 123503  
 Taruya, A., Nishimichi, T., Saito, S. 2010, *Phys. Rev. D* 82, 063522  
 Tinker, J. L., Wetzell, A. R. 2010, *ApJ*, 719, 88  
 Tonry, J., & Davis, M. 1979, *AJ*, 84, 1511  
 Tolstoy, E., Hill, V., & Tosi, M. 2009, *ARAA*, 47, 371  
 Tremonti, C. A., Moustakas, J., Diamond-Stanic, A. M. 2007, *ApJ*, 663, L77  
 Tumlinson, J., et al. 2011, *Science*, 334, 948  
 Vanden Berk, D. E., et al. 2001, *AJ*, 122, 549  
 Whitaker, K. E., et al. 2011, *ApJ*, 735, 86  
 Williams, R. J., Quadri, R. F., Franx, M., van Dokkum, P., Labbé, I. 2009, *ApJ*, 691, 1879  
 Yan, R., Newman, J. A., Faber, S. M., et al. 2006, *ApJ*, 648, 281  
 Yoshida, M., et al. 2006, *ApJ*, 653, 988  
 Wilhelm, R., Beers, T. C., & Gray, R. O. 1999, *AJ*, 117, 2308  
 Zakamska, N. L., et al. 2003, *AJ*, 126, 2125

## APPENDIX

## PFS COLLABORATION

**Principal Investigator (PI)**

Hitoshi Murayama Kavli Institute of the Physics and  
 Mathematics for the Universe (Kavli IPMU, WPI), Japan;  
 Physics Department, University of California, Berkeley;  
 Lawrence Berkeley National Laboratory, Berkeley, USA

**Co-Chairs of the PFS Survey Committee**

Richard Ellis Caltech, USA  
 Masahiro Takada Kavli IPMU, Japan

**Co-Chairs of the PFS Science Working Groups****PFS Cosmology WG**

Masahiro Takada Kavli IPMU, Japan  
 Christopher Hirata Caltech, USA  
 Jean-Paul Kneib LAM, France

**PFS Galactic Archaeology WG**

Masashi Chiba Tohoku University, Japan  
 Judith Cohen Caltech, USA  
 Rosemary Wyse JHU, USA

**PFS Galaxy WG**

Jenny Greene Princeton University, USA  
 Kevin Bundy Kavli IPMU, Japan  
 John Silverman Kavli IPMU, Japan  
 Masami Ouchi The University of Tokyo, Japan

**PFS AGN/QSO WG**

Tohru Nagao Kyoto University, Japan  
 Michael Strauss Princeton University, USA

**PFS Steering Committee**

H. Aihara (U. Tokyo/Kavli IPMU), N. Arimoto (NAOJ), R. Ellis (Caltech), T. Heckman (JHU), P. Ho (ASIAA), O. Le Fevre (LAM), H. Murayama (Kavli IPMU), L. Sodre Jr. (Sao Paulo), M. Seiffert (JPL/Caltech), D. N. Spergel (Princeton), Y. Suto (U. Tokyo), H. Takami (NAOJ)

#### **Members in the PFS Science Working Groups**

L. R. Abramo (Sao Paulo), H. Aihara (U. Tokyo/Kavli IPMU), W. Aoki (NAOJ), N. Arimoto (NAOJ), C. Bennett (JHU), T.-T. Chang (AIAA), M.-Y. Chou (ASIAA), J. Coupon (ASIAA), R. Dekany (Caltech), C. M. de Oliveira (Sao Paulo), O. Dore (JPL/Caltech), T. Goto (Hawaii), J. Gunn (Princeton), K. Hayashi (Tohoku), S. Hayashi (NAOJ), T. Heckman (JHU), C. Hikage (Nagoya U.), B.-C. Hsieh (ASIAA), K. Ichikawa (Kyoto U.), K. Ichiki (Nagoya U.), M. Imanishi (NAOJ), M. Ishigaki (NAOJ), M. Iye (NAOJ), I. Iwata (NAOJ), O. LeFevre (LAM), L. Lin (ASIAA), Y. T. Lin (ASIAA), I. Kayo (Toho U.), H. Karoji (Kavli IPMU), N. Katayama (Kavli IPMU), D. Kawata (UCL), E. Kirby (Caltech), T. Kodama (NAOJ), Y. Komuro (Tohoku U.), K. Maeda (Kavli IPMU), R. Mandelbaum (Princeton), T. Marriage (JHU), T. Matsubara (Nagoya U.), K. Matsuoka (Ehime U.), B. Menard (JHU), S. Mineo (U. Tokyo), H. Miyatake (U. Tokyo), T. Morokuma (U. Tokyo), K. Motohara (U. Tokyo), L. Moustakas (JPL), Y. Matsuda (Caltech), S. S. Murray (JHU), F. Nakamura (NAOJ), T. Nishimichi (Kavli IPMU), A. Nishizawa (Kavli IPMU), M. Oguri (Kavli IPMU), S. Okamoto (Beijing), Y. Okura (NAOJ), Y. Ono (U. Tokyo), P. Price (Princeton), A. R. Pullen (JPL), R. Quimby (Kavli IPMU), A. Raccanelli (JPL), M. Sato (Nagoya U.), M. Seiffert (JPL), A. Shimono (Kavli IPMU), D. N. Spergel (Princeton), D. K. Stern (JPL), H. Sugai (Kavli IPMU), S. Saito (Berkeley), T. Saito (Kavli IPMU), T. Storchi-Bergmann (IF-UFRGS, Brazil), Y. Suto (U. Tokyo), N. Suzuki (LBL), A. Szalay (JHU), R. Takahashi (Hiroshima U.), N. Takato (NAOJ), M. Tanaka (Kavli IPMU), M. Tanaka (Tohoku) A. Taruya (U. Tokyo), N. Tominaga (Konan U.), Y. Urata (NCU), K. Yamamoto (Hiroshima U.), K. Wada (Kagoshima U.), W.-H. Wang (ASIAA), R. Wyse (JHU), T. Yamada (Tohoku U.), N. Yasuda (Kavli IPMU), N. Zakamska (JHU)

#### **PFS Project Office**

H. Karoji (Kavli IPMU), H.-H. Ling (ASIAA), Y. Ohya (ASIAA), H. Sugai (Kavli IPMU), A. Shimono (Kavli IPMU), N. Takato (NAOJ), N. Tamura (Kavli IPMU), A. Ueda (NAOJ)